2019

Multiphase Droplet Interactions with a Single Fiber

Noor M. Farhan
Virginia Commonwealth University

Multiphase Droplet Interactions with a Single Fiber

A dissertation submitted in partial fulfillment of the requirements for the degree of

Doctor of Philosophy at Virginia Commonwealth University.

By:

Noor M. Farhan

M.Sc. Mechanical Engineering, Baghdad University, Baghdad, Iraq, 2011

Director: Hooman V. Tafreshi

Professor, Department of Mechanical and Nuclear Engineering

Virginia Commonwealth University
Richmond, Virginia

May, 2019

Dedication

I would like to dedicate this work to my family. Their sincere prayers have always paved the roughness of all my scientific endeavors. My father, mother, brothers, sisters and all of my family, thank you for your contribution to this work through supporting me emotionally and materialistically. I would like to express my gratitude and dedicate this work to my husband and my kids (Hussain) and (Ibrahim) whose love made it possible for me to finish this thesis successfully.

Acknowledgment

First and foremost, I am grateful to God for the good health, well-being and blessings bestowed upon me throughout life and to accomplish this work.

I wish to express my sincere thanks to my advisor and my mentor Prof. Hooman V. Tafreshi. Professor of Mechanical and Nuclear Engineering Department, School of Engineering, Virginia Commonwealth University for his continuous support of my scientific endeavors; valuable guidance, and encouragement. His guidance, his patience, and his mentorship will always be appreciated. I want to express my gratitude to him because of him this work has been done.

I would also like to extend my feeling of gratitude to my committee members—Prof. Gary C. Tepper, Prof. Jayasimha Atulasimha, Prof. Ram B. Gupta, and Dr. Christopher A. Lemmon. Thank you all for finding time on your very busy schedule for me and the willingness to hear me and advise wisely. My labmates—Amrei, Hemeda, Ganesh, Hussain, Sina, Ali and Mohammad—are also supported me and I appreciate their help.

I will always be grateful to my family for their love, patience, guidance, and inspiration. Without every single one of you, it would not have happened that I wrote a dissertation today. You all make a bouquet of relationships that I hold in high esteem; cherish; and will maintain as I move forward.

I want to express my appreciation to the source of funding during my graduate education: The Higher Committee for Education Development in Iraq (HCED-Iraq).

Table of Contents

Abstract

Multiphase Droplet Interactions with a Single Fiber

By: Noor M. Farhan

A dissertation submitted in partial fulfillment of the requirements for the degree of Doctor of Philosophy at Virginia Commonwealth University.

Virginia Commonwealth University, 2019
Director: Hooman V. Tafreshi,
Professor, Department of Mechanical and Nuclear Engineering

Formulating the physics of droplet adhesion to a fiber is interesting intellectually and important industrially. A typical example of a droplet–fiber system in nature is the dew droplets on spider webs, where droplets first precipitate and grow on the fibers, but they eventually fall when they become too heavy. Obviously, quantifying the force of adhesion between a droplet and a fiber is crucial in designing fog harvesting devices or manufacturing filtration media for liquid–gas or liquid–liquid separation, among many other industrial applications. This study is aimed at developing a mathematical framework for the mechanical forces between a droplet and a fiber in terms of their physical and wetting properties. To this end, a series of experiments were conducted to detach ferrofluid droplets of varying volumes from fibers with different diameters and Young–Laplace contact angles (YLCAs) in a controlled magnetic field. The force of detachment was measured using a sensitive scale and used along with the results of numerical simulations to develop a semi-analytical expression for the force required to detach a droplet from a fiber. This universally-applicable expression allows one to predict the force detachment without the need to run an experiment or a computer simulation.

This work also reports on the use of magnetic force to measure the force of detachment for nonmagnetic droplets for the first time. This is accomplished by adding a small amount of a ferrofluid to the original nonmagnetic droplet to create a compound droplet with the ferrofluid nesting inside or cloaking the nonmagnetic droplet. The ferrofluid is then used to induce a body force to the resulting compound droplet and thereby detach it from the fiber. The recorded detachment force is used directly (the case of nesting ferrofluid) or after scaling (the case of cloaking ferrofluid) to obtain the force of detachment for the original nonmagnetic droplet. The accuracy of these measurements was examined through comparison with numerical simulations as well as available experimental data in the literature. In addition, a simple method is developed to directly measure the intrinsic contact angle of a fiber (i.e., Young–Laplace Contact angle of the fiber material) with any arbitrary liquid. It is shown that the intrinsic contact angle of a fiber can be obtained by simply measuring the angle between the tangent to the fiber surface and the tangent to the droplet at the contact line, if the droplet possesses a clamshell conformation and is viewed from the longitudinal direction. The novelty of the proposed method is that its predictions are not affected by the volume of the droplet used for the experiment, the wettability of the fiber, the surface tension of the liquid, or the magnitude of the body force acting on the droplet during the experiment.

Also, a liquid droplet interaction with granular coatings is simulated and the droplet apparent contact angle (ACA) and the transition from Cassie (fully dry) to Wenzel (fully wet) state as a function to the roughness wavelength have been studied. For a fixed droplet volume, two different granular coatings have been used, spherical and hemispherical bumps. It is demonstrated that the chemistry (YLCA) and geometrical parameters for the granular microtexture play an important effect on the droplet ACA and its transition from Cassie to Wenzel state.

Chapter 1. Introduction

1.1 Droplet Interactions with Fibers

Droplets on fibers are part of our everyday lives. Indeed, many phenomena involve drops on fibers such as the formation of dew droplets on a spider web, the trapping of water droplets on cactus spines or the dyeing of cotton or wool fibers. Therefore, this topic has received significant attention for years and is still an important topic. However, understanding the underlying physics of droplet detachment from the fiber is a challenging problem of crucial importance to many engineering applications such as liquid−liquid separation, liquid−gas filtration, textiles, microfluidics, water transport in fuel cells, and even water harvesting, to name a few [Contal *et al.* 2004; Michielsen and Lee 2007; Gauthier *et al.* 2012; Gilet *et al.* 2009; Ju *et al.* 2012; Patel and Chase 2014; Wurster *et al.* 2015]. A simple manifestation of the role of droplet−fiber interactions in nature is the dew formation on spider webs or cactus spines where droplets first adhering to such fibrous structures when they are small, but then detach from the fibers when they grow larger (e.g., see [Bai *et al.* 2010; Ju *et al.* 2012; Malik *et al.* 2016]). So, formulating the physics of droplet adhesion to a fiber is interesting intellectually and important industrially. Obviously, quantifying the force of adhesion between a droplet and a fiber is crucial in designing fog-harvesting media (e.g., [Xu *et al.* 2016]), filtration media for liquid–gas or liquid–liquid separation (e.g., [Contal *et al.* 2004]), functional textiles (e.g., [Michielsen and Lee 2007]), and open microfluidics system (e.g., [Gilet *et al.* 2009]) among many other applications.

Starting with the pioneering work of Carroll [Carroll 1976], droplet equilibrium shape on a single fiber has been vastly studied by various groups (e.g., [Carroll 1991; De Ruiter *et al.* 2012; Mei *et al.* 2013]). Depending on the fiber radius, droplet volume and the surface energy of the fiber, two fundamentally

different conformations of macroscopic droplets has been found (i.e., barrel and clam-shell conformations). Barrel shapes occur for large droplets relative to the fiber radius or for low contact angles. Clam-shell shapes occur for small droplets or high contact angles. Despite the prevalence of such technology in industry, only a few studies have been focused on quantifying droplet detachment force from a fiber. Correlations have been reported to relate droplet mobility to volume of the droplet, surface tension, Reynolds number and capillary number which are applicable only over a narrow set of parameters [Mullins *et al.* 2011; Funk *et al.* 2014; Hong *et al.* 2011]. Wettability of the fibers is important to many industries such as coating processes, textile fabrication, self-cleaning processes and filtration of fluids. Early studies on the wetting phenomena of droplet-on-fiber systems have reported on determining the droplet shape and on extracting the contact angle accurately which is different from the contact angle that the same liquid would form on a flat plate [McHale and Newton 2002; Rebouillat *et al.* 1999]. Our study easy-to-use mathematical expressions that can be used to predict the force needed to detach a given droplet from an arbitrary fiber using existing data obtained for a fiber–droplet system. In addition, we developed a semi-empirical correlation to calculate the force required to detach a droplet from a fiber in a direction normal to the fiber axis (referred to here as droplet detachment force), for fiber–droplet system with different dimensions or physical properties, for the first time.

We came up with a new method to measure fibers contact angle. During the past decades, several methods have been developed to determine the solid CA from the shape of drop. The analysis of the sessile drop profile is preferred in recent years due to a broad availability of image analysis systems and softwares that handle the profiling of the sessile drop shape. However, this method is not as straightforward for fibers since their cylindrical geometry affects the drop shape [Carroll 1976; McHale and Newton 2002]. Recently, method was proposed based on the analysis of the meniscus formed when a fiber is immersed into a liquid [Clanet and Quere 2002]. The meniscus can be fitted by the Young–Laplace equation;

alternatively, the contact angle can be calculated from the meniscus height. Unfortunately, small dimensions of the liquid meniscus climbing over the small-diameter fiber poses challenges in collecting enough data points for plotting the Young–Laplace equation.

In our study, an alternative method is proposed. Contact angles are determined on fibers directly through analysis of a clamshell droplet profile formed on fibers under the influence of gravity. The shape of the drop is directly imaged from the longitudinal view with the fiber, and the contact angle is determined as a geometrical parameter from the intersection of the drop profile with the solid. The measurement is achieved by simply aligning the tangent of the drop profile at the contact point with the solid surface tangent and reading the protractor through the eyepiece.

Detaching non-magnetic droplet has been studied experimentally [Mullins *et al.* 2007; Mead-Hunter *et al.* 2011; Sahu *et al.* 2013; Fang *et al.* 2015; Hotz *et al.* 2015; Davoudi *et al.* 2016], and each study has been conducted such a complicated method to detach the droplet. In most of these studies, droplet motion away from the fiber(s) were driven by air flow, surface wetting heterogeneity, or an external mechanical device like an atomic force microscope (AFM) cantilever. The experimental method developed in the work presented here, on the other hand, circumvents many complications that arise from the use of air or an external device to detach or move a droplet. For instance, when air is used as the driving mechanism to detach a droplet from a fiber, the resulting force can become somewhat dependent on the aerodynamic field around the droplet−fiber assembly (e.g., laminar vs turbulent, dependent on the flow orientation with respect to fibers) as well as the geometry of the test chamber used for the experiment [Sahu *et al.* 2013; Fang *et al.* 2015; Davoudi *et al.* 2016]. Likewise, bringing an AFM cantilever tip (even treated with a phobic coating) into contact with the droplet may change the original problem of a droplet interacting with a fiber to a new problem of a droplet interacting with a fiber and a cantilever tip (and its associated droplet

shape changes) [Mullins *et al.* 2007; Mead-Hunter *et al.* 2011; Hotz *et al.* 2015]. The use of an AFM microscope for such measurements also comes with additional limitations with regard to imaging the droplet during the experiment, the cost of modifying the cantilever tip, and the inconvenience of working with a sophisticated instrument designed for measuring atomic force rather than moving a droplet on a fiber.

The method developed in this article is based on forming a compound droplet of two immiscible fluids by using ferrofluid (referred to here as secondary fluid) in a magnetic field to detach the non-magnetic droplet (referred to here as the primary fluid e.g., a water or an oil droplet) from a fiber in a direction normal to the fiber axis. It is quite easy to implement and is flexible with regard to varying the droplet fluid.

Numerically, the energy minimization approach has been used to solve for 3-D shape of the droplet and predict the detachment force for that fiber-droplet system to validate our experimental results. That is done by using a public domain software called Surface Evolver (SE) [Brakke 1992]. The finite element code, Surface Evolver (SE), is able to solve for the minimum-energy shape of an interface between two immiscible fluids. The general form of the energy equation E being integrated in thecode can be expressed as $E = \sigma_{LG}\, dA_L + \rho\, g\, h \int dV - \sigma_{LG}\, \cos\theta \int_{SL} dA$ in which A, σ, θ and V are the area, surface tension, YLCA, and volume, respectively. This approach gives us the equilibrium shape of the droplet and consequently the ability to calculate the detachment force which is the force required to detach a droplet from the solid surface.

1.2 Droplet Interactions with Granular Coatings

The self-cleaning properties of Lotus leaves have motivated many studies in the past decade to investigate the superhydrophobicity effect. Fluid interaction with a surface is affected by both the chemical composition and the geometrical attributes of the surface. Substrate topology can potentially alter the wetting behavior of the substrate of a given chemical composition [Extrand 2005; Moghadam *et al.* 2019]. Thus, it is important to study the role of substrate topology on the liquid mechanism. Surface wetting behavior is categorized into two categories: hydrophobic surface (contact angle above 90°) and hydrophilic surface (contact angle below 90°). The Superhydrophobicity is known for having contact angles exceeding 150° and low contact-angle hysteresis. Examples of such surfaces in nature are the lotus leaves and water striders. Superhydrophobic (SHP) surfaces, are known for their ability to reduce the area of contact between water and the solid surface. SHP coatings can be used for drag reduction [Davis and Lauga 2009; Aziz and Tafreshi 2018], oil-water separation [Lee *et al.* 2011], self-cleaning and anti-icing [Extrand 2011], underwater protection of electronic devices [Ganne *et al.* 2016], water harvesting [Park *et al.* 2013], and heat transfer [Geraldi *et al.* 2016] among many other applications.

Superhydrophobic surfaces are often produced by imprinting micro- or nano-scale structures on a hydrophobic substrate or by chemically treating the surface of a substrate with the desired roughness as mentioned before [Shirtcliffe *et al.* 2004; Lee *et al.* 2008]. In addition, SHP surfaces may also be used to reduce the drag force on an object submerged in moving water due to its ability to entrap air [Ou and Rothstein 2005; McHale *et al.* 2009; Lee *et al.* 2008; Dong *et al.* 2013]. When the pores in an SPH surface are completely filled with air, the surface is considered to be in Cassie state (fully dry). If the hydrostatic pressure over the surface is too high, water may start penetrating into the pores compressing the entrapped air and finally fully wets the surface (Wenzel state) [Wenzel 1963; Cassie and Baxter 1944]. Depending

on surface geometry and pressure, the AWI can ingress into the space between the grooves to allow the Wenzel state (fully wetted), the Cassie state (fully dry), or a series of transition states in between the two extreme states to prevail over the surface.

Understanding the physics of droplet deposed over rough surfaces and the dynamics of wetting behavior have received a significant attention for years [Yang 2010; Savita *et al.* 2007; Charvet *et al.* 2008] to study the stability of droplet conformations, contact angles, and droplet geometry on different microstructures. The wetting phenomena of droplet-on-semicircular and curved microstructures have reported [Tie *et al.* 2014; Lu *et al.* 2015; Tie *et al.* 2015] on determining the droplet shape and the contact angle. But, these works focus on measuring the contact angle of a droplet sitting on 2D microstructures (which is different from the contact angle that the same liquid would form on a 3D pattern).

Our research dedicated for modeling a droplet siting on granular protrusions in 3D pattern (that resembles the natural SHP surfaces) arranged over a flat surface in a uniform configuration and measure the apparent contact angle (ACA) of that droplet. Two fundamentally different conformations of macroscopic droplets has been studied (Wenzel and Cassie conformations) for different shapes of the granular microstructure (hemispherical or spherical particles), particles radius, particles contact angle, solid volume fraction (SVF), and droplet volume.

To predict the droplet shape experimentally, the surface roughness (spherical and hemispherical particle) has been achieved by 3D printing. It was a challenge to get a spherical shape of the roughness by 3D printing. The surface was not perfectly curved. So, given the complexity of the problem, the current study is limited to study the effects of granular SHP coatings on the droplet shape numerically. The droplet transition from a fully dry state (Cassie state) to fully wet state (Wenzel state) is studied as a function to the roughness wavelength.

1.3 Overall Objective of This Thesis

This study is intended to develop experimental and theoretical models to study droplet interactions with fiber in terms of interfacial forces. This information is crucially important for understanding the dynamics, coalescence, and migration of liquid droplets in fibrous structures. The main contribution of this study is expected to provide quantitative predictions for the performance of droplet-fibers system in many applications. Also, our study is focused on study multiphase droplets (magnetic and non-magnetic droplets) detaching from a fiber with different wettabilities.

We develop experimental and theoretical methods for predicting the force required to detach a droplet normal from the fiber. The proposed work begins with studying the interactions between a magnetic droplet (ferrofluid droplet) and a fiber with different contact angle and moves on to include multiphase droplets of magnetic and non-magnetic droplets (e.g. ferrofluid and oil droplets) on the fiber. The effect of different parameters (such as the fiber diameter, fiber contact angle, relative size of fiber and droplet) on the force required to detach the multiphase droplet from the fiber are studied thoroughly.

Also, we study a droplet interaction over granular surface in Cassie and Wenzel states and predicting the apparent contact angle of a droplet sitting on particles for different geometric parameters such as particles diameters, particles contact angles and solid volume fraction (SVF). We expand that work to study the displacement force of the droplet in Cassie state by applying horizontal force for different geometric parameters.

Chapter 2. Universal Expression for Droplet-Fiber Detachment Force

2.1 Introduction

Formulating the physics of droplet adhesion to a fiber is interesting intellectually and important industrially. A typical example of droplet–fiber interactions in nature is the dew formation on spider webs or cactus spines, where droplets first adhering to such fibrous structures when they are small, but then move along the fibers or detach from the fibers when they grow larger (Bai *et al.* 2010; Bai *et al.* 2012; Malik *et al.* 2016). Obviously, quantifying the force of adhesion between a droplet and a fiber is crucial in designing fog-harvesting media (Xu *et al.* 2016; Weyer *et al.* 2017; He *et al.* 2015; Seo *et al.* 2016; Xing *et al.* 2017), filtration media for liquid–gas or liquid–liquid separation (Contal *et al.* 2004; Patel and Chase 2014; Kampa *et al.* 2014; Song *et al.* 2014), functional textiles (Michielsen and Lee 2007; Kleingartner *et al.* 2015), and open microfluidics system among many other applications (Gilet *et al.* 2009; Michielsen *et al.* 2011; Weyer *et al.* 2015; Pan *et al.* 2018).

Starting with the pioneering work of Carroll four decades ago (Carroll 1976; Carroll 1991), droplet equilibrium shape on a single fiber (i.e., symmetric barrel, asymmetric barrel, or clamshell) has been vastly studied by various groups (Rebouillat *et al.* 1999; McHale *et al.* 2001; McHale and Newton 2002; Hanumanthu and Stebe 2006; Ruiter *et al.* 2012; Mei *et al.* 2013; Eral *et al.* 2011). However, only a few studies have been focused on quantifying droplet detachment force from a fiber (Wu *et al.* 2010; Sahu *et al.* 2013; Davoudi *et al.* 2016; Mullins *et al.* 2007; Hotz *et al.* 2015; Amrei *et al.* 2016; Weyer *et al.* 2017), and each study has been conducted for a specific set of parameters (e.g., droplet volume, fluid surface tension, fiber diameter, fiber contact angle (CA)…) different from those of other studies. The study

reported here is a combined experimental–computational investigation focused primarily on measuring the force required to detach a droplet from a fiber in a direction normal to the fiber axis (referred to here as droplet detachment force) for fiber–droplet systems with different dimensions or Young–Laplace contact angles (YLCAs), for the first time. In addition, the current chapter presents easy-to-use mathematical expressions that can be used to predict the force needed to detach a given droplet from an arbitrary fiber using existing data obtained for a fiber–droplet system with different dimensions or physical properties.

The remainder of this chapter is organized as follows. Our experimental procedure and computational method are discussed in Sec. 2.2. Our experimental data are presented and compared with their computational counterparts, in Sec. 2.3. A detailed force balance analysis is given in Sec. 2.4 for forces acting on a droplet–fiber system. Section 2.5 presents different equations for force estimation and proposes a final universally applicable expression for predicting droplet detachment force from a fiber. This section is followed by our conclusions in Sec. 2.5.

2.2 Approaches

In this section, we outline the basics of the experimental and computational approaches considered here to quantify the force required to detach a droplet from a fiber.

2.2.1 Measuring droplet detachment force

Previous experiments on droplet detachment from a fiber were chiefly driven by either an air-flow (Sahu *et al.* 2013; Davoudi *et al.* 2016) or an external mechanical device like an atomic force microscope (AFM) cantilever (Mullins *et al.* 2007; Hotz *et al.* 2015). Our group has recently developed a simple ferrofluid-based method to measure droplet detachment force from a fiber. This method allows for direct

measurement of detachment force, and it circumvents many complications that arise from using air-flow or an AFM cantilever. Like every other measurement methods however, the technique discussed here has some limitations as was discussed previously (Amrei *et al.* 2016).

Figure 2.1a shows a schematic diagram of our experimental setup consisting of a fiber with a diameter of 381 μm (Trilene XL smooth casting fishing line) mounted on a 3D printed holder placed on a Mettler Toledo XSE105 weight measurement scale. An Era NE-300 syringe pump was used to produce ferrofluid (EMG508, Ferrotech, USA) droplets with desired volumes. The droplet was then deposited gently on the fiber and the scale was zeroed. Droplet evaporation was minimized by using the draft shields of the balance and the droplets were imaged using a Nikon D3100 camera connected to a PC. A nickel-plated axially-magnetized cylindrical permanent magnet with a diameter of 1.5 cm and a length of 3 cm (purchased from K&J Magnetics) was used to exert an external force on the droplets. Close attention was paid to ensure that the magnet and the droplet are perfectly aligned as the magnet is brought closer to the droplet–fiber system. As the magnet travels toward the droplet, the scale shows increasing weights, i.e., increasing magnetic force on the droplet (note that the long 3D printed holder prevents the magnet from affecting the readings of the scale), and the droplet shape changes accordingly, as shown in Fig. 2.1b. In this figure, Image 1 shows the droplet initially under the gravity. Images 2 and 3 show the droplet under the influence of higher magnetic forces, causing the triple contact-line (CL) and the apparent CA to change. More specifically, Image 3 corresponds to the moment when the magnetic force is strong enough to detach the droplet (no force increase is required form here on). At this force, the CL spontaneously shrinks until it reaches a minimum value before the droplet is detached as shown in Image 4, 5 and Image 6. As expected, a small residue will be left on the fiber as shown in Image 7.

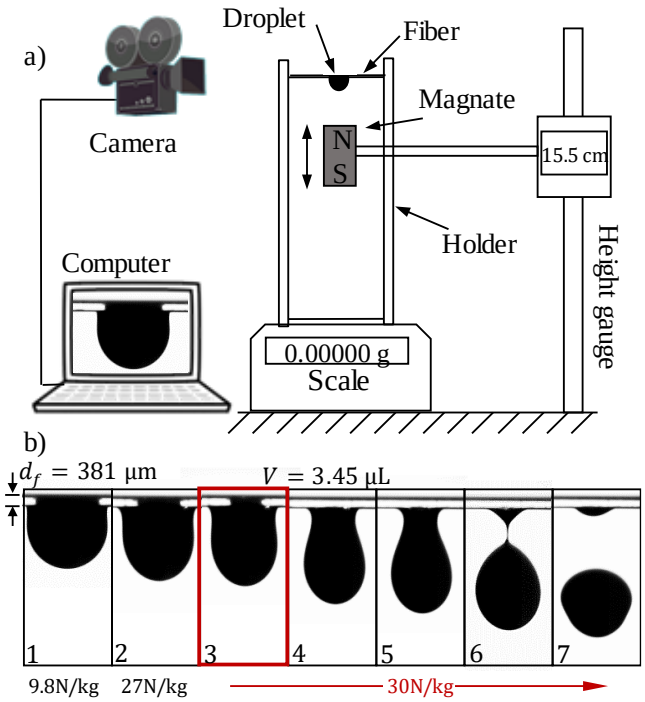

Figure 2.1: Schematic of the experimental setup is shown in (a). High-speed images taken from a ferrofluid droplet with a volume of 3.45µL on a fiber with a radius of $r = 190.5$ µm are shown in (b). The external body force is increased from image 1 to image 3 but then kept constant. Image 3 (marked also with a red frame) shows the final state of droplet equilibrium under an external force (the final equilibrium shape before the spontaneous detachment starts, corresponding to the largest external body force that can be applied to a droplet at equilibrium).

The detachment scenario shown in Fig. 2.1b, is qualitatively similar to the observations reported in Ref. (Tadmor *et al.* 2017) for droplet detachment from a flat surface using a centrifugal force. At the moment of droplet detachment from the fiber, the scale reading reaches a peak value that is taken here as the detachment force. To avoid missing the force at the moment of droplet detachment, the digital display of the scale was video-taped during the experiment and the maximum force was obtained from the recorded videos. The detachment force per unit mass of the droplet was calculated as

$$F_z = \left(\frac{m_{ex}}{\rho V} + 1\right) g \tag{2.1}$$

where m_{ex} is the peak value (max mass) read from the scale at the moment of detachment. In this equation, ρ, V and g are the droplet density, droplet volume and gravity, respectively. The surface tension and

density of the water-based ferrofluid used in our experiments were measure to be 0.0649 N/m and 1050 kg/m^3 at 25 °C, respectively.

2.2.2 Measuring fiber Young–Laplace contact angle

Neither the material of the fiber (fishing line) used in our experiments nor its surface chemistry (e.g., having any sort of surface coating) was reported by the manufacturer. Therefore, we designed an experimental setup to determine the Young–Laplace contact angle (YLCA) of the fibers used in our experiments. To do so, we placed the fiber in the middle of a glass capillary tube and used the assembly as a fluid height-rise experiment. However, as the setup required a relatively large volume of ferrofluid (costly considering the required repetitions for each experiment), we conducted the experiment using DI water. Once the YLCA of DI water θ_w with the material of the fiber was obtained, we used the following equation from Refs. (Good and Girifalco 1960; Sullivan 1981) to obtain the YLCA θ of the ferrofluid (knowing the surface tension of DI water σ_w and that of the ferrofluid σ).

$$\cos\theta = -1 + \left(\frac{\sigma_w}{\sigma}\right)^{1/2} (\cos\theta_w + 1) \tag{2.2}$$

To do the experiment, the capillary tube was first brought into contact with DI water, and water was allowed to rise into the tube. Measuring the water height rise in the tube h_1, and knowing the inner diameter of the tube d_t as well as the physical properties of the DI water, we obtained an YLCA for the tube using Jurin's law (Jurin 1719),

$$\theta_t = \cos^{-1}\left(\frac{h_1 d_t}{4\,a^2}\right) \tag{2.3}$$

where $a = \sqrt{\sigma_w/(\rho_w\, g)}$ is a dimensionless number called capillary length scale, and ρ_w is density of DI water. Next, the fiber with the unknown YLCA was placed inside the tube (see Fig. 2.2a) and the experiment was repeated to obtain a new height rise value h_2. Writing the balance of forces acting on the air–water interface (AWI) inside the tube, one can obtain

$$\rho_w\, g\, h_2\, A = \pi\, \sigma_w\, (d_f \cos\theta_w\ + d_t\ \cos\theta_t) \tag{2.4}$$

where $A = \frac{\pi}{4}(d_t^2 - d_f^2)$ is the projected area of the annular AWI. Rearranging Eq. (2.4) to calculate fiber's YLCA with water θ_w, we obtain

$$\theta_w\ = \cos^{-1}\left(\frac{h_2(d_t^2-d_f^2)}{4\,a^2\,d_f} - \frac{d_t\cos\theta_t}{d_f}\right) \tag{2.5}$$

Using Eq. (2.5), we found an YLCA of 69° for the DI water with the material of the fiber (based on an average vertical height rise value of about 12.7 mm with a small standard deviation over five repetitions). Using water YLCA in Eq. (2.2) along with the known surface tension values, we obtained an YLCA of $\theta = 65^\circ$ for the ferrofluid.

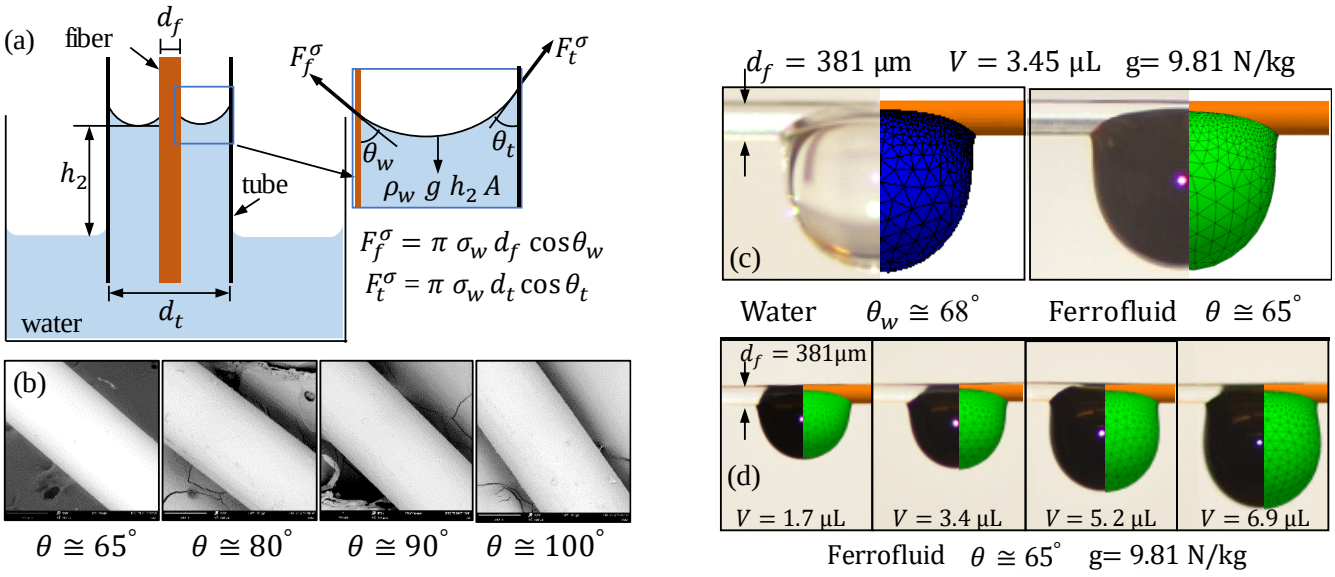

Figure 2.2: Schematic of our height rise experiment is shown in (a) along with the capillary forces applied by the fiber F_f^σ and by the tube F_t^σ on the air–water interface. SEM images of original and FDTS-coated fibers are shown in (b) with their corresponding YLCAs. Water and ferrofluid droplet profiles (under gravity) from simulation and experiment are compared to one another in (c) for a droplet volume of 3.45 µL on a fiber with $r = 190.5$ µm. Similar comparison is also given for ferrofluid droplets with different volumes $1.7\ \mu L < V < 6.9\ \mu L$ on the same fiber in (d).

As was discussed earlier in the introduction section, our main objective in this chapter is to determine the effects of YLCA on droplet detachment force from a fiber. Therefore, to create fibers with different YLCAs but identical diameters, we coated our fibers with heptadecafluoro-1,1,2,2-tetrahydrodecyl trichlorosilane (FDTS), which has been shown to be effective and stable in increasing the hydrophobicity of a polymeric surface in room temperature (Solmaz *et al.* 2008; Lin and Yang 2009). To do so, about 1 m of the fishing line was curled up into a spiral shape and mounted on a small stand inside a petri dish (to prevent the fishing line to touch the bottom of the dish or itself). An FDTS droplet was then placed in the middle of the dish far from the fibers using a syringe. The lid was closed to allow FDTS to evaporate in the sealed environment of the petri dish and to deposit on the fiber over a given exposure time (12 hours). We obtained average YLCAs of about 70°, 80°, 90°,and 100° by varying the volume of the FDTS droplet from about 10 μL to about 25 μL. Figure 2.2b shows SEM images of clean and coated fishing lines. Fiber's YLCA with ferrofluid is also added to the figure for each case.

To further refine and examine the accuracy of our YLCA measurements, we also developed an image-based method to determine the YLCA of the fibers with ferrofluid. With the imaged-based method, we first deposited a droplet with a known volume and physical properties on the fiber (with the unknown YLCA) and imaged the droplet from a front view. We then simulated the same droplet using the Surface Evolver code (see the next section for details about the simulations) but considered different YLCAs for the fibers. We then compared images (profile and apparent CA) of the simulated droplets with those from experiment to obtain the YLCA of the fiber. To benchmark this method, we measured the YLCA of DI water with the uncoated fiber and compared it with the results we obtained from the height rise test (i.e., $\theta_w = 69^{\circ}$). As can be seen in Fig. 2.2c, the image-based method resulted in an average YLCA of 68° between DI water and the fiber, which is within 2% margin of error relative to the height rise method. Likewise, ferrofluid droplets with different volumes $1.7\ \mu L \leq V \leq 6.9\ \mu L$ were placed on the same fiber

under the gravity, and their images were compared to those obtained from their corresponding simulations with fibers of different YLCAs. A YLCA of $\theta \cong 65^{\circ}$ was found for the ferrofluid regardless of the volume of the droplet considered for the experiment/simulation (see Fig. 2.2d).

2.2.3 Modeling droplet shape under an external body force

Numerical simulation is considered in our work to complement our experimental observations by providing detailed information with regard to the interplay between the forces acting on a droplet as it detaches from a fiber. Our simulations are conducted using the finite element Surface Evolver (SE) code (Brakke 1992), after the fiber–droplet system is properly defined for the solver. SE minimizes the total energy of the droplet–fiber system toward the equilibrium droplet shape (Bedarkar and Wu 2009). Our simulations start by placing a cubical body of fluid with a given volume on the fiber and allowing it to evolve to reach a 3D shape expected from the droplet at equilibrium (see Refs. (Amrei *et al.* 2017; Aziz *et al.* 2017; Venkateshan and Tafreshi 2018)). An external body force is then applied to the droplet in a direction normal to the fiber, and the force magnitude is incrementally increased until no equilibrium shape can be found for the droplet. The maximum force for which an equilibrium state for the droplet was obtained is considered as the detachment force in our study.

2.3 Experiment–Simulation Comparison

Fibers with different YLCAs ranging $65^{\circ} \leq \theta \leq 100^{\circ}$, but a fixed radius of $r = 190.5$ μm were prepared according to the procedure described in Sec. 2.2 and used here to study the effects of fiber YLCA on droplet detachment force. Figure 2.3a shows our experimental and computational detachment force per unit mass of the droplet versus droplet volume V, non-dimensionalized using fiber radius r cube. Each experiment was repeated multiple times to reduce the error associated with the experiment, and the results were averaged to obtain a representative detachment force.

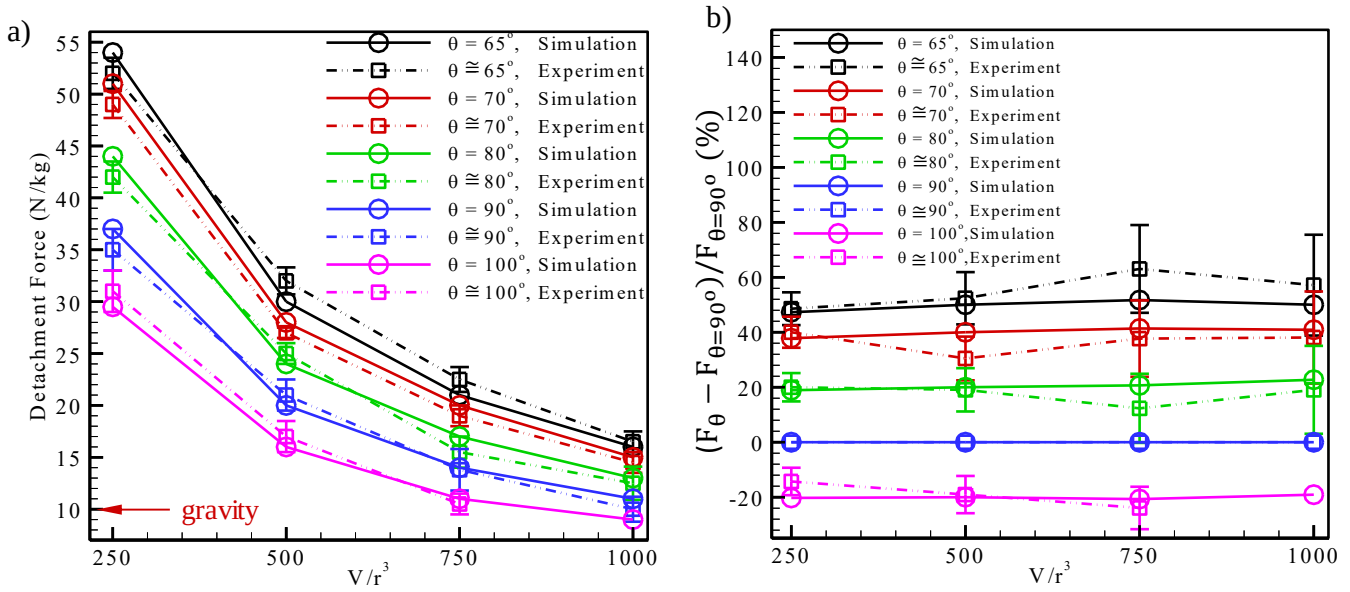

Figure 2.3: Droplet detachment forces from experiment and simulation are compared with each other in (a) for different droplet volumes on fibers with a fixed radius of 190.5 μm but different YLCAs. Detachment forces at different YLCAs are compared to that at $\theta = 90^{\circ}$ and presented in relative percent change in (b) for better comparison.

Despite the expected imperfections in the experiments (e.g., possible non-uniformity of the coating, errors in producing droplets with the small desired volume, the scale sensing and displaying the detachment force at the exact moment of detachment…), the predicted and measured detachment forces are in good agreement. It can be seen in this figure that the detachment force per unit mass of droplet decreases as droplet volume or YLCA increases. In other words, it is easier to detach a droplet from a fiber when the droplet is large or when the fiber is more phobic, as expected. We plotted the change in the droplet detachment force for all YLCAs relative to the case with $\theta \cong 90^{\circ}$in Fig. 2.3b. It can be seen that effects of YLCA does not diminish with increasing the droplet size (note that the simulation and experiment results for $\theta \cong 90^{\circ}$ are above each other as the results are plotted relative to the case with $\theta \cong 90^{\circ}$). Note that, for droplet $\frac{V}{r^3} = 1000$, and $\theta \cong 100^{\circ}$, gravity is enough to detach the droplet, and so no experimental data are included in Fig. 2.3 for this case.

2.4 Force Balance Analysis

In this section, we present a detailed analysis of the forces acting on a droplet deposited on a fiber. For such a droplet, we define the local apparent CA θ_i^{app} as the angle between the tangent to the droplet along the droplet–fiber CL and the horizontal plane. Figure 2.4a shows the apparent CA at the two extreme positions: longitudinal θ_L^{app} (viewed from a direction parallel to the fiber) and transverse θ_T^{app} (viewed from a direction normal to the fiber). The transverse and longitudinal apparent CAs at the moment of detachment (critical transverse and longitudinal apparent CAs) are shown in Fig. 2.4b, for a droplet with a volume ratio of 1000 and a fiber radius of 190.5 μm but with two different YLCAs of 65° and 90°.

Figure 2.4c shows the local critical apparent CAs (at the detachment moment) along the entire length of the CL for a droplet with a volume ratio of 1000 and a fiber radius of 190.5 μm and a YLCA ranging from 65° to 100°. It can be seen that apparent CA varies along the CL from a minimum value corresponding to θ_T^{app} to a maximum value corresponding to θ_L^{app}. Moreover, critical apparent CA is larger for fibers with larger YLCAs. To also study the effects of droplet volume, critical apparent CAs are compared for two droplets with different volumes ratio of 250 and 1000 in Fig. 2.4d (detachment forces are reported in the insets). Larger critical apparent CAs can be seen for the larger droplet (heavier droplets hang lower). In these figures, L is the total length of the CL for a clamshell droplet and L_i is the local position in the y-direction measured from the left corner in a transvers view of the droplet (red dot of the inset in Fig. 2.4c). Recognizing the fact that measuring the local droplet apparent CA on a fiber θ_i^{app} is an experimental challenge, here we propose an easy-to-use expression to obtain an approximate average value for the apparent CA of a droplet on a fiber,

$$\theta_{avg}^{app} = \frac{1}{3}\theta_T^{app} + \frac{2}{3}\theta_L^{app} \tag{2.6}$$

This expression is proposed based on the trend of variation of θ_i^{app} along the CL as shown in Figs. 2.4c and 2.4d. Predictions of this expression are also added to Fig. 2.4c (the solid lines) for $\theta = 65^{\circ}$ and $\theta = 90^{\circ}$, and they are in very good agreement with θ_{avg}^{app} calculated directly from the simulations (dashed lines).

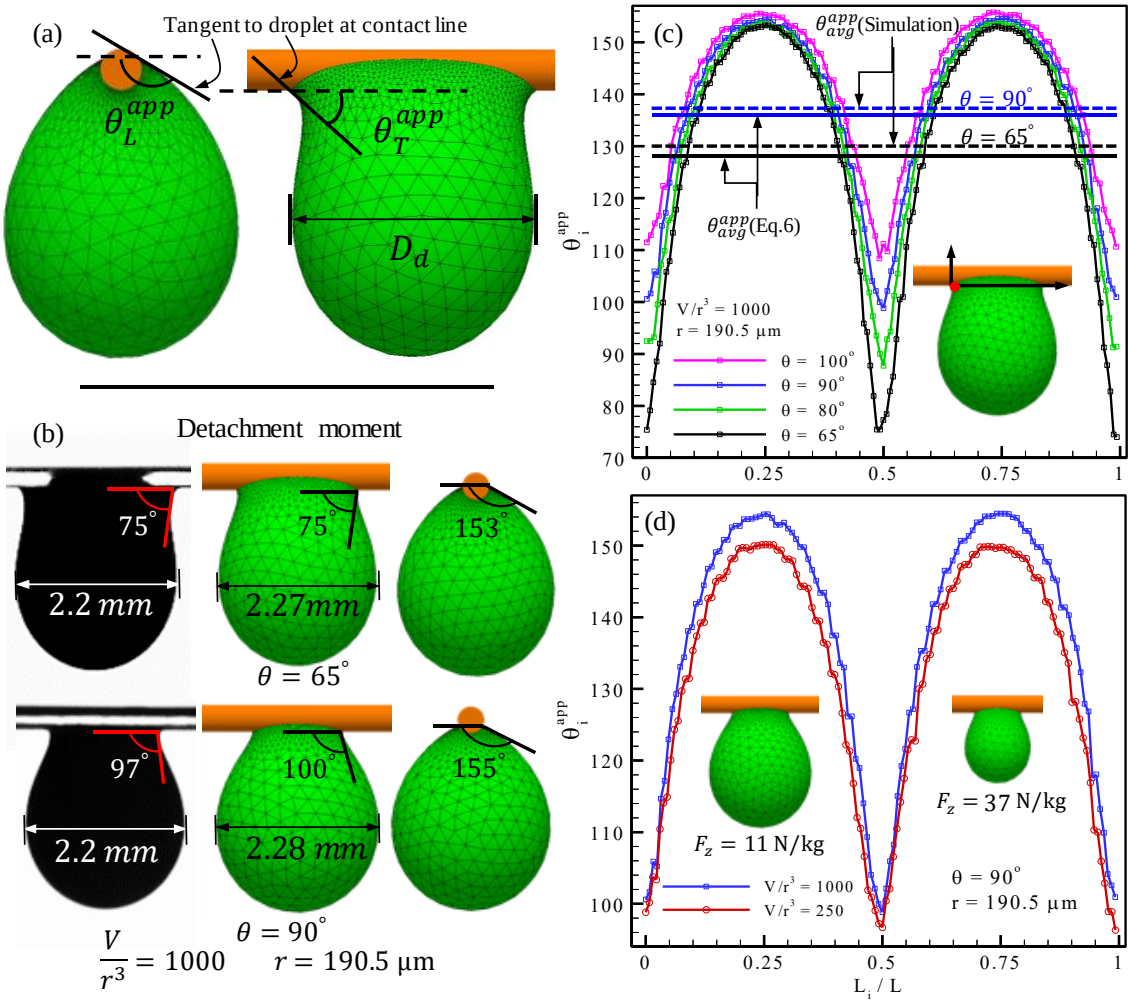

Figure 2.4: Longitudinal θ_L^{app} and transverse θ_T^{app} apparent contact angles are shown in (a) for a droplet with a volume ratio of $\frac{V}{r^3} = 1000$ on a fiber with a radius of r =190.5 µm and a YLCA of $\theta = 30^{\circ}$ at its final equilibrium state (under a detachment force of $F_z = 22.5$ N/kg). Comparisons between experimental and computational droplet profiles (apparent contact angle when possible) are given in (b) for the same droplet deposited on fibers with different YLCAs of $\theta = 65^{\circ}$ and 90°. Variation of the local apparent contact angle θ_i^{app} along the droplet contact line at the detachment moment is shown in (c) for different YLCAs. Average apparent contact angles θ_{avg}^{app} from the simulation and Eq. (2.6) are also added for comparison. Variation of the local apparent contact angle θ_i^{app} is also shown in (d) for droplets with different volumes on a fiber with a YLCA of $\theta = 90^{\circ}$ at the moment of detachment.

For a liquid droplet to remain on a fiber, it must be in a mechanical equilibrium state. Considering a free body diagram for the droplet (see Figs. 2.5a and 2.5b), the upward component of the capillary force $f_\sigma^\perp$ (N) along the CL should balance the external body force on the droplet f_z (N) plus the downward component of the surface reaction force to the droplet pressure (exerted on the fiber wetted area) f_p (N). In other words,

$$f_z = f_\sigma^\perp - f_p = \int_L \sigma \cos\alpha \, dL - f_p \tag{2.7}$$

where α is the local angle between the tangent to the droplet's surface at the CL and the vertical reference plane along the fiber. The vertical pressure force acting on fiber's wetted area can be calculated as

$$f_p = \int_L x\,(p_o - \rho\, F_z\, z)dy \tag{2.8}$$

where p_o is the pressure inside the droplet at $z = 0$ and $\rho\, F_z\, z$ is the change in pressure due to the body force per unit mass F_z at a height z (z is the coordinate of the points on the CL, and the body force is a downward force). Note that the second term in the integrand would become zero if the CL was planar, like the case of a droplet on a flat surface. In the above calculations, the length of the CL L is obtained from the simulations, but, it can also be estimated using Eq. (2.9), assuming an elliptical shape for the CL, i.e.,

$$L_e = 2\pi \sqrt{\frac{(\beta\, r)^2 + (l_f/2)^2}{2}} \tag{2.9}$$

In this equation, β (in radian) is the azimuthal angle between the negative vertical axis and the top of the CL on the fiber and l_f is the transverse projection of the wetted length of the fiber on its lower side (see the inset of Fig. 2.5c). Figure 2.5c, compares the actual length of the CL with the estimation obtained using Eq. (2.9) for droplets with two different volumes.

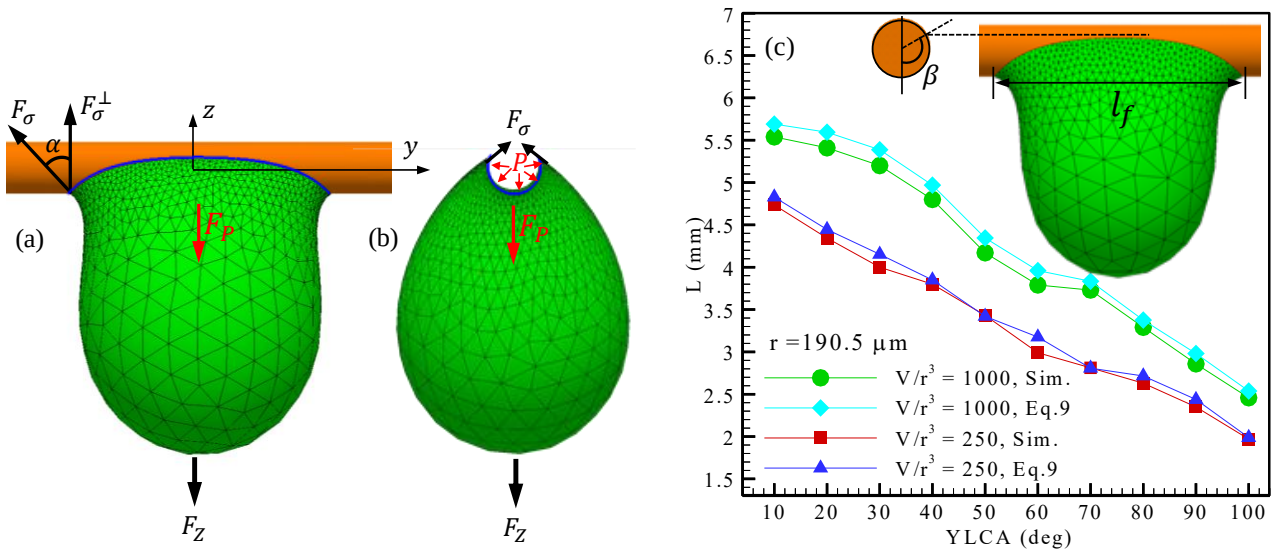

Figure 2.5: Free body diagrams are given in (a) and (b) for a droplet on a fiber at the equilibrium. The upward component of capillary force $F_\sigma^\perp$ along the contact line should balance the external body force on the droplet F_z as well as the downward component of the surface reaction force to the droplet pressure F_p (exerted on the fiber's wetted area). In these figures $\frac{V}{r^3} = 500$, $r = 190.5$ µm, $\theta = 30^\circ$, and $F_z = 40$ N/kg, Contact line total length is obtained from simulations and Eq. 2.9 and compared with one another in (c) for different droplet volumes. Fiber's wetted length l_f and azimuthal angle β and are shown in the inset figure.

For the simulations reported here, special attention was paid to ensure that the numerical results are mesh-independent, as predicted capillary forces may depend mesh density around the CL if a coarse mesh is used. One should also ensure that predicted capillary forces balance the pressure forces in the absence of a body force on the droplet. This was done by varying the mesh density along the CL and monitoring its impact on the results for each simulation.

To further investigate the effects of YLCA on droplet behavior, we compare capillary force and pressure force (both per unit mass of droplet) exerted on a droplet in Fig. 2.6a for two droplets with different volumes (shown with red and blue lines for $\frac{V}{r^3} = 250$ and $\frac{V}{r^3}$ =1000, respectively). The external force acting on the droplet is the gravity (9.81 N/kg). It can also be seen that, capillary force $F_\sigma^\perp$ (N/kg) is larger than the body force (the black dashed line). However, when the pressure force F_p (N/kg) is subtracted from the capillary force $F_\sigma^\perp$, the resultant force is almost equal to the body force. This clearly highlights

the importance of including pressure force in calculating the force of detachment (see also Refs. (Chen *et al.* 2013; Ataei *et al.* 2017). Figure 2.6b compares the capillary force, pressure force, and the detachment force for the same droplets discussed previously in Fig. 2.6a but at their own detachment moments. More interestingly, it can be seen that there exist some small differences between $F_\sigma^\perp - F_p$ and the detachment force F_z (besides numerical errors), and the differences decrease with increasing YLCA. This is because at low YLCAs, a detaching droplet breaks up into two volumes during the detachment process (leaving a small residue on the fibers, see Ref. (Aziz *et al.* 2018) for more details). This is in contrast to detachment from a hydrophobic fiber where no significant residue will be left (Aziz *et al.* 2018). In other words, when $F_\sigma^\perp - F_p$ (with $F_\sigma^\perp$ calculated at the CL and F_p calculated on the fiber wetted area) is greater than the cohesive forces holding the droplet together, it is impossible to detach the droplet from the fiber without leaving a residue behind. Formation of a neck (a minimum cross-sectional area along the z-direction) during detachment process is expected from a droplet that leaves a residue behind [Aziz *et al.* 2018]. Recalculating $F_\sigma^\perp - F_p$ based on the perimeter and cross-sectional area of the neck shows perfect agreement with the detachment force. Figure 2.6c shows the length of droplet CL on the fiber and the average angle between the capillary force and the vertical direction (averaged over CL) α_{avg} at the detachment moment. It can be seen that CL length and α_{avg} are greater for the larger droplet. It is also interesting to note that by increasing YLCA, α_{avg} first decreases slightly and then increases unlike CL which decreases monotonically (e.g., see Ref. (Carroll 1991)). The minimum point in the α_{avg} curve versus YLCA corresponds to the YLCA above which no neck formation is observed (forces balancing the external body force are at the droplet–fiber contact area rather the neck). Formation of a neck can be seen more clearly in Fig. 2.6d, where droplet maximum diameter D_d, neck's major axis (neck cross-section is elliptical) a_n, and fiber's wetted length l_f are compared to one another. It can be seen at the moment of detachment that a_n and l_f decrease with increasing YLCA while droplet maximum diameter D_d remains

unchanged (independent of YLCA). Detachment occurs from the neck when $a_n < l_f$ and from the fiber when a_n=l_f.

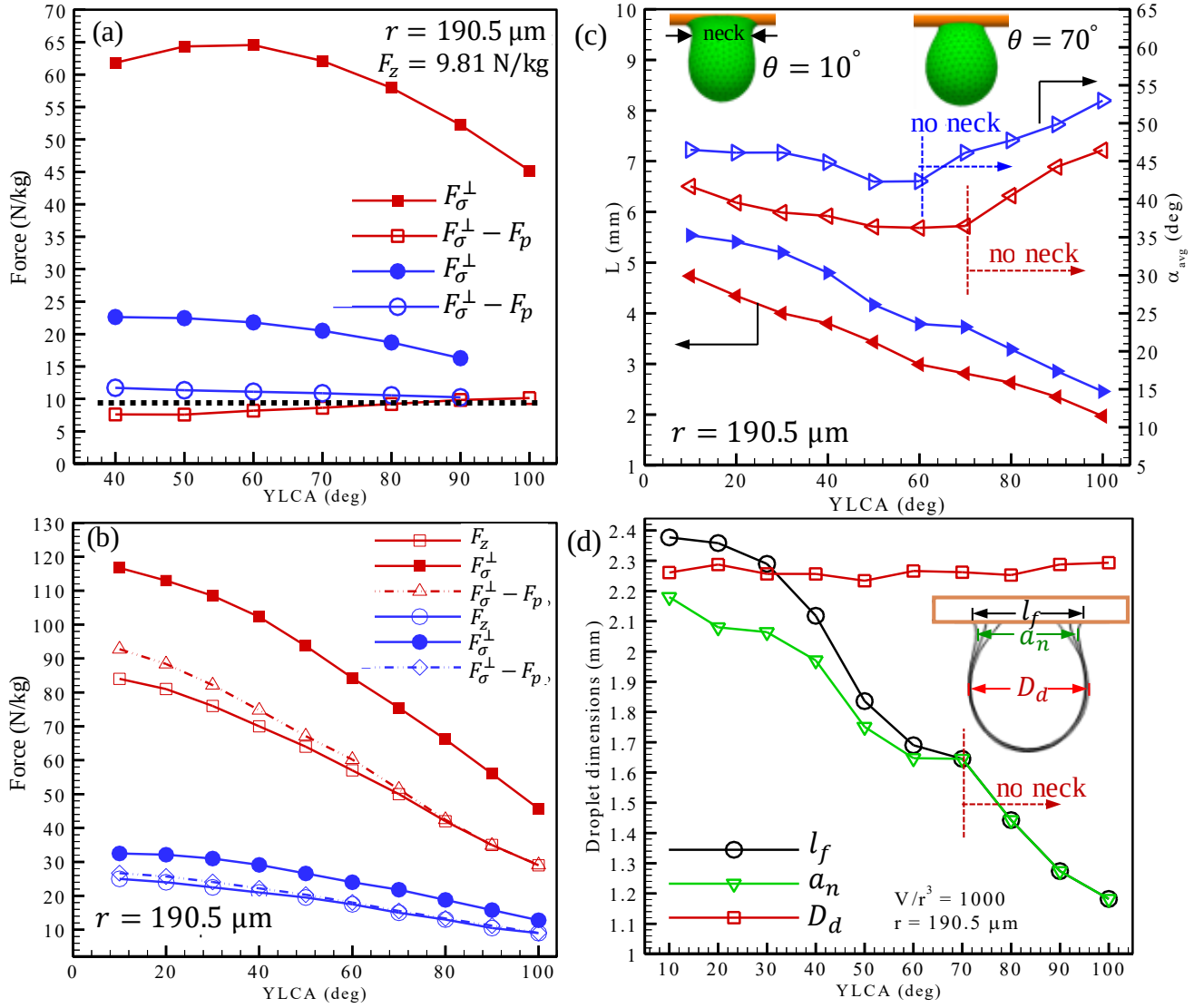

Figure 2.6: Vertical component of the capillary force $F_\sigma^\perp$ is shown for a droplet under the influence of gravity F_z = 9.81 N/kg on fibers with different YLCAs in (a). $F_\sigma^\perp - F_p \cong$ 9.81 N/kg is also added to the figure for comparison. The red and blue lines correspond to $\frac{V}{r^3} = 250$ and 1000, respectively (the droplet with $\frac{V}{r^3} = 1000$ cannot stay on the fiber with $\theta = 100^\circ$ under gravity). The figure in (b) shows similar results but for the detachment moment (i.e., different detachment force F_z for different YLCAs). Contact line length L and α_{avg} for droplets on fibers with different YLCAs at the detachment moment are shown in (c). Note the YLCA above which no measureable neck formation is expected from the detaching droplet. The droplet maximum diameter D_d, neck's major axis a_n (assuming elliptical neck cross-sections), and fiber's wetted length l_f are compared to one another in (d) as a function YLCA at the detachment moment.

The decrease in the detachment force with increasing YLCA (Fig. 2.6b) can also be explained using the data given in Figs. 2.6b and 2.6c. Consider Eq. 2.7 where detachment force is given as a function of pressure force f_p, the angle α, and contact line length L. It can be seen in these figures that F_p and α do not vary significantly with YLCA, but L decreases rapidly with increasing YLCA. Therefore, according to Eq. 2.7, one can expect the detachment force to decrease with increasing fiber's YLCA.

2.5 Predictive Correlations for Droplet Detachment Force

While studying droplet detachment from a flat surface is not the focus of the work presented here, such studies can be insightful in understanding the fundamental physics of droplet detachment from a fiber. In a recent study, (Tadmor *et al.* 2017), reported on droplet detachment from a flat surface mounted on a rotating tilted surface referred to as centrifugal adhesion balance (CAB) (see also Ref. (Tadmor *et al.* 2009)). Tadmor (Tadmor *et al.* 2017) used the Young–Dupré equation to relate the droplet detachment force to droplet CA and CL length at its final equilibrium state (the same state as has been considered in our simulations here or in our past work (Amrei *et al.* 2016; Amrei *et al.* 2017)). The Young–Dupré equation is given as

$$f_{Y-D} = p_T \, \sigma \, (1 + \cos\theta) \tag{2.10}$$

where p_T denotes droplet perimeter (i.e., CL length L in the current chapter) at the moment of detachment (see also Ref. (Bormashenko and Bormashenko 2013)). Using detachment force from their CAB experiment in Eq. 2.10, (Tadmor *et al.* 2017) obtained an angle close to the advancing CA for the surface on which the droplet was deposited. Obviously, obtaining the advancing CA for a receding CL was not expected, but (Tadmor *et al.* 2017) presented a justification for this observation on the basis of other studies in the literature (also see Ref. (Bormashenko 2013) for a discussion about using advancing CA in

the Young–Dupré equation). Most recently, an alternative relationship between detachment force and droplet CA has been derived by (Extrand 2017), as

$$f_{Rec} = p_T\ \sigma\ \cos\theta^R \tag{2.11}$$

where θ^R is the droplet receding CA. Extrand obtained this angle by equating the detachment force from the CAB experiment (normal to the surface) to the lateral surface force that anchors the perimeter of the drop to the solid surface (in the plane of the surface), but he did not include the pressure force (Eq. 2.8) in his calculations (Extrand 2017). Moving forward to the problem of droplet detachment from a fiber, we start with Eq. 2.10. To use this equation for detachment force prediction, one needs an appropriate CA and an appropriate characteristic length (e.g., CL length). In Table 1, we present predictions of droplet detachment force from a fiber using different combinations of these two parameters. In this table, *L* is the total length of the CL for a clamshell droplet on the fiber and L_{proj} is its projection onto a horizontal plane (normal to the direction of the external force). θ_{avg}^{app} is the average apparent CA (from Eq. 2.6), and D_d is the droplet maximum diameter at the moment of detachment (see Fig. 2.6d).

Table 2.1: Droplet detachment force f_z in (μN) for a droplet with a volume of $\frac{V}{r^3} = 1000$ deposited on a fiber with a radius of $r = 190.5$ μm is approximated using different expressions for different YLCAs, and compared with our experimental and computational results. Matching data are highlighted in grey.

YLCA, θ / f_z (μN)	10°	50°	70°	80°	100°	120°
f_z from experiment	NA	NA	**105 ± 1**	**91 ± 0.8**	NA	NA
f_z from simulation	**181**	**141**	**109**	**94**	**65**	**39**
$f_z = \sigma L\ (1 + \cos\theta)$	708	444	325	251	144	66
$f_z = \sigma L_{proj}\ (1 + \cos\theta)$	670	429	317	245	141	65
$f_z = \sigma L_{proj}\ (1 + \cos\theta_{avg}^{app})$	237	125	80	64	38	16
$f_z = 2\sigma D_d\ (1 + \cos\theta_{avg}^{app})$	**183**	**139**	**102**	**92**	**64**	**38**
$f_z = L_e\ \sigma\ sin\,\theta_{avg}^{app} - A_e\ \frac{2\sigma}{0.5\ l_f + r}$	Neck	Neck	**112**	**98**	**68**	**38**

It can be seen in Table 1 that only two of these expressions can predict the detachment force relatively accurately. The first equation (Eq. 2.12) is a simplified form of Eq. (2.7), i.e.,

$$f_z = \sigma\, L_e \sin\theta_{avg}^{app} - A_e\,(\frac{2\sigma}{r + 0.5\, l_f}) \tag{2.12}$$

where $A_e = \frac{\pi}{2}\beta\, r\, l_f$ is the projected wetted area and β (in radian) is the azimuthal angle (see Fig. 2.5c). Note that we propose Eq. 2.12 only for when a droplet detaches from a fiber without exhibiting a major neck formation. It is worth mentioning that, Eq. 2.12 may also be used to estimate droplet detachment force from a flat surface like those reported by Tadmor (Tadmor *et al.* 2017) as long as the detachment is without a neck formation. For instance, for a water droplet ($\sigma = 0.072$ N/m) with a CL radius of $R = 0.47$ mm on a hydrophobic microporous layers polytetrafluoroethylene (MPL-PTFE) surface, we obtained a detachment force of $f_z = 77$ μN in good agreement with the measurements reported in Ref. (Tadmor *et al.* 2017) when assuming $\theta_{avg}^{app} \cong 120^{\circ}$and using $2R$ instead of $r + 0.5\, l_f$ (circular wetted area).

Our second proposed equation is Eq. 2.13, which uses D_d as the characteristic length for its independence from YLCA and θ_{avg}^{app} (see Fig. 2.6d).

$$f_z = 2\sigma\, D_d\,(1 + \cos\theta_{avg}^{app}) \tag{2.13}$$

Despite their good predictions, Eqs. (2.12) and (2.13) require parameters that can only be obtained by conducting a droplet detachment experiment to image the droplet right before detachment (to obtain θ_{avg}^{app}, β, l_f, and D_d). In this concern, we combined Eq. (2.10) (proposed in Ref. (Tadmor *et al.* 2017)) with the expression developed in our previous work (Amrei *et al.* 2016; Amrei *et al.* 2017) for droplet detachment from fibers with different diameters or YLCAs to develop an equation for detachment force prediction, i.e.,

$$F_{z,2} = \left(\frac{r_1}{r_2}\right)^2 \frac{1+\cos\theta_2}{1+\cos\theta_1} F_{z,1} \tag{2.14}$$

With this equation one can predict the force needed to detach a droplet from an arbitrary fiber using the detachment force data $F_{z,1}$ obtained previously for a fiber–droplet combination with different dimensions and/or YLCA, but identical Bond numbers ($B_O = \frac{\rho g r^2}{\sigma}$, the ratio of the body forces to the capillary forces acting on a droplet). According to Eq. (2.14), going from droplet–fiber combination 1 to droplet–fiber combination 2, detachment force scales by a factor of $\left(\frac{r_1}{r_2}\right)^2 \frac{1+\cos\theta_2}{1+\cos\theta_1}$.

To examine the accuracy of this equation, we first measured the force needed to detach ferrofluid droplets of various volumes from a fiber with a radius of $r_1 = 266.7$ μm and an YLCA of $\theta_1 = 25^\circ$ (red circles in Fig. 2.7a). We then used the experimental (or computational) data obtained for droplet detachment from a fiber with a radius $r_2 = 190.5$ μm and an YLCA of $\theta_2 = 65^\circ$ (from Fig. 2.3a) and scaled them using Eq. 2.14. The scaled detachment forces are added to Fig. 2.7a (black squares), and they show excellent agreement with the forces obtained via direct measurement. We also repeated this exercise for $\theta_2 = 100^\circ$ (blue triangles) for further examination and obtained perfect predictions as can be seen in Fig. 2.7a. Examples of droplet profiles under the gravity and at the moment of detachment for $\frac{V}{r^3} = 250$ are given in Fig. 2.7b to better illustrate the differences between the size and wetting properties of the droplet–fiber combinations considered in this figure.

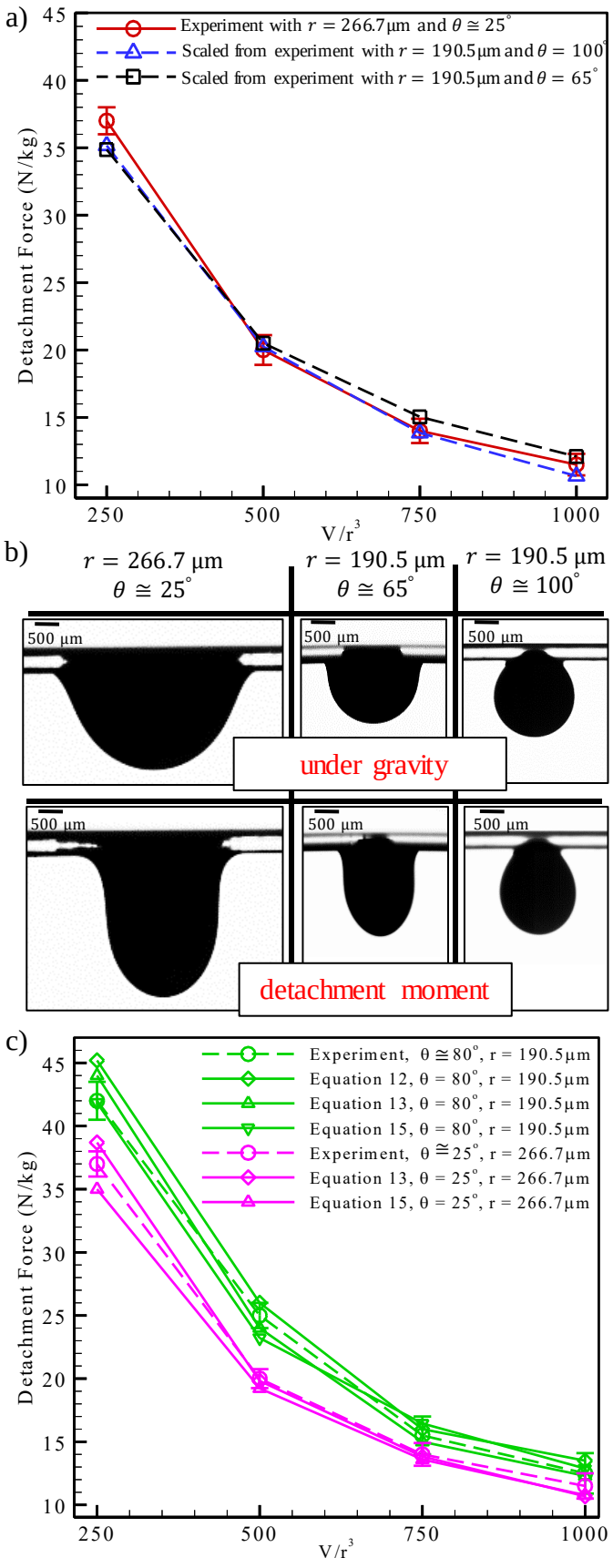

Figure 2.7: Detachment force obtained from experiment for droplets with different volumes on a fiber with a radius of $r = 266.7$ µm and a YLCA of $\theta \cong 25^{\circ}$ are shown with red circles in (a). Blue squares and black triangles are experimental data obtained for droplets on a fiber with a radius of $r = 190.5$ µm and YLCAs of $\theta = 65^{\circ}$ and 100°, respectively (Figure 2.3(a)), but they are scaled using Eq. (2.14) to predict the forces shown with red circles. The above droplet–fiber systems for $\frac{V}{r^3} = 250$ shown in (b) to better illustrate that the data shown with blue and black symbols where obtained from experiments conducted with droplet–fiber systems very different from the one used to produce the red symbols. Additional comparison is shown in (c) between experimental results and the prediction of Eqs. (2.12), (2.13) and (2.15) for $\theta = 80^{\circ}$ and $r = 190.5$ µm (green symbols) and for $\theta = 25^{\circ}$ and $r = 266.7$ µm (pink symbols). Note that for $\theta = 25^{\circ}$ and $r = 266.7$ µm droplet detachment involves neck formation and so Eq. (2.12) is not used for this case.

To further expand the usability of Eq. (2.14), we fitted a power-law equation ($F_{z,ref} = \varphi \left(\frac{V}{r_{ref}^3}\right)^{\xi}$ with $\varphi =$ 3,894 N/kg, and $\xi = -0.84$) to our experimental data obtained for the case of $\theta_{ref} = 90^{\circ}$ and $r_{ref} = 190.5 \times 10^{-6}$m (from Fig. 2.3a) and used the resulting expression in Eq. (2.14) as,

$$F_z = \left(\frac{r_{\text{ref}}}{r}\right)^2 \frac{\sigma}{\sigma_{ref}} \frac{\rho_{ref}}{\rho} (1 + \cos\theta)\, \varphi \left(\frac{V}{r^3}\right)^{\xi} \tag{2.15}$$

where $\sigma_{ref} = 0.0649$ N/m N/m and $\rho_{ref} = 1050$ kg/m^3 (all variables are in SI units). Figure 2.7c compares our experimental droplet detachment force from fibers with two different radii of $r = 266.7$ μm and $r =$190.5 μm having YLCAs of $\theta = 25^{\circ}$and $\theta = 80^{\circ}$, respectively, with predictions of Eqs. (2.12), (2.13), and (2.15) (Eq. (2.12) is only used for when droplet detachment occurs from a fiber without a major neck formation). Excellent agreement can again be observed between the predictions of these equations and the actual experimental data.

To further examine the accuracy of Eq. 2.15 for range of parameters outside those investigated experimentally, we conducted a series of numerical simulations for droplet detachment from fibers as small as 10 μm or as large as 1000 μm in radius. We considered silicone oil with a density of $\rho_{so} =$ 960 kg/m^3 and a surface tension of $\sigma_{so} = 0.02$ N/m as the fluid and varied the YLCA of the fiber from 10 to 160 degrees. As shown in Fig. 2.8, good agreement can be seen between the predictions of Eq. 2.15 and the results of numerical simulation for $20^{\circ} \leq \theta$. Droplet size for the simulations reported in this figure is $\frac{V}{r^3} = 250$ and $\frac{V}{r^3} = 1000$, for the fiber with the radius of 1000 μm and radius of 10 μm, respectively. Equation 2.15 has also shown perfect agreement with simulation results for droplet volumes different from those considered here.

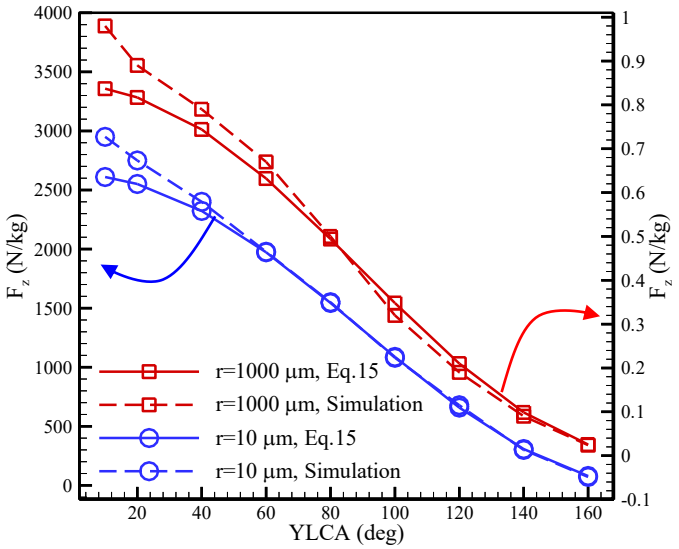

Figure 2.8: Comparison between simulation results and prediction of Eq. 2.15 for detachment force obtained for silicone oil droplets with a density $\rho = 960$ kg/m^3 and a surface tension $\sigma = 0.02$ N/m from fibers with different radii of 10 μm and 1000 μm. The red and blue lines correspond to $\frac{V}{r^3} = 250$ and 1000, respectively.

We also considered experimental data reported in the literature (although they are very scarce) to provide additional comparison. The work of (Tian *et al.* 2011) reported a detachment force of is 9.8 N/kg (i.e., gravity) for water droplets with a volume of $V = 1.95 \pm 0.12$ μL deposited on a nylon fiber with $r =$ 9 μm. Using the above information in Eq. (2.15), one can obtain a detachment force in close agreement with the reported data in Ref. (Tian *et al.* 2011) assuming a YLCA of $\theta = 60^\circ$ (no YLCA was reported in Ref. (Tian *et al.* 2011)). Equation (2.15) also provides good predictions for the experimental data reported by Ref. (Mullins *et al.* 2007) for oil droplet detachment from fibers made of different materials, but only after assuming a reasonable YLCA for the fibers used in their experiments (no YLCA was reported in Ref. (Mullins *et al.* 2007)).

2.6 Conclusions

Experiment and numerical simulation were conducted to study the effects of fiber diameter, fiber YLCA, and droplet properties on the force required to detach a droplet from a fiber. Experiment and simulation in good mutual agreement quantified the increase of droplet detachment force for any incremental decrease in YLCA in the range YLCAs considered $65^{\circ} < \theta < 100^{\circ}$ (see Fig. 2.3a).

Considering a free body diagram for a droplet at its final equilibrium state under an external force on a fiber, it was found that droplet pressure plays an important role in the balance of forces acting on the droplet. It was also found that average apparent CA of the droplet θ_{avg}^{app} is an important geometric parameter that can be used in predicting droplet's force of detachment. As this angle is hard to measure experimentally, an approximate but yet relatively accurate equation in terms of longitudinal and transverse apparent CAs (Eq. 2.6) is proposed to be used along with another approximate equation for the shape of the CL (Eq. 2.9) in estimating droplet detachment force (see Eq. 2.12). Varying YLCA for a given droplet–fiber system, it was found that there exists a YLCA above which detachment occurs before a measurable neck is observed in the droplet profile (see Fig. 2.6d). Unlike CL or wetted length l_f, droplet maximum diameter at the moment of detachment D_d was found to be independent of YLCA, and so it can be used in characterize the detachment force (see Eq. 2.13).

We proposed and examined the accuracy of a series of ad-hoc expressions relating droplet detachment force to its geometrical dimensions (obtained from imaging or simulating the droplet at its final equilibrium state before spontaneous detachment). Two expressions were found to be fairly accurate (Eqs. 2.12 and 2.13). To circumvent the need for conducting an experiment or running a computer simulation to obtain these geometric dimensions, we developed a mathematical relationship that uses an existing set

of detachment force data, obtained for an arbitrary droplet–fiber system, to predict the force of detachment for the droplet–fiber system at hand. To further facilitate the use of the above relationship, we used our own data to create a simple correlation for detachment force. This semi-empirical correlation (see Eq. 2.15) can be used for droplet detachment force prediction without the need for running an experiment or a computer simulation for YLCAs greater than about 20°.

Chapter 3. Simple Method for Measuring Intrinsic Contact Angle of a Fiber with Liquids

3.1 Introduction

Wettability is a measure of a surface tendency to remain in contact with a liquid, and it is often characterized using the Young–Laplace contact angle (YLCA), obtained by placing a small droplet on the surface and measuring the angle between the tangent to the droplet at the solid–liquid–air contact line (CL) and the surface (Tavana and Neumann 2007; Quere 2008; Bormashenko 2017). The two main methods commonly used for YLCA measurement (also referred to as the intrinsic contact angle of the surface) are the sessile-drop method and the Wilhelmy force method. For the sessile-droplet method, a small liquid droplet is placed on the substrate and the YLCA is either measured, between the base of the droplet and the tangent to the droplet surface at the CL, or calculated, from the sessile drop profile (Drelich 2013; Kalantarian *et al.* 2009; Bracco and Holst 2013). For the Wilhelmy method, the force needed to pull a partially-submerged vertical flat plate out of the liquid is measured and used to estimate the YLCA of the plate.

The ability to measure the YLCA of the material from which a fiber is made has significant value for many industrial applications such as fog harvesting (Seo *et al.* 2016; Shi *et al.* 2018), droplet–gas or droplet–liquid separation (Kampa *et al.* 2014; Sahu *et al.* 2013; Wurster *et al.*2015; Patel and Chase 2014; Wei *et al.* 2019), textiles/clothing (Michielsen and Lee 2007; Chen *et al.* 2010), microfluidics (Reznik *et al.* 2007; Weyer *et al.* 2015), and fuel cells (Gurau *et al.* 2006; Gauthier *et al.*2012), among many others. Applying the methods developed originally for flat plates, the YLCA of a fiber has also been measured using the Wilhelmy method and a modified version of the sessile-droplet method. Applying the Wilhelmy

method to a single fiber requires measuring the minute wetting forces exerted by a liquid on a partially submersed single fiber (Wu 1982; Tsai *et al.* 2014; Pucci *et al.* 2015; Hansen *et al.* 2017). The method therefore, requires quantitative information about the exact length and shape of the CL around the fiber, which is hard to obtain especially when the fiber is not perfectly cylindrical. Moreover, this method requires very sensitive equipment to measure the wetting force exerted on a minute fiber by a liquid. To apply the sessile-droplet method to a fiber, a small droplet is placed on a horizontal fiber and is imaged from the side view. The droplet should be very small so that it conforms to the shape of an axisymmetric barrel on the fiber (negligible gravitational effect). Since it is hard to locate the position of the CL on a small hydrophilic fiber (and thereby measure the contact angle (CA)), it has been proposed to obtain the inflection point of the barrel-shaped profile via image processing, and used that to geometrically predict the YLCA of the fiber (McHale *et al.* 1997; McHale *et al.* 1999; Rebouillat *et al.* 1999; McHale *et al.* 2001; Davoudi *et al.* 2018). This method obviously, requires the droplet to be very small (or it will not form an axisymmetric barrel-shaped profile) and the fiber to be hydrophilic. It is worth mentioning that the YLCA of a cylindrical (i.e., fiber) or a spherical surface can also be obtained by imaging a droplet simply placed on top of the curved surface, but as long as the surface is hydrophobic and the droplet is small enough to be considered weightless (Extrand and Moon 2008; Guilizzoni 2011; Viswanadam and Chase 2012; Lu *et al.* 2016).

Most recently, a new method to measure droplet CA on a hydrophilic (YLCA $< 90^{\circ}$) fiber has been proposed (Schellbach *et al.* 2016). For this method, a droplet is deposited on two horizontal parallel fibers, and the CA of the fibers is obtained from the shape of the liquid column formed between the hydrophilic fibers (the droplet should be small so that it does not hang below the fibers). As will be discussed later, the method of (Schellbach *et al.* 2016) is used in the current study for comparison whenever possible.

The underlying hypothesis for the fiber CA measurement method proposed in this study is that the fiber YLCA can directly be measured if the droplet is imaged from the longitudinal view, as opposed to the commonly-used transverse view (side view) as can be seen in Figure 3.1. This requires the droplet to be in the clamshell (hanging) conformation so that a CL is formed on the curved sides of the fiber. Working with a clamshell droplet alleviates the need for the droplet volume to be small, as the clamshell profile is promoted by the gravitational force (as opposed to being prevented like in the case of barrel-shaped droplets). The larger clamshell droplets are also easier to produce and easier to place on a fiber (Chou *et al.* 2011; Eral *et al.* 2011; Mei *et al.* 2013; Funk *et al.* 2014).

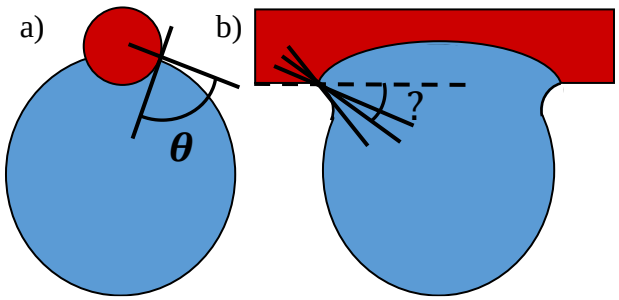

Figure 3.1: Droplet contact angle on a fiber from the longitudinal and transverse directions in (a) and (b), respectively.

In the remainder of this chapter, we first describe our YLCA measurement method in Section 3.2. We then present a few droplet–fiber combinations for which the YLCA was measured and compared with those obtained using established methods from the literature in Section 3.3. The conclusions drawn from the work are given in Section 3.4.

3.2 Measuring YLCA of a Fiber

Figure 3.2a shows our experimental setup consisting primarily of a fiber mounted on a 3-D printed holder, an Era NE-300 syringe pump (to produce liquid droplets of desired volumes), and a digital camera (Phantom Miro LAB/ LC/R series). While the proposed method can be used for any arbitrary fluid, we considered a aqueous ferrofluid (from EMG508, Ferrotech, USA) for most of our experiments to also examine the accuracy of our method when the droplet was affected by an external force larger than the gravity. The surface tension and density of the ferrofluid used in our experiments were measured to be 0.0649 N/m and 1050 kg/m^3 at 25 °C, respectively. The experiment starts by first washing the fiber with isopropyl alcohol and then allowing it to dry for a couple of hours. Using the syringe pump, a small droplet was then gently deposited on the fiber and its volume was increased gradually until a hanging clamshell droplet was obtained. Each experiment was repeated multiple times, and the results were averaged.

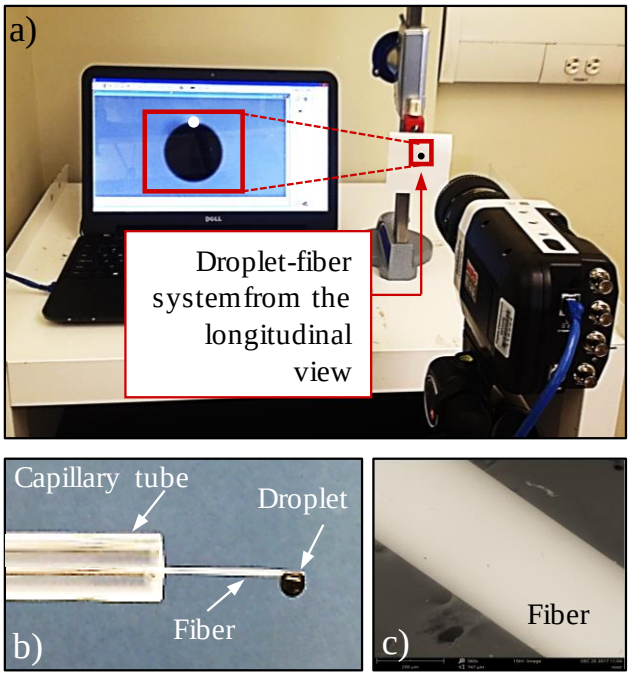

Figure 3.2: Our experimental setup is shown in (a). The droplet–fiber mounting system is shown in (b). An SEM image of the fiber's smooth surface is shown in (c).

For the fiber YLCA (intrinsic CA) measurement method proposed in this study, the droplet should be large enough to exhibit a clamshell (hanging) profile on the fiber but obviously small enough to remain on the fiber under the influence of gravity. The droplets were imaged from transvers (optional) and longitudinal (required) views. For the latter, the fiber was mounted in a cantilever-like position (one end fixed but the other end free (see Fig. 3.2b)) with the camera facing the fiber cross-section. The droplet was then placed as close to the end of the fiber as possible to image both the droplet boundaries and the fiber cross-section with the same (almost the same) magnification. Note that for the proposed YLCA measurement method to be accurate, the fiber surface should be smooth to avoid CL pinning (see the SEM image given in Fig. 3.2c).

Figures 3.3a and 3.3b show ferrofluid droplets of different volumes (from 4 to 12 μL) deposited on a hydrophilic fiber with a diameter of $d = 381$ μm (Trilene XL smooth casting nylon fishing line) from the transverse and longitudinal views, respectively (detachment volume for this droplet–fiber system is $V_d = 12.2$ μL). It can be seen that ferrofluid droplets in this volume range exhibit clamshell profiles on this particular fiber. It is interesting to note that apparent CA (measured from a droplet's macroscopic profile that excludes the skewed corners (Bormashenko 2013; Marmur *et al.* 2017; Farhan and Tafreshi 2018)) from the transverse view tends to vary with increasing droplet volume (see Fig. 3.3c) whether defined at the contact point with the solid boundary (red colored angles) or at the droplet inflection point (where droplet curvature changes sign (Rebouillat *et al.* 2002)). The latter was obtained in the current study by extracting droplet boundaries using an edge-detection algorithm in the *Mathematica* software. A 6th order polynomial $y = f(x)$ was then curve-fitted to these data, and the inflection point was obtained by setting the second derivative of the function equal to zero, i.e., $f''(x) = 0$. This provided the *x*-coordinate x_i and subsequently, the *y*-coordinate $y_i = f(x_i)$ of the inflection point. The inflection points and their

corresponding angles are shown in blue color for droplets with different volumes in Fig. 3.3c. The contact angles from the longitudinal views were also obtained in a similar manner through image process via Mathematica. An example of such calculation is shown in Figs. 3.3d and 3.3e for simulated and imaged droplets, respectively. Figures 3.3d and 3.3e each show two droplets, one with a volume of 4 μL and the other with a volume of 12 μL (note how CL moves down along the side of the fiber preserving the CA).

The CA viewed from the longitudinal direction remains the same regardless of the droplet volume. This is because with increasing the gravitational force (e.g., droplet volume), CL can freely move downward on the curved sides of the fiber (see the green dots in the magnified figures in Fig. 3.3b) allowing the air–liquid interface to maintain its original slope with the fiber. This does not happen in the transverse direction where CL can only move horizontally along the length of the fiber (normal to the direction of the body force). The results shown in Figure 3.3 indicate that droplet CA viewed from the longitudinal direction is volume-independent. Moreover, as the CL can be located on the side of the fiber (from the longitudinal view) relatively easily, and as the droplet's local profile is concave near the CL (independent of the hydrophilicity or hydrophobicity of the fiber), it is reasonable to conclude that the measured CA can represent the YLCA of the fiber. The volume-independence is a significant attribute of our YLCA measurement method, as accurate droplet volume measurement can be quite difficult when working with small droplet–fiber systems. In addition, since the proposed method does not require the fiber to be hydrophilic or hydrophobic, it can be used with liquids with an unknown surface tension.

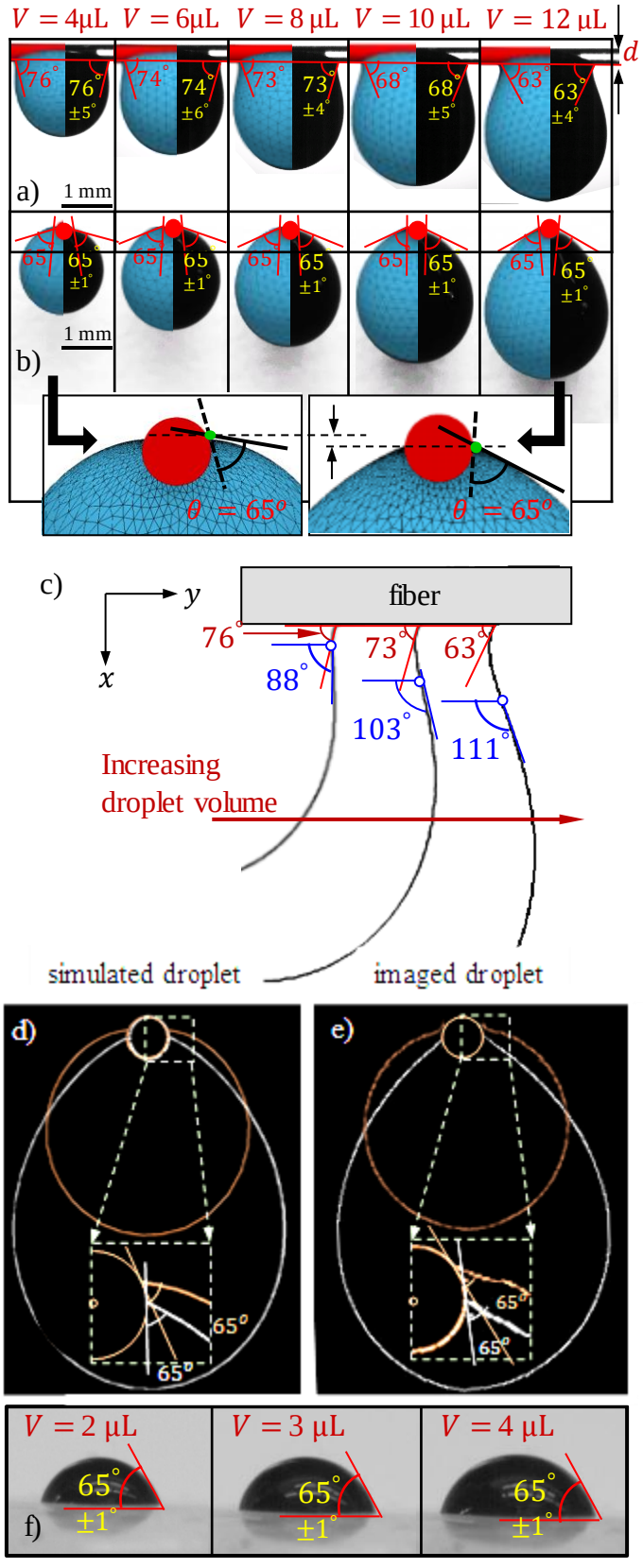

Figure 3.3: Ferrofluid droplets with different volume (**4 μL ≤ V ≤ 12 μL**) hanging from a fiber under the influence of gravity from the transverse (a) and longitudinal (b) views. The droplet profile from experiment and simulation ($\boldsymbol{\theta_{YL}}$=**65°**) are compared. Droplet profiles from the transverse view are obtained using an edge-detection algorithm in *Mathematica* software and overlaid on top of one another in (c). Transverse CA is defined in two different ways, and both are found to vary with droplet volume. Examples of droplet profiles used for measuring fiber's YLCA from the longitudinal view are shown in (d) and (e) for droplets with two different volumes 4 and 12 μL. The profiles shown in (d) are from simulated droplets, and are reported here for comparison only. Fiber's YLCA is also measured using the sessile-drop method on a flat sheet made of the same material of the fiber in (f).

It is important to emphasize here that microscopic measurement of droplet CA near the fiber surface from the transverse view will most probably show a CA close to the YLCA of the surface. However, such measurements are not easy to conduct when working with small droplets on small fibers. The problem becomes even harder when the fiber is hydrophilic as the droplet local curvature changes asymptotically near the CL (McHale *et al.* 1997; McHale *et al.* 1999; 24–25, Bormashenko 2013; Marmur *et al.* 2017; Farhan and Tafreshi 2018).

The YLCA for the fiber used in the experiments shown in Fig. 3.3 was measured using two different methods, and it was found to be $\theta_{\mathrm{YL}} \approx 65^{\circ}$. For the first method, the fiber was placed in a capillary tube with a known YLCA, and the rise of a known liquid in the gap between the tube and the fiber was imaged and used to obtain the YLCA of the fiber (Farhan and Tafreshi 2018; Aziz *et al.* 2018). For the second method, the droplet profile from experiment was compared to that obtained from a series of validated numerical simulations conducted for the same droplet–fiber system but with different fiber YLCAs as input. The YLCA for which the simulated droplet profile matched the one from experiment was taken as the YLCA of the fiber (see (Amrei *et al.* 2016; Farhan and Tafreshi 2018) for more detailed information). The numerical simulations reported in Figure 3.3 were conducted using the Surface Evolver (SE) finite element code (Brakke 1992). SE simulations start by placing a droplet with an arbitrary shape on the fiber. SE then, evolves the droplet shape to reach a 3-D profile that corresponds to the minimum energy of the fiber–droplet system in the presence of an external body force acting on the droplet (Marmur *et al.* 2017; Venkateshan and Tafreshi 2018).

For further validation, we melted some of the fibers that were used for the experiment in an oven and flattened the surface of the resulting sheet using a heavy press. Figure 3.3f shows ferrofluid droplets with different volumes on the resulting surface (droplets are small enough to provide the YLCA of the surface). As can be seen, a YLCA of $\theta_{\mathrm{YL}} \approx 65^{\circ}$ is obtained for the surface in agreement with the contact angle

observed from the longitudinal direction on the fiber in Figure 3.3b. Note that the above sessile-drop method can only be used for fibers that can easily be melted and made into a flat sheet with no compositional degradation. For instance, working with carbon fibers, metallic fibers, glass fibers, or fibers from any material that loses its composition when melted makes the sessile-drop method impractical. In addition, there are many fibers with a coating on their surface [Yousefi *et al.* 2018]. Some coatings are added to help with fiber spinning process (e.g., a spin-finish) and others are added to enhance the performance of the fibers for their intended applications (e.g., to enhance the wettability of the fibers for fluid absorption applications). Moreover, many fibers are made of more than one polymer. For instance, some bi-component fibers are made of a stronger polymer as the core, and a more functional polymer as the sheath. The sessile-drop method is obviously not suitable for measuring the YLCA of such fibers.

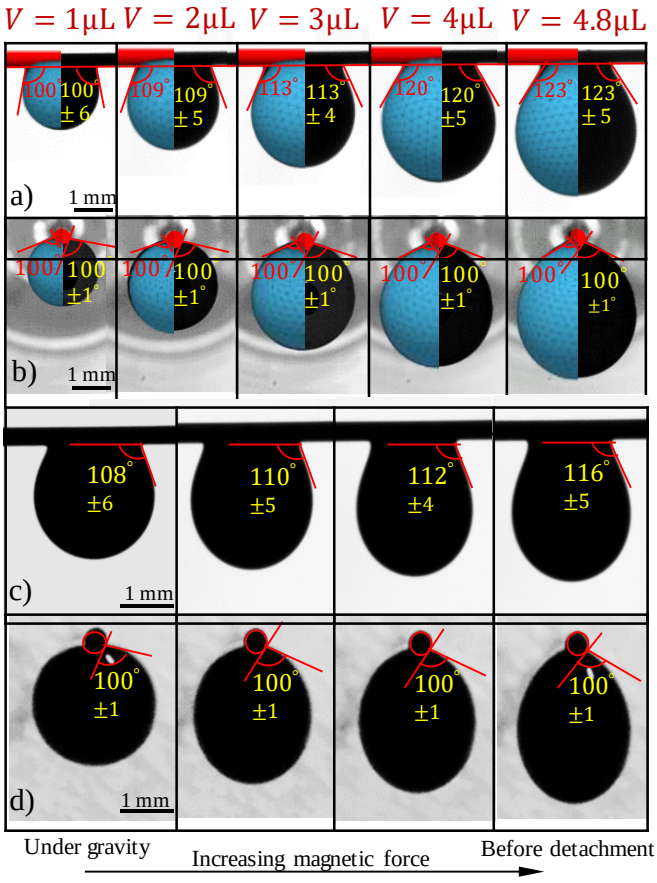

Figure 3.4: Ferrofluid droplets with different volume ($1\ \mu L \leq V \leq 4.8\ \mu L$) hanging from a hydrophobic needle fiber under the influence of gravity from the transverse (a) and longitudinal (b) views. The needle has a diameter of $d = 262\mu m$, an YLCA $\theta_{YL} \approx 100^{\circ}$, and a ferrofluid detachment volume of $V_d = 5\ \mu L$. The ferrofluid droplet with a volume of 2 µL is shown in (c) and (d) when subjected to a downward magnetic force. The magnetic force increases from left to right. The figure to the right is the final equilibrium state before droplet detaches from the fiber.

To examine the accuracy of the proposed method when the fiber is hydrophobic, we repeated the above experiments using a hydrophobic needle with a diameter of $d = 262$ μm (from MHC Medical Products, LLC, USA). Figures 3.4a and 3.4b show the droplet and its CAs from the transverse and longitudinal views, respectively. It can again be seen that transverse CA varies with droplet volume while the longitudinal CA remains the same at $\theta \approx 100^{\circ}$ (which was also confirmed independently using the above-mentioned YLCA measurement methods). Note in Figure 3.4 that, droplet profile from experiment matches that obtained from numerical simulation of droplets on a fiber with an YLCA $\theta_{YL} = 100^{\circ}$.

To investigate how the transverse and longitudinal CAs respond to an external body force exerted on the droplet, we deposited a ferrofluid droplet with a volume of 2 μL on the fiber shown in Figs. 3.4a and 3.4b but used a permanent magnet to pull on the droplet. The magnetic force was then increased continuously by bringing the magnet closer to the droplet using an accurate height gauge. As can be seen in Figs. 3.4c and 3.4d, the transverse CA changes continuously while the longitudinal CA remains the same at $\theta \approx 100^{\circ}$regardless of the strength of the magnetic force (from gravity-only, on the left, to the final equilibrium state before detachment under the influence of gravity and magnetic force, on the right). The evidence shown in Figs. 3.3 and 3.4 serves to prove that the proposed YLCA measurement method is independent of droplet volume and/or the magnitude of the external force acting on the droplet (the basic requirements for measuring YLCA on a flat surface).

3.3 Comparison with Existing Methods

As mentioned earlier in the Introduction, a method to measure droplet CA on hydrophilic (YLCA $< 90^{\circ}$) fibers was recently reported in (Schellbach *et al.* 2016). In this method, a droplet was deposited on two horizontal parallel fibers, and the CA of the fibers was obtained from the shape of the liquid column formed between these fibers using the following expression,

$$\theta_{YL} = 90 - 2\ \tan^{-1}\left(\frac{2h}{b}\right) \tag{3.1}$$

In this equation, h and b are the height and width of the spherical meniscus formed between the fibers, respectively. We used this method to obtain the YLCA of our hydrophilic fiber (the one reported in Fig. 3.3) for comparison. We considered two identical fibers. We fixed one of the fibers horizontally but made the other one movable in the lateral direction in the same horizontal plane (to vary the fiber–fiber distance b) using the motors of two Era NE-300 syringe pumps. The experiment started by placing a ferrofluid droplet on the fibers while the fibers were close to each other. We then increased the distance between the fibers until the droplet formed a bridge between the fibers (see Fig. 3.5a). Using this method, we obtained an average YLCA of $\theta_{YL} = 61^{\circ} \pm 3^{\circ}$ which is within 6% of the angle obtained using our proposed method, i.e., $\theta_{YL} = 65^{\circ}$. We also used the measured YLCA in a simulation devised to mimic the above experiment (see Figure 3.5b). As can be seen in these figures, there is good relative agreement between droplet length obtained from experiment and from simulation, indicating that the YLCA measured experimentally was accurate.

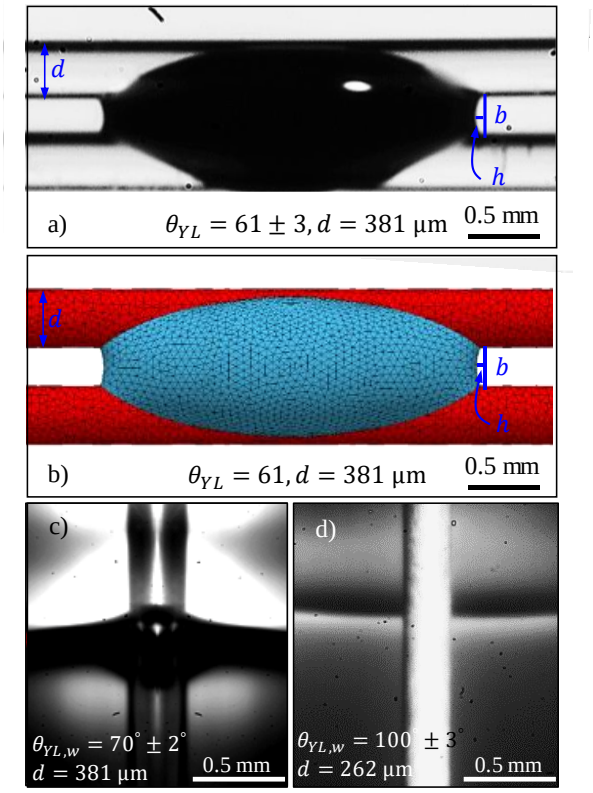

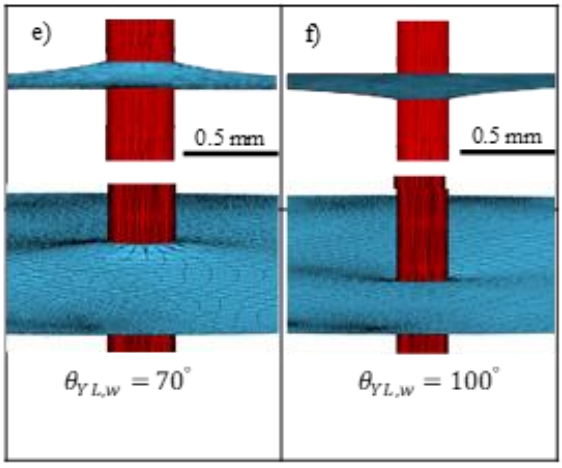

Figure 3.5: Ferrofluid droplet forming a bridge between two fishing lines (with the same properties as mentioned in Figure 3.2) is shown in (a) along with its numerical counterpart in (b). An YLCA of about 61 degrees was obtained from the image according to the method developed in (Schellbach *et al.* 2016). YLCAs are obtained for the hydrophilic fiber of Figure 3.3 and the hydrophobic needle of Figure 3.4 using DI water in (c) and (d), respectively. Computational counterparts of the experiment reported in (c) and (d) are given in (e) and (f), respectively.

We also repeated the YLCA measurements of Figs. 3.3 and 3.4 by vertically submerging one end of the fiber in a large body of deionized (DI) water (DI water for its cost-effectiveness compared to ferrofluid), as shown in Figures 13c and 13d. The meniscus rise near the surface of the fibers was then compared to the results from numerical simulation (Figures 3.5e and 3.5f) to confirm the accuracy of the measured YLCAs of $\theta_{YL,w} = 70^{\circ} \pm 2^{\circ}$ and $100^{\circ} \pm 3^{\circ}$ with DI water for the fiber used in Fig. 3.3 and the needle used in Fig. 3.4, respectively. We then used Eq. 3.2 to convert the YLCAs obtain with DI water to those for ferrofluid (knowing the surface tension of DI water σ_w and that of the ferrofluid σ) (Good and Girifalco 1960; Sullivan 1981).

$$\cos\theta_{YL} = -1 + \left(\frac{\sigma_w}{\sigma}\right)^{1/2} (\cos\theta_{YL,w} + 1) \tag{3.2}$$

The resulting YLCAs for ferrofluid were $\theta_{YL} = 65^{\circ} \pm 2^{\circ}$ and $\theta_{YL} = 97^{\circ} \pm 3^{\circ}$ for the fiber of Fig. 3.3 and the needle of Fig. 3.4, respectively (less than 10% mismatch with the method proposed here). Note that

the method used in Fig. 3.5c and 3.5d also suffers from the aforementioned problem of asymptotic curvature change near the contact line when the surface is very hydrophilic (making image processing difficult) (McHale *et al.* 1997; McHale *et al.* 1999; Bormashenko 2013; Marmur *et al.* 2017; Farhan and Tafreshi 2018).

We also examined the accuracy of the proposed YLCA measurement method when used for fibers smaller or larger, or with fluids having different properties. Figure 3.6a shows a ferrofluid droplet on a Polypropylene fiber (from FiberVision) with a diameter of $d = 50$ μm exhibiting an intrinsic CA of $\theta_{YL} \approx 83^{\circ}$ (no attempt was made to control the volume of the droplet, as the proposed method is volume-independent). To check the accuracy of this measurement, we simulated the shape of a ferrofluid droplet with a volume $V = 2$ μL on a fiber with the same diameter having an YLCA of $\theta_{YL} = 83^{\circ}$, and compared the resulting droplet profile with that obtained experimentally. As can be seen in Fig. 3.6b, there is good agreement between the experimental and computational profiles (only the transvers view is shown for the sake of brevity), supporting the applicability of the proposed method to YLCA measurement for fibers as small as 50 μm in diameter (and perhaps smaller). Figure 3.6c shows a silicone oil droplet on a fiber with a diameter of 1.28 mm showing an YLCA of $\theta_{YL} \approx 20^{\circ}$. Numerical simulation results obtained for the same droplet–fiber system (and an YLCA of $\theta_{YL} = 20^{\circ}$) are also shown in Fig. 3.6d, to further confirm the accuracy the proposed method.

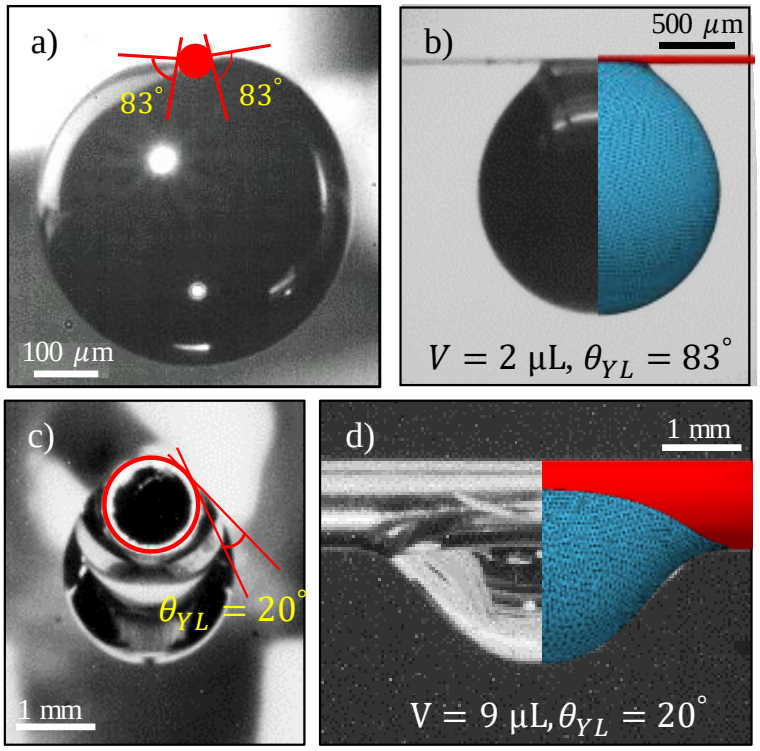

Figure 3.6: Longitudinal view of a ferrofluid droplet with an arbitrary volume on a Polypropylene fiber with a diameter of $d = 50$ μm is shown in (a) under the influence of gravity. An intrinsic CA of about 83 degrees was read from the image. Droplet profile from experiment matches that from a simulation with an YLCA of 83 degrees in (b) validating the YLCA read from (a). An YLCA of about 20 degrees can be seen from the longitudinal view of a silicone oil droplet with surface tension $\sigma_o = 0.02$ N/m on a fiber with a diameter of $d = 1.28$ mm as shown in (c). Droplet profile from experiment matches that from a simulation with an YLCA of 20 degrees in (d) validating the YLCA read from (c).

Similar to other YLCA measurement methods (e.g., Wilhelmy force method or the infection-angle method), the underlying assumption of the proposed method is the absence of CL pinning (i.e., where no significant advancing or receding CAs are expected) (Bormashenko *et al.* 2008; Bormashenko 2013). To demonstrate this, an experiment was conducted for the fiber discussed in Fig. 3.3. We deposited a ferrofluid droplet with a volume of $V = 4$ μL on the fiber, and applied downward and upward magnetic forces to the droplet (shown with dark blue arrows in Figure 3.7). As can be seen in Figs. 3.7a–3.7c and the magnified image shown in Figure 3.7d, CL moves up or down in response to the body force applied

to the droplet. This allows the droplet to maintain an angle with the fiber equal to the YLCA of the fluid–solid system, regardless of the "weight" or size of the droplet.

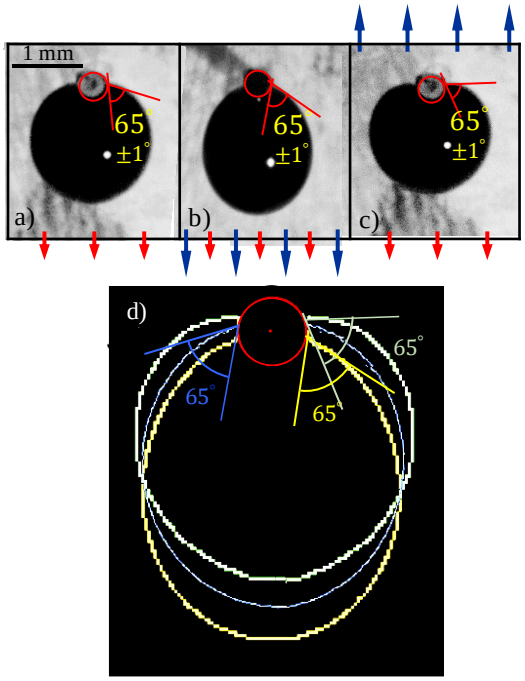

Figure 3.7: Contact angle measurement for a ferrofluid droplet with a volume of $V = 4$ µL on a nylon fiber with a diameter of $d = 381$ µm in the presence gravity (a), presence of gravity and a downward magnetic force (b), and presence of gravity and an upward magnetic force (c). The red and blue arrows show the direction of the gravitational and magnetic forces, respectively. Droplet edge obtained via image processing is shown in (d) for the three cases shown in (a) to (c).

As a final note, it is important to emphasize that typical textile fibers do not always have a perfectly circular cross-section. This is also often accompanied by some degrees of waviness along the length of the fiber (e.g., fiber crimp). The non-circularity of the cross-section or the waviness of the fiber may make it harder (depending on severity of the imperfections) to measure the droplet contact angle from the longitudinal direction.

3.4 Conclusions

A new method to measure the YLCA of a fiber (i.e., the intrinsic CA of the material from which the fiber was made) is developed in this study. Experimental and computational results were produced to show that the CA measured from the longitudinal view for a droplet in the clamshell conformation on a fiber represents the YLCA of the fiber. It was also shown that the proposed measurement method is independent of the volume of the droplet used for the experiment, or the magnitude of the external body force acting on the droplet. The droplet-volume-independence is an important attribute of the proposed method, which is in contrast to the commonly-used inflection-angle method. In addition, the proposed method can be used with both wetting and non-wetting fibers, which is also in contrast to many previous methods. Our experimental results were compared with data from numerical simulation or alternative experimental methods and good agreement was observed.

Chapter 4. Using Magnetic Field to Measuring Detachment Force between a Nonmagnetic Droplet and Fibers

4.1 Introduction

Quantifying the force required to detach a droplet from a fiber is important as it serves as a starting point in design and development of fibrous materials for applications like droplet–air or droplet–liquid separation [Contal *et al.* 2004; Kampa *et al.* 2014; Patel and Chase 2014; Yu *et al.* 2016; Wei 2018; Wei *et al.* 2019], water management in fuel cells [Gurau *et al.* 2006; Gauthier *et al.* 2012; Chen *et al.* 2013; Kakaee *et al.* 2018], fog harvesting [Garrod *et al.* 2007; Xu *et al.* 2016; Seo *et al.* 2016; Weyer *et al.* 2017; Shi *et al.* 2018], sensing [Yarin *et al.* 2002; De Ruiter *et al.* 2012], microfluidic [Gilet *et al.* 2009; Gilet *et al.* 2010], or textiles [Michielsen and Lee 2007; Sun *et al.* 2018] to name a few. Understanding droplet–fiber interfacial forces also helps improve our understanding of the nature and how it inspires biomimetic designs [Zheng *et al.* 2010; Bai *et al.* 2010].

In the context of droplet–fiber(s) interactions, there are currently three experimental techniques reported in the literature for measuring the force required to detach a droplet from a fiber: detachment driven by a high-speed airflow [Sahu *et al.* 2013; Fang *et al.* 2015; Davoudi *et al.* 2016], detachment via an external mechanical object like the cantilever tip of an atomic force microscope (AFM) [Mullins *et al.* 2007; Mead-Hunter *et al.* 2012; Hotz *et al.* 2015], and detachment via a magnetic force [Amrei *et al.* 2016; Aziz *et al.* 2018; Farhan and Tafreshi 2018]. The problem with using air as the driving mechanism for droplet detachment is that the resulting forces will depend on the specific design of the chamber used for the experiment, i.e., the local laminar or turbulent airflow pattern around the deformed droplet. For the second method, the concern is that using an external object to detach a droplet from a fiber changes the original

problem of detaching a pendent droplet to a capillary bridge problem, which may further complicate the experiment (requiring additional equipment) and the interpretation of the resulting data. The use of a magnetic field for droplet detachment and force measurement (a non-contact approach) can alleviate some of the abovementioned problems, but it can only be considered for magnetic fluids (e.g., a ferrofluid), which obviously is a major limitation for the method from an application viewpoint.

Although never used for droplet detachment from a fiber, it is important here to also mention about the use of a centrifugal force in measuring the force of adhesion between a droplet and a surface in a centrifugal adhesion balance device reported in the literature [Tadmor *et al.* 2017; Tadmor *et al.* 2009].

In the current study, we have developed a novel experimental approach that allows one to use a magnetic force for droplet detachment even when the droplet is nonmagnetic (e.g., a water or an oil droplet). This is done by adding a small amount of ferrofluid (referred to here as the secondary fluid) to the original nonmagnetic droplet (referred to here as the primary fluid) to create a compound droplet. The secondary ferrofluid can then be used to apply a body force to the resulting compound droplet and thereby detach it from the fiber(s). As will be discussed later in this chapter, the secondary fluid may reside inside the primary droplet in the form of a nested droplet [Neeson *et al.* 2012; Guzowski *et al.* 2012] or wrap around it in the form of a cloak [Khalil *et al.* 2014; Sett *et al.* 2017; Bansal and Sen *et al.* 2017; Rigoni *et al.* 2018]. The detachment force measured for the compound droplet can then be post-processed to obtain the force of detachment for the original (primary) droplet from the fiber.

The remainder of this chapter is organized as follows. Section 4.2, briefly describes our experimental setup and the materials used for the experiments. Section 4.3, presents our work on measuring the detachment force for when the primary droplet was made of a non-polar fluid (e.g., silicone oil), and an aqueous

ferrofluid was used as the secondary fluid. Section 4.4 on the other hand, presents the condition where the primary fluid was polar (e.g., water) and an oil-based ferrofluid was used to cloak and detach the primary droplet. Section 4.5 shows the application of the force measurement method developed in this study to more complicated scenarios of droplet detachment from intersecting fibers. Section 4.6 presents an analysis on the use of gravity as an alternative mechanism for droplet detachment from a fiber. The conclusions drawn from our study are given in Section 4.7.

4.2 Experimental Setup and Materials

Measuring detachment force using a magnet was first reported in Ref. [Amrei *et al.* 2016] for ferrofluid droplets on single or crossing fibers but it was also used later for studying droplet mobility on, or penetration through, hydrophobic fibrous surfaces [Jamali *et al. Appl. Surf. Sci*. 2018; Jamali *et al. Langmuir* 2018; Jamali *et al.* 2019]. The experimental approach of Ref. [Amrei *et al.* 2016] is modified here to measure the force of detachment for nonmagnetic droplets. Figure 4.1 shows our setup which consists of a fiber (Trilene XL smooth casting fishing line) mounted on a 3-D printed holder and a Mettler Toledo XSE105 weight measurement scale on which the holder is placed. An Era NE-300 syringe pump is used to produce droplets with desired volumes. The abovementioned modification is based on creating a compound droplet where a suspended ferrofluid droplet is gently injected inside the nonmagnetic droplet while it is hanging from the fibers (the ferrofluid should be immiscible with the nonmagnetic fluid).

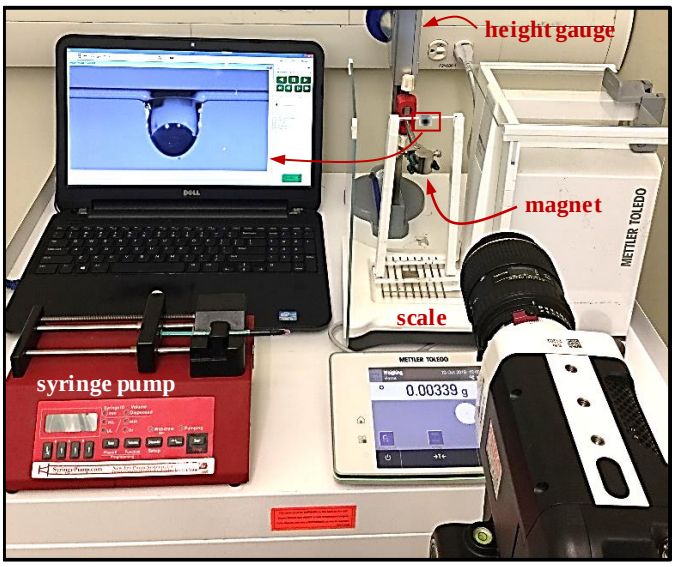

Figure 4.1: The experimental setup designed for the study.

For the experiments, we used silicone oil (ALDRICH Chemistry-USA, viscosity of 96 cP) as the nonmagnetic primary fluid and a water-based ferrofluid (EMG 508, Ferrotech, USA, viscosity of 5 cP) as the magnetic (secondary) fluid. However, for the experiments with an aqueous nonmagnetic primary fluid (e.g., water), we used a kerosene oil-based ferrofluid like EMG 900 (Ferrotech, USA, viscosity of 60 cP). The scale was zeroed after an equilibrium state was observed for the compound droplet, and the detachment process was recorded using a high-speed camera (Phantom Miro Lab 340). A nickel-plated axially-magnetized permanent magnet (mounted on a height gauge) with a diameter of 1.5 cm and a height of 3 cm (K&J Magnetics) was used to apply an external force to the droplet. Table 1 shows the surface tension (measured using the pendant drop method) and density (from manufacturer) values for the fluids used in our experiment.

Table 4.1: Fluid properties at 25 C°.

Fluid	**Surface tension**	**Density**
Silicone oil	σ_{so} = 0.02 N/m	ρ_{so} = 960 kg/m^3
Water-based ferrofluid	σ_{wf} = 0.0649 N/m	ρ_{wf} = 1050 kg/m^3
Oil-based ferrofluid	σ_{of} = 0.018 N/m	ρ_{of} = 1300 kg/m^3
water	σ_{w} = 0.072 N/m	ρ_{w} = 1000 kg/m^3

4.3 Droplet Detachment using a Nesting Ferrofluid Droplet

To create a compound droplet with a non-polar primary fluid (e.g., silicone oil) we use an aqueous ferrofluid as the magnetic (secondary) fluid. To do so, we inject a small amount of ferrofluid inside the oil droplet while it is hanging from the fiber (see Figure A1 in Appendix A). The volume of the ferrofluid droplet should be large enough to create sufficient magnetic force for the detachment but small enough to avoid contact with the fiber (dependent on the fluid densities and surface tensions as well as the fiber diameter and wettability). Figure 4.2 shows silicone oil droplets with volumes of V_{so} =2 and 3 μL hanging from a fiber with a diameter of $d = 381$ μm. Ferrofluids with different volumes are injected into the oil droplet from below using a syringe (U-100 insulin syringe, MHC Medical Products, LLC, USA). It can be seen that, ferrofluid droplets that are too small or too large are not suitable for the experiment as they may come into contact with the fiber (see Figures 4.2b, 4.2f, and 4.2h). The range of ferrofluid droplets suitable for the experiment depends on the size of the primary droplet, as shown in Figure 4.2 with a red frame (about $0.3 \leq V_{wf} \leq 1.5$ μL for $V_{so} = 2$ μL and about $0.5 \leq V_{wf} \leq 2.5$ μL for $V_{so} = 3$ μL).

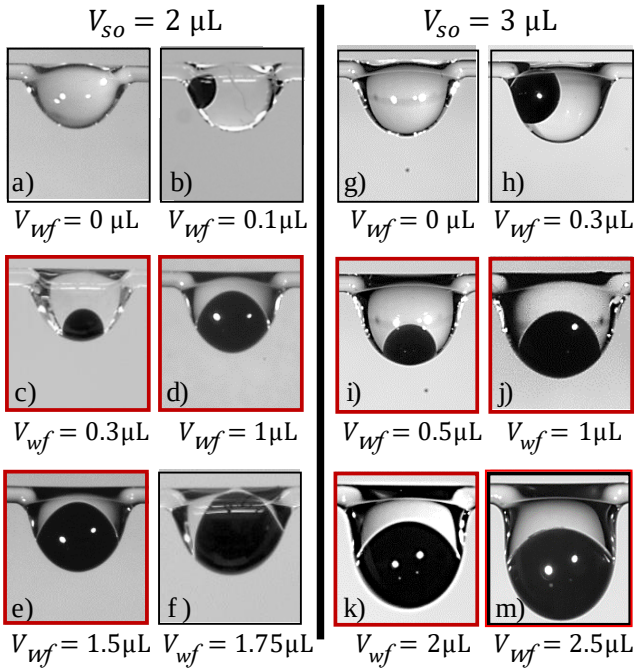

Figure 4.2: A silicone oil droplet with a volume of $V_{so} = 2$ µL on a fiber with a diameter of $d = 381$ µm is shown in (a). Compound droplets with nested ferrofluid droplets having different volumes V_{wf} are shown in (b) through (f). Similar experiment conducted for a larger silicone oil droplet with a volume $V_{so} = 3$ µL is shown in (g) through (m).

Once a suitable compound droplet is produced, the detachment experiment can start by moving the magnet toward the droplet–fiber system. As the magnet travels toward the droplet, it pulls the ferrofluid droplet downward leading to the deformation, and eventually, detachment of the compound droplet as can be seen in Figure 4.3a. Moving from Image 1 to Image 3 in this figure, the magnetic force increases from zero (only gravity acting on the droplet i.e., 38 µN) to about 11 µN (resulting in a total force of about 49 µN). The final equilibrium state of the compound droplet is shown with a red frame in Figure 4.3a. The droplet will undergo a spontaneous detachment (time-dependent) process under a constant body force of about 49 µN. At the onset of detachment (Image 3), the scale reading reaches a peak value that is taken here as the droplet detachment force. The detachment force f_{so} of the silicone oil droplet is calculated as

$$f_{so} = \mathrm{g}\left(m_{ex} + \rho_{so} V_{so} + \rho_{wf} V_{wf}\right) \tag{4.1}$$

where g is the gravitational acceleration and m_{ex} is the maximum mass value recorded by the scale at the moment of detachment. In this equation, ρ and V represent density and volume, and subscripts "so" and "wf" denote silicone oil and water-based ferrofluid, respectively.

Figure 4.3b shows the recorded body force on the fiber during one of the experiments (the scale was zeroed after both droplets were placed on the fiber; Image 1 in Figure 4.3a). As expected, the force increases as the magnet moves closer to the droplet (points 1 through 3). To detect the onset of detachment accurately, the speed by which the magnet was moved toward the droplet was decreased after point 2. Spontaneous detachment started at point 3 and continued for about 3 seconds until point 6 with the magnet held in place. It can be seen that the force measured by the scale did not vary much after the start of the spontaneous detachment process even though the center of mass of the elongated droplet moved closer to the magnet and so the droplet experienced a stronger magnetic force. This is because during the spontaneous detachment, the droplet was not in mechanical equilibrium and the additional magnetic force was spent on elongating the droplet and on accelerating it toward the magnet rather than pulling on the fiber more strongly). After droplet detachment, the scale recorded a negative force (point 7) which corresponds to the weight of the detached droplet. Note that the force applying on the silicone oil droplet is not uniform (i.e. the lower part of the oil droplet that is in contact with the ferrofluid droplet has more force comparing with the one far away from the ferrofluid droplet). However, from the force balance point view, the resulting force affecting on the fiber is the one we care about and that force the scale can predict and tell how much force were applying on the whole silicone oil droplet at the detachment moment.

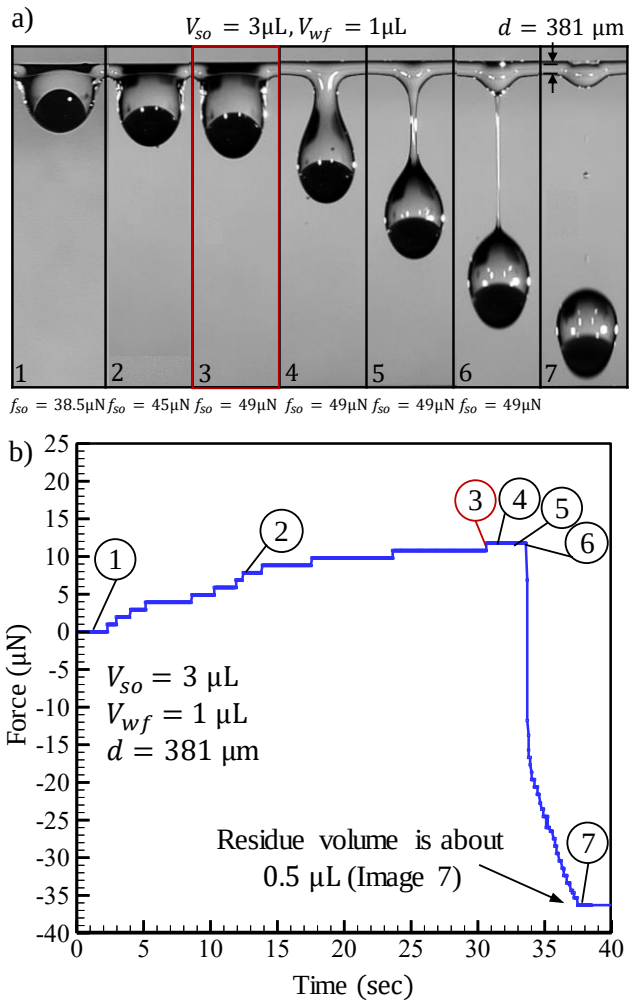

Figure 4.3: High-speed images showing detachment of a silicone oil droplet compounded with a nesting aqueous ferrofluid droplet are shown in (a). The external body force exerted on the fiber during one of our droplet detachment experiments is given in (b) as a function of time. The volume of the liquid residue left on the fiber after detachment V_r (see Image 7) is calculated using the largest recorded negative force f_r as $V_r = \frac{g(\rho_{so} V_{so} + \rho_{wf} V_{wf}) - f_r}{g\,\rho_{so}}$.

Figure 4.4a shows the force required to detach a silicone oil droplet with a volume of $V_{so} = 3$ µL from a fiber using nested ferrofluid droplets of different volumes V_{wf}. As can be seen in this figure, a detachment force of about $f_{so} \cong 50$ µN has been obtained for the silicone oil droplet ($V_{so} = 3$ µL) independent of the volume of the ferrofluid droplet used for the experiment. Note that, with increasing the volume of the ferrofluid, the compound droplet will become heavier and a smaller magnetic force is required to detach it from the fiber. Figure 4.4b shows similar results but for silicone oil droplets with two different volumes of $V_{so} = 3$ and 5 µL placed on a fiber with a larger diameter of 532 µm and a different YLCA of $\theta = 18°$.

It again can be seen that detachment force is independent of the volume of the nested ferrofluid used for the experiment.

To examine the accuracy of our experimental results, and to obtain additional insight into the interplay between the forces acting on the oil droplet, we also conducted a series of numerical simulations using the Surface Evolver (SE) finite element code [Brakke 1992]. Once the fiber–droplet system was properly defined for SE, the code was able to minimize the total energy of the system toward an equilibrium shape for the droplet under the influence of the applied body force [Amrei *et al.* 2016; Aziz *et al.* 2018; Farhan and Tafreshi 2018; McHale and Newton 2002; Moghadam *et al. Colloids Surf. A* 2018]. The simulations started by placing a body of silicone oil with a volume V_{so}, a density of ρ_{so}, and a surface tension of σ_{so} on the fiber and allowing it to evolve to reach an equilibrium shape. An external body force was then applied to the droplet in a direction normal to the fiber, and the force magnitude was increased incrementally until no equilibrium shape could be found for the droplet. The maximum force at which an equilibrium state was obtained for the hanging oil droplet was considered as the droplet detachment force in our study (see Refs. [Amrei *et al.* 2016; Aziz *et al.* 2018; Farhan and Tafreshi 2018; Jamali *et al. Appl. Surf. Sci*. 2018; Jamali *et al. Langmuir* 2018; Ojaghlou *et al.* 2018] for more details).

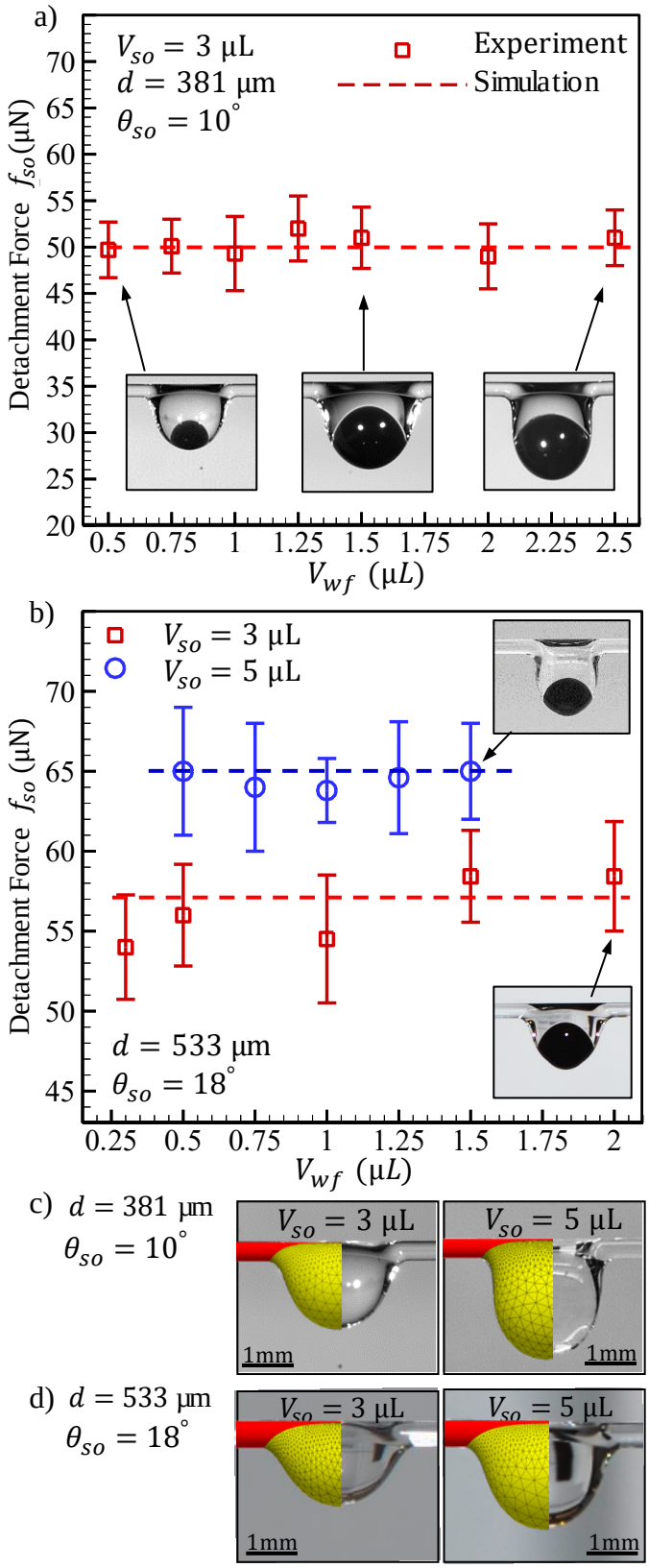

Figure 4.4: Experimentally measured detachment force for a silicone oil droplet compounded with ferrofluid droplets of different volumes is given in (a). Numerical simulation results (dashed line) obtained for pure silicone oil is also given for comparison. The experiment–simulation comparison of (a) is repeated for a fiber with a different diameter and a different YLCA in (b) for silicone oil droplets with two different volumes. Our image-based YLCA measurement method applied to the droplet–fiber systems considered in this figure is shown in (c) and (d).

Our numerical simulation results (obtained for detachment of a silicone oil droplet with a volume of V_{so}) are shown in Figures 4.4a and 4.4b using dashed lines, and it can be seen that they are in good agreement with the experimental data. Note that the YLCA of the fiber with the silicone oil θ_{so}, required for the simulations, was experimentally obtained using an image-based method (see Figures 4.4c and 4.4d) described previously in Refs. [Amrei *et al.* 2016; Aziz *et al.* 2018; Farhan and Tafreshi 2018; Farhan *et al.* 2019].

4.4 Droplet Detachment using a Cloaking Ferrofluid Droplet

When the primary droplet is made from a polar fluid (e.g., water), one can use an oil-based ferrofluid for the detachment experiment. With the surface tension of most oils less than that of most polar fluids, it is likely that the ferrofluid will cloak the primary droplet rather than a nesting inside it.[36–43]

Figure 4.5 shows the detachment process for a compound droplet comprised of a water droplet with a volume of 4 μL cloaked by 0.3 μL of oil-based ferrofluid. The experiment started by first placing a water droplet on the fiber (Image 1) and zeroing the scale. The ferrofluid was then brought into contact with the water droplet using a small needle (from below without letting ferrofluid touch the fiber, Image 2) and was allowed to cloak the water droplet (Images 3–6). After an equilibrium state was reached for the compound droplet (Image 7) (about t_1= 0.8 s in the case shown here), the increased mass m_{scale} was read from the scale (to calculate the volume of the cloaking ferrofluid $V_{of} = m_{scale}/\rho_{of}$), and the scale was zeroed again. The detachment process started by moving the magnet closer to the droplet (Images 8–9) increasing the magnetic force from zero (only gravity affecting the droplet) to about 8 N/kg (resulting in a total force of about $F_z = 18$ N/kg affecting the droplet). Images 10–12 in Figure 4.5 show the process of spontaneous (time-dependent) droplet detachment under a constant body force of about 18 N/kg.

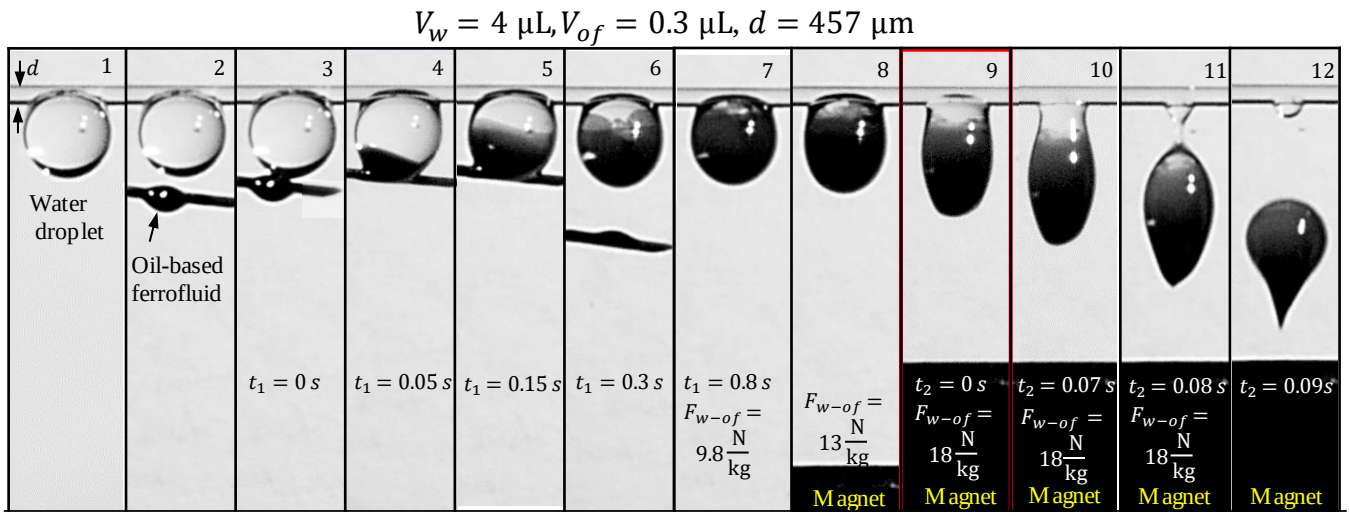

Figure 4.5: High-speed images showing detachment of a DI water droplet cloaked by an oil-based ferrofluid. Image 1 shows the water droplet under the gravity. Images 3 through 7 show the ferrofluid cloaking the water droplet in less than a second. Image 8 shows the compound droplet under the influence of gravity and a weak magnetic force. Image 9 shows the compound droplet in its final state of equilibrium before the spontaneous detachment. Images 10 through 12 show the spontaneous detachment process.

Figure 4.6 shows the force recorded by the scale during one of the experiments with a water droplet having a volume of $V_w = 8$ µL and cloaked by 0.7 µL of the oil-based ferrofluid. The force on the fiber increases with bringing the magnet closer to the droplet until the spontaneous detachment process starts (corresponding to the largest recorded force in Figure 4.6). The negative value shown by the scale after detachment corresponds to the weight of the detached droplet and can be used to obtain the weight of the residue left on the fiber (0.5 µL here). Similar to the case of nesting ferrofluid droplets (Section 4.3), the force applying on the water droplet is not uniform (i.e. the lower part of the water droplet has more force since the ferrofluid will cumulate down more with bringing the magnet closer to the compound droplet). However, from the force balance point view, the resulting force affecting on the fiber is the one we care about and that force the scale can predict and tell how much force were applying on the whole water droplet at the detachment moment.

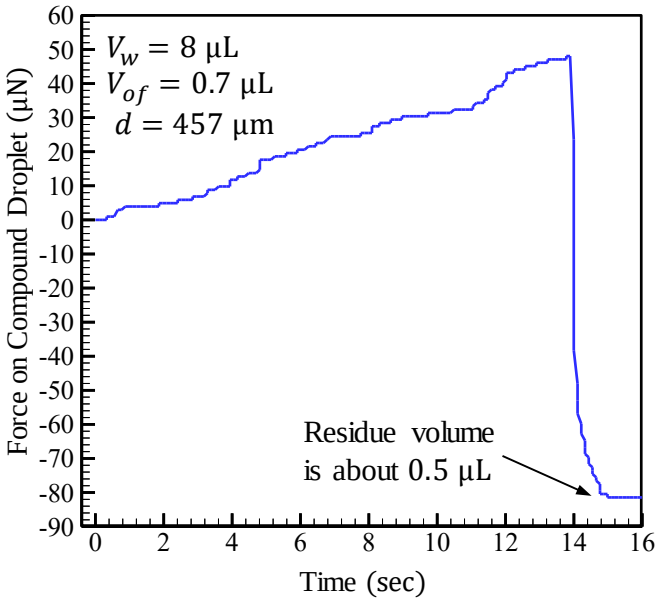

Figure 4.6: The external body force exerted on a fiber with a diameter of 457 µm during magnetic detachment of a water droplet with a volume of 8 µL cloaked by 0.7 µL of oil-based ferrofluid. The volume of the liquid residue left on the fiber after detachment V_r is calculated using the largest recorded negative force.

Similar to the case of nesting ferrofluid droplets (Section 4.3), the volume of the cloaking ferrofluid should not be too small or too large. Figures 4.7a–c show three compound droplets made with 4 µL of water but with different volumes of ferrofluid. It can be seen that the compound droplet does not detach from the fiber when the cloak is too thin (Figure 4.7a with $V_{of} = 0.1$ µL). Increasing the ferrofluid volume to $V_{of} \geq 0.3$ µL, can result in a successful droplet detachment as can be seen in Figure 4.7b. However, excessive ferrofluid volumes (e.g., $V_{of} = 1.5$ µL as shown in Figure 4.7c), can lead to ferrofluid ejection from the compound droplet before detachment takes place. This makes it hard to know the volume of the ferrofluid that was actually on the compound droplet during detachment (needed for calculating the detachment force).

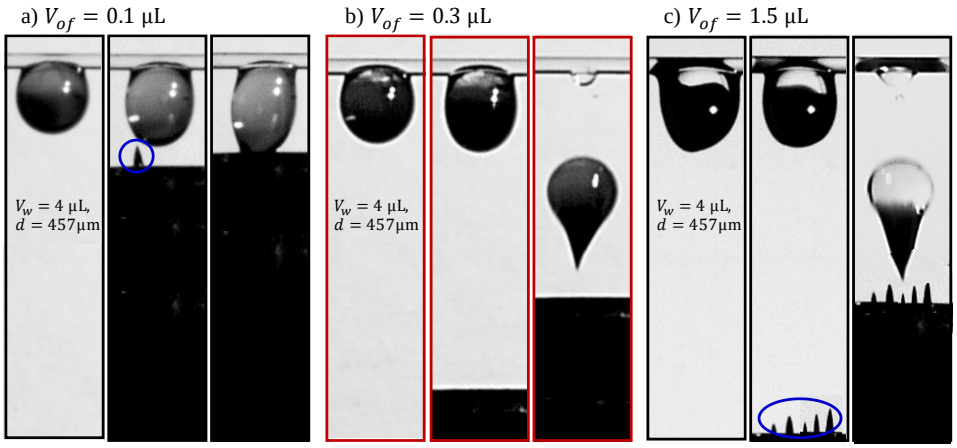

Figure 4.7: Possible scenarios of detaching a water droplet with a volume of 4 µL cloaked with different amounts of oil-based ferrofluid. (a): insufficient amount of ferrofluid, (b): right amount of ferrofluid, (c): excessive amount of ferrofluid.

Note that since the oil-based ferrofluid cloaks the water droplet, the contact angle between the fiber and the droplet changes from the YLCA of water with the material of the fiber in air θ_w to an angle closer to that in a bath of ferrofluid θ_{w-of}. Therefore, the recorded detachment force for such a compound droplet F_{w-of} should properly be scaled before it can be assigned to a water droplet. The compound droplet detachment force from experiment F_{w-of} can be written as,

$$F_{w-of} = \frac{g\,(m_{ex}+\rho_{of}\,V_{of}+\rho_w\,V_w)}{\rho_{of}\,V_{of}+\rho_w\,V_w} \tag{4.2}$$

With the compound droplet and its volume-equivalent made of water (with a volume of $V_{w,eq} = V_w + V_{of}$) having identical Bond numbers at the moment of detachment, we can write [Farhan and Tafreshi 2018],

$$F_w = \frac{\rho_{w-of}}{\rho_w}\,\frac{\sigma_w}{\sigma_{w-of}}\,\frac{1+\cos\theta_w}{1+\cos\theta_{w-of}}\,F_{w-of} \tag{4.3}$$

where F_w is the force needed to detach the volume-equivalent water droplet, and σ_w is the water surface tension. Also in this equation, $\rho_{w-of} = \frac{\rho_{of}\ V_{of} + \rho_w\ V_w}{V_w + V_{of}}$ and σ_{w-of} are "effective" density and surface tension (in air) for the compound droplet. The parameter $\cos\theta_{w-of}$ can be obtained from the Young equation $\cos\theta_{w-of} = (\sigma_{s-of} - \sigma_{s-w})/\sigma_{w-of}$ and further simplified considering $\cos\theta_{of} = (\sigma_s - \sigma_{s-of})/\sigma_{of}$ and $\cos\theta_w = (\sigma_s - \sigma_{s-w})/\sigma_w$ (subscripts, *s*, *of*, and *w* refer to solid, oil-based ferrofluid, and water, respectively), to appear as (see Figure 4.8a),

$$\cos\theta_{w-of} = \frac{\sigma_w\ \cos\theta_w - \sigma_{of}\ \cos\theta_{of}}{\sigma_{w-of}} \tag{4.4}$$

Note that we use the aforementioned image-based method (see Ref. [Amrei *et al.* 2016; Aziz *et al.* 2018; Farhan and Tafreshi 2018; Farhan *et al.* 2019]) to measure the YLCA of water θ_w and oil-based ferrofluid θ_{of} with the fiber (see Figure 4.8b). The other unknown parameter needed for scaling the detachment force obtained for a compound droplet to be used for a water droplet is an "effective" surface tension for the compound droplet σ_{w-of}. Here, we obtain this effective surface tension using a semi-empirical correlation that we developed previously to predict the force needed to detach a droplet from a fiber (Eq. 15 in Ref. [Farhan and Tafreshi 2018]), written here for σ_{w-of}, i.e.,

$$\sigma_{w-of} = \frac{F_{w-of}\ \ \sigma_{ref}}{\left(\frac{r_{\mathrm{ref}}}{r}\right)^2 \frac{\rho_{ref}}{\rho_{w-of}} \left(1+\cos\theta_{w-of}\right) \varphi \left(\frac{V_w+V_{of}}{r^3}\right)^{-\xi}} \tag{4.5}$$

where, F_{w-of} is the force obtained from the experiment with the compound droplet. All other parameters in this equation are constant ($\sigma_{ref} = 0.0649$ N/m, $r_{ref} = 190.5 \times 10^{-6}$m, $\rho_{ref} = 1050$ kg/m^3, $\varphi =$ 3,894 N/kg, and $\xi = -0.84$).

With σ_{w-of} from Eq. 4.5, the detachment force for a water droplet with a volume equal to that of the compound droplet can now be found using Eq. 4.3. Figure 4.8c shows the detachment force of a water droplet (obtained from Eq. 4.3) with a volume of $V_{w,eq}$. Simulation results for a water droplet detachment from the same fiber are also included for comparison. Excellent agreement can be seen between the detachment forces obtained from simulation and those from Eq. 4.3. Once a figure like Figure 4.8c is produced, one can obviously read the force needed to detach the original water droplet (the one with a volume of V_w) from the figure. Alternatively, one can start making the compound droplet with a water droplet slightly smaller than the desired water droplet (for instance, 25% smaller) such that the volume of the resulting compound droplet (after cloaking with ferrofluid) matches that of the water droplet in question. One should then detach the resulting compound droplet using a magnet to obtain the force of detachment F_{w-of}, and use Eqs. 4.5 and 4.3 to scale this force for the desired water droplet.

An important discussion is given in Ref. [Tadmor *et al.* 2017] to judge if the forces recorded during a droplet detachment experiment can represent the work of adhesion or they are merely the force needed to break up a droplet. Following Ref. [Tadmor *et al.* 2017], we have presented an analysis in Appendix A for some of the experiments reported in this chapter to ensure that the recorded forces are not for droplet breakup (see Appendix A).

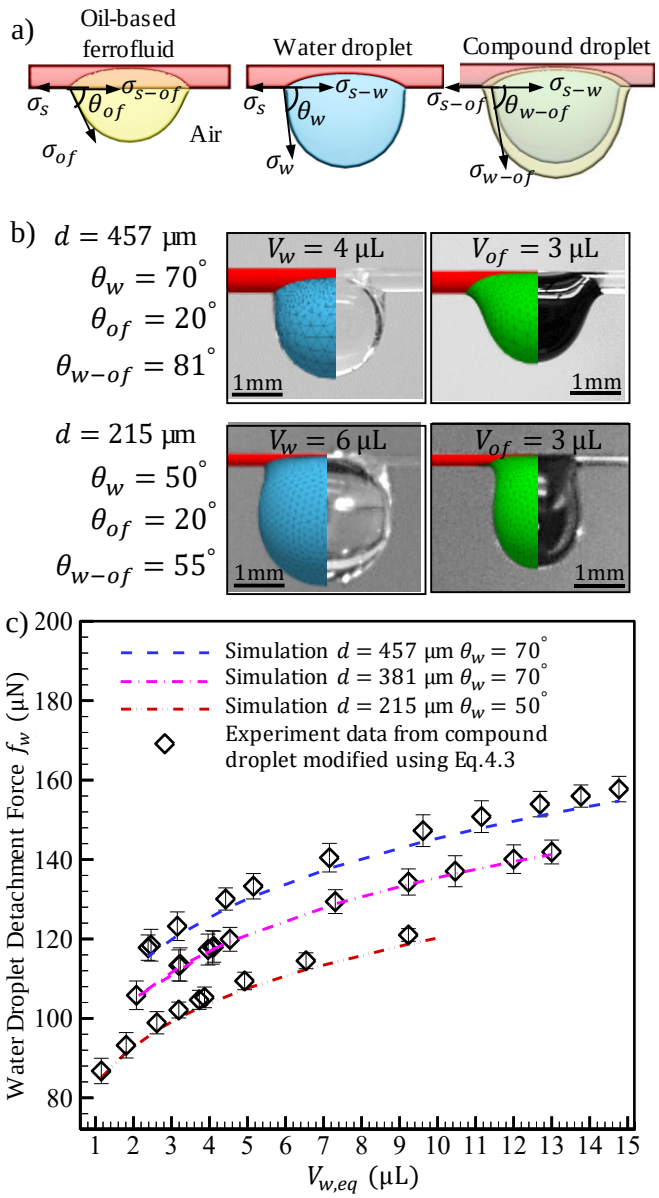

Figure 4.8: Schematic drawings show the contact angles for a pendent oil-based ferrofluid droplet (left), a pendent water droplet (middle), and a compound droplet made of the two (right) in (a). The subscript "s", "w" and "of" denote solid-surface, DI water, and oil-based ferrofluid, respectively. Our image-based YLCA measurement method applied to the droplet–fiber systems considered in this figure is shown in (b). Detachment force data are obtained for ferrofluid-cloaked water droplets using a magnetic field and scaled (Eqs. 4.3 and 4.5) to represent detachment force for pure water droplets in (c). Numerical simulation results obtained for pure water droplet are also shown for comparison.

4.5 Detaching Nonmagnetic Droplets from Crossing Fibers

In this section, we discuss detachment of nonmagnetic droplets from intersecting fibers. Figure 4.9a shows the detachment force for a silicone oil droplet with a volume of $V_{so} = 4$ μL (compounded with nesting aqueous ferrofluid droplets of different volumes) on two intersecting (orthogonal respect to one another) fibers with a diameter of $d = 381$ μm and a YLCA of about $\theta_{so} = 10^\circ$ with silicone oil. The inset on the

top shows examples of such compound droplets made with ferrofluid droplets of different volumes from two different views. The red dashed-line in Fig. 4.9a show the results of our numerical simulations conducted for the detachment of the silicone oil droplet from the fiber. A computational figure showing the silicone oil droplet with a volume of $V_{so} = 4$ µL at the final state of equilibrium (near detachment moment) on the intersecting fibers is also shown as a second inset for better illustration.

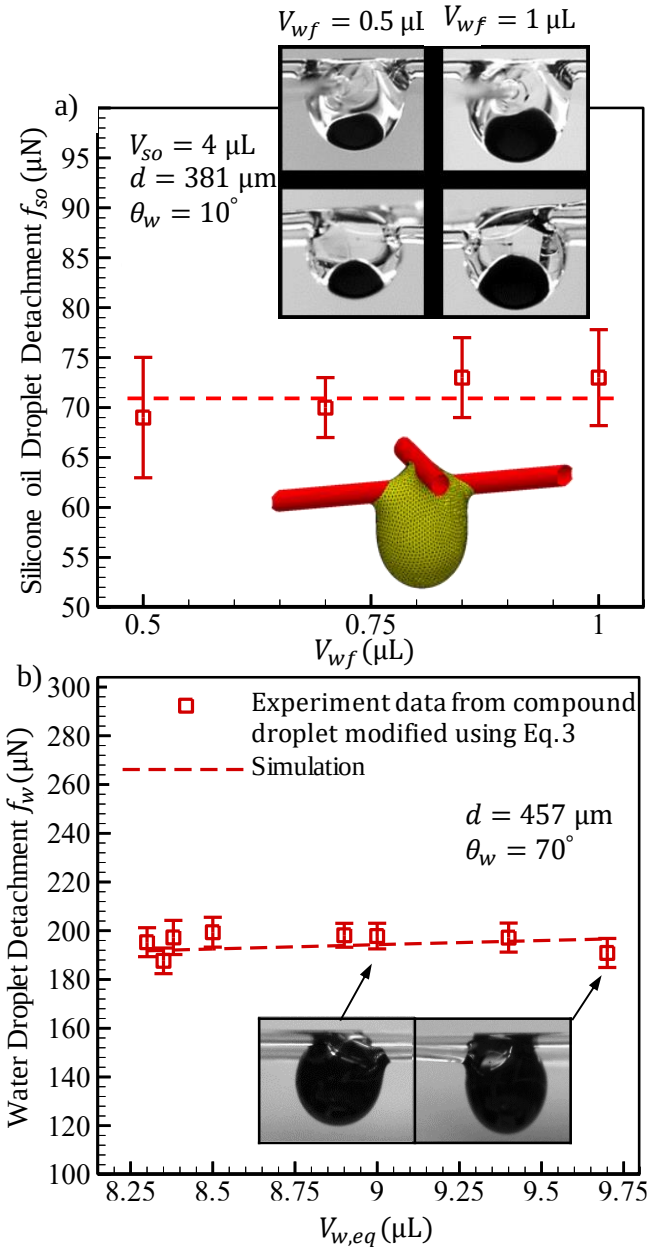

Figure 4.9: The force required to detach a silicone oil droplet from two intersecting fibers is reported in (a) for when it was compounded with nesting (aqueous) ferrofluid droplets of different volumes. The force required to detach a pure water droplet from two intersecting fibers is reported in (b). These data were obtained by magnetically measuring the force of detachment using compound droplets (ferrofluid-cloaked water droplets) but scaled using Eqs. 4.3 and 4.5 so that they can be applied to pure water droplets. Examples of the compound droplets used in the experiment are shown in the inset images in (a) and (b). Numerical simulation results obtained for detaching pure water droplets are also shown in (a) and (b) with red dashed-lines for comparison.

Figure 4.9b shows the force required to detach a cloaked water droplet from two intersecting (orthogonal) fibers with a diameter of $d = 457\ \mu m$ and an YLCA of $\theta_{w-of} = 81^{\circ}$. Examples of the compound (cloaked) droplets are shown as inset. Note that, unlike the case of detachment from a single fiber (Sections 4.3 and 4.4), where a universally-applicable correlation for droplet detachment force was used (i.e., Eq. 4.5 from Ref. [Farhan and Tafreshi 2018]), no such correlation exists for the case of droplet detachment from intersecting fibers. In this concern, we conducted an experiment with a single fiber (with the same compound droplet) and used Eq. 4.5 to estimate an effective surface tension σ_{w-of} for the compound droplet detaching from the intersecting fibers.

Numerical simulation results obtained for a water droplet from the same intersecting fibers are also shown with red dashed-lines for comparison. Good agreement can be seen between the detachment forces from experiment with compound droplets (after scaling for water via Eq. 4.3) and their computational counterparts obtained directly for water droplet detachment.

4.6 Compound Droplet Detachment using Gravity

The traditional, and perhaps the simplest, way to study capillarity of a fiber has been to increase the volume of a droplet hanging from the fiber until the droplet falls under its own weight (i.e., until the force per unit mass needed to detach the droplet becomes as small as the gravitational acceleration, g). This method, obviously, cannot be used for droplet detachment force measurement when the droplet of interest has a specific volume. However, as reported recently in [Weyer *et al*. 2015], such a measurement can be possible when using a compound droplet. The authors in Ref. [Weyer *et al*. 2015] considered pure water and soapy water as their primary fluids and used silicone oil as the secondary fluid to create different compound droplets. They then increased the volume of the silicone oil until the compound droplets were too heavy

to stay on the fiber. In this section, we discuss how this method can be used in our work for droplet detachment force measurement. For the case where the secondary fluid nests inside the primary fluid (Section 4.3), the abovementioned volume-increase method is obviously not applicable. This is because increasing the volume of the secondary fluid results in the secondary fluid coming into contact with the fiber. On the other hand, when the secondary fluid cloaks the primary droplet, the scenario is somewhat different, as is discussed in the next paragraph.

For this analysis, we produced compound droplets with water as the primary fluid and the oil-based ferrofluid as the secondary fluid (using the oil-based ferrofluid allows us to compare the results of volume-increase method with those obtained from using a magnet). We placed water droplets of different volumes V_w on a fiber, and added as much ferrofluid as needed until the resulting compound droplets became too heavy to stay on the fiber (see Fig. 4.10a). As can be seen in Fig. 4.10b, the total droplet volume ($V_m = V_w + V_{of}$) needed to detach a water droplet with a volume of V_w increases with increasing V_w. This is similar to the behavior reported in [Weyer *et al*. 2015] for compound droplets made with water and silicone oil. Repeating the same experiment with fibers having different diameters and YLCAs, we observed a similar trend, but the results were not independent of the YLCA or diameter of the fibers used for the experiment (unlike the data reported in [Weyer *et al*. 2015]). Our results show that V_m increases with increasing fiber diameter or decreeing the YLCA of the fiber. This agrees well with our previous work (Ref. [Farhan and Tafreshi 2018]) where we showed that for the gravity to be the detachment acceleration (detachment force per mass of the droplet), droplet volume should decrease with decreasing fiber dimeter.

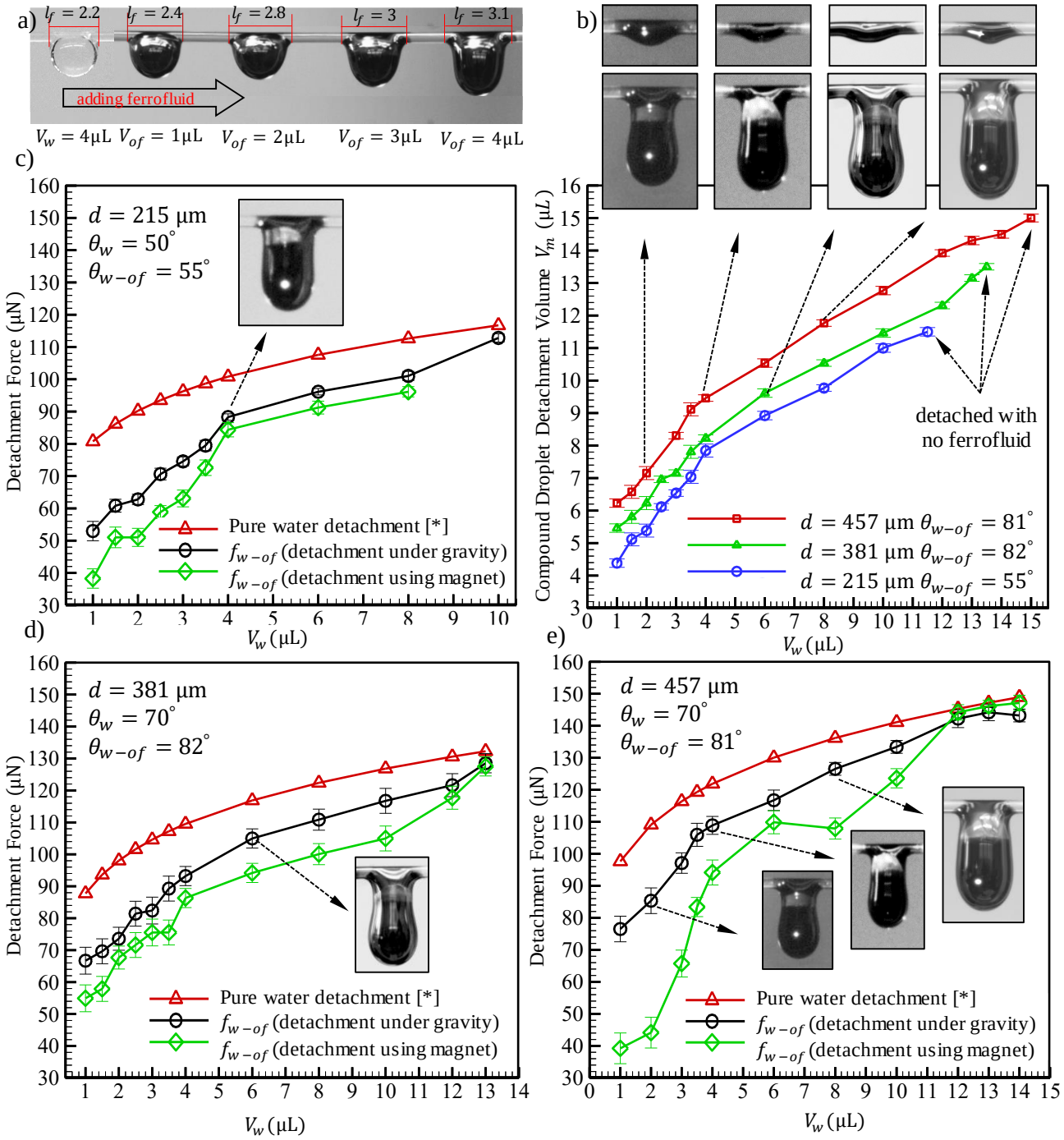

Figure 4.10: The steps of adding an oil-based ferrofluid to a pendent water droplet with a volume of 4μL are shown in (a). The length of the fiber's wetted area (viewed from the transverse direction) l_f is measured (in millimeters) and added to the figures for comparison. The detachment volume for compound droplets ($V_m = V_w + V_{of}$) is given in (b) as a function of the volume of the primary (water) droplet. The inset images in (b) show the final equilibrium state of different compound droplets (water droplets cloaked with the oil-based ferrofluid). Detachment force for pure water droplet (red line), compound droplet under gravity (black line), and compound droplet under magnetic force (green line) are given in (c), (d), and (e) for fibers with a diameter of $d = 215, 381,$ and 457 μm, respectivley. Note that Ref. [*] in (c-e) refers to Ref. [Farhan and Tafreshi 2018].

The inset images in Figure 4.10b show different compound droplets near the detachment moment. It can be seen that the ferrofluid cloaks the water droplet all the way to the fiber, although the cloak is thicker near the bottom and thinner on the top (note the black color on the fiber and the ferrofluid residue left on the fiber after detachment).

Figures 4.10c-e show detachment force for water droplets of different volumes (red line) from the same three fibers. These forces are obtained from Eq. 4.5 with surface tension and YLCA of water as inputs. Figures 4.10c-e also present detachment force for the same water droplets but when compounded with the cloaking ferrofluid. The black lines in these figures show the case were gravity was used for droplet detachment (i.e., the volume of the ferrofluid was increased until the compound droplet detached under gravity). It can clearly be seen that the force needs to detach a water droplet with a volume of V_w is higher than the force needed to detach the same droplet when it was cloaked with ferrofluid (with a volume of V_{of}). This is because the surface tension of the compound droplets is less than that of water, and also their YLCA with the material of the fiber is somewhat higher than that of water. Note that the detachment forces shown with black lines in Figures 4.10c–e correspond to compound droplet detachment volumes V_m shown in Figure 4.10b. Note that the behavior we observed with our compound droplets does not agree with that reported in Ref. [Weyer *et al*. 2015] for water (or soapy water) droplets compounded with silicone oil.

The green lines in Figure 4.10c–e show the case where the detachment was induced by a magnetic field (i.e., only a small volume of ferrofluid was used in making the compound droplets). Note that, the detachment forces shown with green lines are the same data used in Eqs. 4.3 and 4.5 to produce water droplet detachment forces in Figure 4.8c. In other words, the data obtained from compound droplet detachment need to be scaled before they can be used for water droplet, as mentioned earlier in Sections 4.4 and 4.5.

Note in Figure 4.10a that, adding more ferrofluid to the water droplet (from left to right), the wetted area of the fiber increases with the increase in the volume of the resulting compound droplet. The increased wetted area (i.e., increased contact line) lead to an increase in the force needed to detach the droplet (even with the effective surface tension of the compound droplet decreasing with increasing the volume of the ferrofluid). Therefore, less force is needed to detach a compound droplet when it contains less ferrofluid (and that is why the green lines are below the black lines in Figures 4.10c–e). Using the data shown with black lines in Eqs. 4.5 and 4.3, we obtained detachment force data that can be assigned to water droplets with a volume equal to that of the compound droplet (i.e., $V_{w,eq} = V_w + V_{of}$) as can be seen in Figure 4.11a. Same as the case shown in Figure 4.8c, numerical simulation results obtained for a water droplet with a volume of $V_{w,eq}$ are added to this figure, and excellent agreement can be seen between the results obtained for water droplet detachment and data from compound droplet detachment experiment after scaling.

We also conducted a series of single-fiber detachment experiments using the volume-increase method (detachment under gravity) with compound droplets having different ferrofluid-to-water volume ratios $\eta = \frac{V_{of}}{V_w}$. We then used the resulting forces F_{w-of} in Eq. 4.5 to obtain effective surface tension values for cloaked droplets with of different ferrofluid-to-water volume ratios (see Figure 4.11b). Fitting a 2nd order polynomial to these data (regardless of the fiber used for droplet detachment experiment), a semi-empirical correlation is developed for the effective surface tension of our compound droplets comprised of a water droplet cloaked by oil-based ferrofluid.

$$\sigma_{w-of} = \sigma_w - \alpha\,\eta + \beta\,\eta^2 \tag{4.6}$$

where $\beta = 0.002$ N/m and $\alpha = 0.015$ N/m.

Equation 4.6 circumvents the need for using Eq. 4.5 to obtain σ_{w-of} when doing the droplet detachment using gravity. It is interesting to note in this figure that increasing $\eta = \frac{V_{of}}{V_w}$ the effective interfacial tension σ_{w-of} reaches a plateau of about 0.049 N/m which is close to the value one can obtain using the equation given in Ref. [Marmur and Valal 2010] for a droplet submerged in a bath of another fluid.

$$\sigma_{w-of} = \frac{\cosh\left(\frac{\sigma_w}{k}\right)\sigma_w^{1-m} - \cosh\left(\frac{\sigma_{of}}{k}\right)\sigma_{of}^{1-m}}{\cosh\left(\frac{\sigma_w+\sigma_{of}-c\,\sigma_w^n\,\sigma_{of}^{1-n}}{k}\right)(\sigma_w+\sigma_{of}-c\,\sigma_w^n\,\sigma_{of}^{1-n})^{-m}} \tag{4.7}$$

where $m = 0.93884$, $n = 0.94965$, $c = 0.83755$ $k = 42.121$ mN/m. Using the surface tension of our oil-based ferrofluid σ_{of} and water σ_w from Table 1, we obtain an effective surface tension of $\sigma_{w-of} = 0.049$ N/m.

We also observed that the effective surface tension values given in Figure 4.11b (or Eq. 4.6) are not very accurate when used for predicting droplet detachment force if detachment is made magnetically. This probably is due to the way the effective surface tension is defined in our work, i.e., based on detachment force per unit droplet mass, which varies from one case to other when using a magnet for droplet detachment (as opposed to when using earth's gravity). Note also that the amount of ferrofluid used for droplet detachment with a magnet is quite small compared to the volume of the primary droplet.

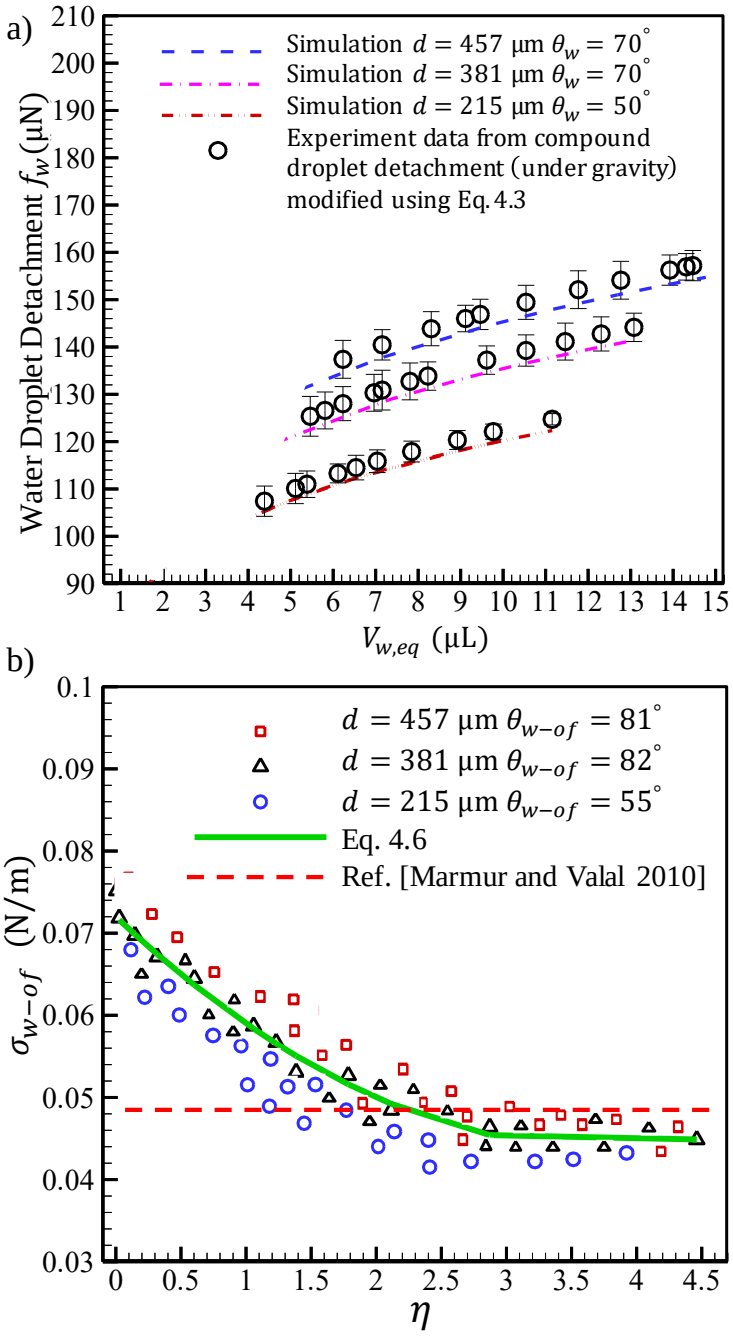

Figure 4.11: Detachment force data obtained for ferrofluid-cloaked water droplets under gravity and scaled (Eqs. 4.6 and 4.3) to represent detachment force for pure water droplets in (a). Numerical simulation results obtained for pure water droplet are also shown for comparison. Effective surface for ferrofluid-cloaked water droplets is given in (b) as a function of ferrofluid-to-water volume ratio $\eta = \frac{V_{of}}{V_w}$. The effective surface tension values converge to that predicted in Ref. [Marmur and Valal 2010] when large amounts of ferrofluids are used in cloaking the inner water droplet (for detachment using earth's gravity).

4.7 Conclusions

In this work, we present a new approach to obtain the force required to detach a nonmagnetic droplet from a fiber using a magnetic force, for the first time. This method allows one to measure the force of detachment without the need for using an external object, an airflow, or a centrifugal device. The proposed method is based on creating a compound droplet comprised of the droplet of interest (primary fluid) and a ferrofluid (secondary fluid). More specifically, we measured the force of detachment for a silicone oil (a non-polar fluid) deposited on a fiber by injecting a small amount of aqueous ferrofluid inside it in the form of a nested droplet, and then used a magnet to detach the resulting compound droplet. To repeat the experiment for a non-polar liquid (DI water), we used a kerosene oil-based ferrofluid to cloak the primary droplet and then detach it. The force obtained from detaching the compound droplet was then used to calculate the force of detachment for the original (primary) droplet. Good agreement was observed between the forces measured experimentally and those obtained from numerical simulation.

Chapter 5. Modeling Droplets in Cassie and Wenzel States over Granular Coatings

5.1 Introduction

Hydrophobicity of Louts leaves have motivated many studies to apply the leaf morphology on material surfaces [Gao and McCarthy 2006] since the hydrophobicity of surfaces has some advantages, such as excellent self-cleaning [Extrand 2011], drug reduction [Davis and Lauga 2009] and underwater protection of electronic devices [Ganne *et al.* 2016] among many other applications. The Super hydrophobicity is known for having contact angles exceeding 150° and low contact-angle hysteresis (i.e., the difference between the advancing and receding CAs) [Samaha *et al.* 2012]. Two dominant approaches to optimize the hydrophobicity which are a combination of surface morphology and/or surface chemical treatment. Substrate topology is necessary for developing the hydrophobicity and can potentially alter the wetting behavior of the substrate for a given chemical composition, which has been shown through many theoretical and experimental works [Que´ re´ 2002; Que´ re´ 2005; Callies and Que´ re´ 2005].

Understanding the physics of droplet displacement over rough surfaces and the wetting behavior have been received much attention since the pioneer works of Cassie-Baxter (CB) [Cassie and Baxter 1944] and Wenzel [Wenzel 1936]. When the valleys of the surface roughness are filled with air, the system is considered to be at in the CB state. With decreasing the solid volume fraction (SVF), liquid drop penetrates into the roughness valleys and may displace the air underneath. This results in losing the hydrophobicity, and transition to the fully wetted state so-called Wenzel state.

Recent studies [Lu *et al.* 2015; Tie *et al.* 2015] are focused on the wetting phenomena of droplet on curved shape of microstructures. These works detail the measurement of the contact angle of a droplet on a 2D microstructures (which is different from the contact angle of the same liquid would form on a 3D pattern).

In this study, we extend the analysis to model a droplet sitting on more real surface structures, 3D granular protrusions structures having a similar micro-structure to the lotus leaf surface [Yamamoto *et al.* 2015; Extrand and Sung 2014]. Physically, the granular microtexture has some advantages like it is hardly involves edges and corners (compared to the pillar microtexture surface for example), and it can be fabricated easily. Also, it is difficult to erosion.

We establish a numerical simulation to model droplet sitting over a 3D granular rough surface to determine the apparent contact angle ACA and to investigate the wetting transition from Cassie to Wenzel state. The energy minimization approach has been used. This has achieved by using the Surface Evolver (SE) software [Brakke 1992] which has been used to study various kinds of interfacial phenomena [Dorrer and Rühe 2007; Promraksa and Chen 2012; David and Neumann 2012; Aziz *et al.* 2017]. The equilibrium states of droplet on the rough surfaces are predicted, and their stabilities are analyzed comprehensively. The effects of chemistry (Young-Laplace contact angle YLCA) and geometrical parameters for the microtexture on equilibrium ACA have been investigated.

5.2 Analytical Formula

It is well known that, the equilibrium YLCA (θ) of a droplet on a flat solid surface first described by Thomas Young in 1805. The contact angle of a liquid drop on an ideal solid surface is defined by the mechanical equilibrium of the drop under the action of three interfacial tensions:

$$\cos\theta = \frac{\gamma_{SA} - \gamma_{SL}}{\gamma_{LA}} \tag{5.1}$$

where γ_{SA}, γ_{SL}, and γ_{LA} are the surface tension at liquid–air, solid–air, and liquid–solid interfaces, respectively. For a rough solid surface, there are two wetting states, which are Wenzel state (i.e., liquid wets the surface to form a solid–liquid homogeneous interface) and Cassie state (i.e., liquid wets only the

top surfaces of the roughness to form a heterogeneous interface of solid–liquid and gas–liquid), see Fig.5.1a and 5.1b.

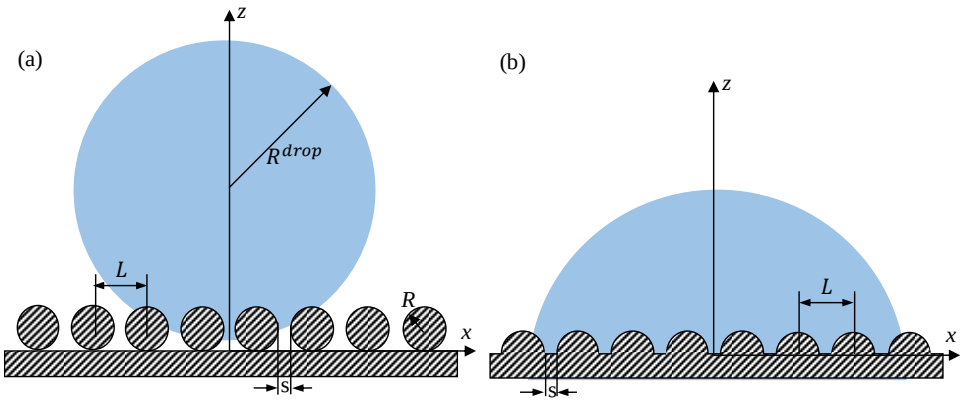

Figure 5.1: Schematics of the microstructure geometry of the solid surface with a droplet over it (a) Cassie state on hydrophobic spherical bumps. (b) Wenzel state on hydrophilic hemispherical bumps.

An ordered array of spherical particles on a flat surface, is shown in Fig. 5.1a and 5.1b. The radius of each bump is denoted by R, and the spacing between each two adjacent bumps is denoted by S. When the droplet size is smaller than the capillary length L_c, which is defined by $L_c = (\gamma/\rho g)^{1/2}$, where γ is the liquid surface tension, g the gravity acceleration, and ρ the liquid density, the effect of gravity is usually negligible [Wolansky and Marmur 1998]. In our simulation, the droplet size is much smaller than the capillary length to ignore the effect of the gravity. So, the liquid-air interface is circular because of the lack of gravity. Both the liquid drop and the solid surface on which it is placed are immersed in an ambient air.

5.2.1 Surfaces with ordered particles

The apparent contact angle θ^W, of the homogeneous wetting (fully wetted) state is typically described using Wenzel's equation,

$$\cos\theta^W = r\cos\theta \tag{5.2}$$

where r is the roughness factor defines as the ratio of the actual solid surface area to its projected area. This equation shows that roughness ($r > 1$) amplifies surface wettability and makes a hydrophilic ($\theta < \pi/2$) surfaces appear more hydrophilic and a hydrophobic surface more hydrophobic. The roughness factor for spherical bumps over a flat surface is,

$$r = 1 + \frac{4\pi R^2}{(S+2R)^2} \tag{5.3}$$

On the other hand, for the heterogeneous wetting (partially wetted) state, the apparent contact angle θ^{CB} is expressed by Cassie-Baxter (CB) equation as

$$\cos\theta^{CB} = r_f f\cos\theta + f - 1 \tag{5.4}$$

where f is the fraction of the projected of the wetted solid surface area (projected wetted area to the total projected solid area), and r_f is the roughness ratio of the wet area (wetted area to projected wetted area). For the Cassie-Baxter model, roughness always increases the apparent contact angle and makes any surface appear more hydrophobic. In this work for uniform distributed spherical bumps

$$r_f = \frac{2[1-\cos\alpha]}{\sin^2\alpha} \tag{5.5}$$

$$f = \frac{\pi R^2 \sin^2\alpha}{[S + 2R]^2} \tag{5.6}$$

When $f = 1$ and $r_f = r$, the CB equation turns into the Wenzel equation. The CB equation assumed the air-water interface is flat. The wetting angle $\alpha = \pi - \theta$ is constant and doesn't depend on the space changing between bumps. For uniform distributed particles and keeping the same size and YLCA for all particles, the CB equation will be

$$cos\theta^{CB} = 2\pi \left[\frac{R}{S + 2R}\right]^2 [(1 + \cos\theta)\cos\theta + 0.5(\sin^2\theta)] - 1 \tag{5.7}$$

5.2.2 Surfaces with bimodal particles

By assuming the particles consists of different materials and distributed uniformity over the substrate, each material is characterized by its own surface tension coefficients $\gamma_{SL,i}$ and $\gamma_{SA,i}$. The CB equation will be

$$cos\theta^{CB} = \sum_{i=1}^{n} r_{f,i}\, f_i\, \frac{\gamma_{SA,i} - \gamma_{SL,i}}{\gamma_{LA}} - f_A \tag{5.8}$$

where f_A is the ratio of the liquid–air area to the projected area (i.e., air fraction), $f_A = 1 - \sum_{i=1}^{n} f_i$. The roughness $\sum_{i=1}^{n} r_{f,i}\, f_i > 1$, is the ratio of the real surface in contact with liquid to its projection onto the horizontal plane. Comparing with Eq.5.1, so Eq. 5.8 can be written as

$$cos\theta^{CB} = \sum_{i=1}^{n} r_{f,i}\, f_i\, cos\theta_i - (1 - \sum_{i=1}^{n} f_i\,) \tag{5.9}$$

So, particles with two different YLCA θ_1 and θ_2 but the same size particles, Eq. 5.9 will be written as:

$$cos\theta^{CB} = \pi\left[\frac{R}{S+2R}\right]^2 [(1+cos\theta_1)cos\theta_1 + (1+cos\theta_2)cos\theta_2 + 0.5(sin^2\theta_1 + sin^2\theta_2)] - 1 \quad (5.10)$$

For the same YLCA θ particles but for two different sizes R_1 and R_2, Eq. 5.9 will be:

$$cos\theta^{CB} = \frac{\pi({R_1}^2 + {R_2}^2)}{[S+R_1+R_1]^2}[(1+\cos\theta)\cos\theta + 0.5\sin^2\theta] - 1 \quad (5.11)$$

5.3 Results and Discussion

As mentioned before, this study is reported on determining the ACA and transition from Cassie to Wenzel state of droplet sitting on 3D granular microstructures. The energy minimization has been used to interpret the wetting phenomena of droplet on that surfaces. The energy minimization theory is generally based on calculating the total surface energy for a droplet settling on an open microstructure surface, e.g., an isothermal system [Li W, and Amirfazli 2007; Kietzig *et al.* 2009]. The three-dimensional droplet simulations were achieved using the public-domain Surface Evolver software [Brakke 1992], which in essence minimizes the system free energy. We first define a suitable design parameter, *S* (the spacing parameter) to correlate the measured apparent contact angles for the transition from Cassie to Wenzel state. For any given contact angle θ for particles and substrate, the equilibrium apparent contact angles of the droplet are controlled by the feature spacing. We seek to correlate the apparent contact angle of a droplet in Cassie and Wenzel states as a function to the bumps size, distribution and wettability.

5.3.1 Wenzel state for hemispherical bumps

In this section, we considered a droplet in Wenzel state siting on hemispherical bumps as shown in Fig.5.1b. By changing the bumps size R and spacing S but keeping the roughness factor $r = 1 + \frac{\pi R^2}{(S+2R)^2}$ constant ($r = 1.349$), we studied the effect of bumps availability on the measured ACA for a constant droplet volume ($V = 0.1$ µL), see Fig 5.2a-d.

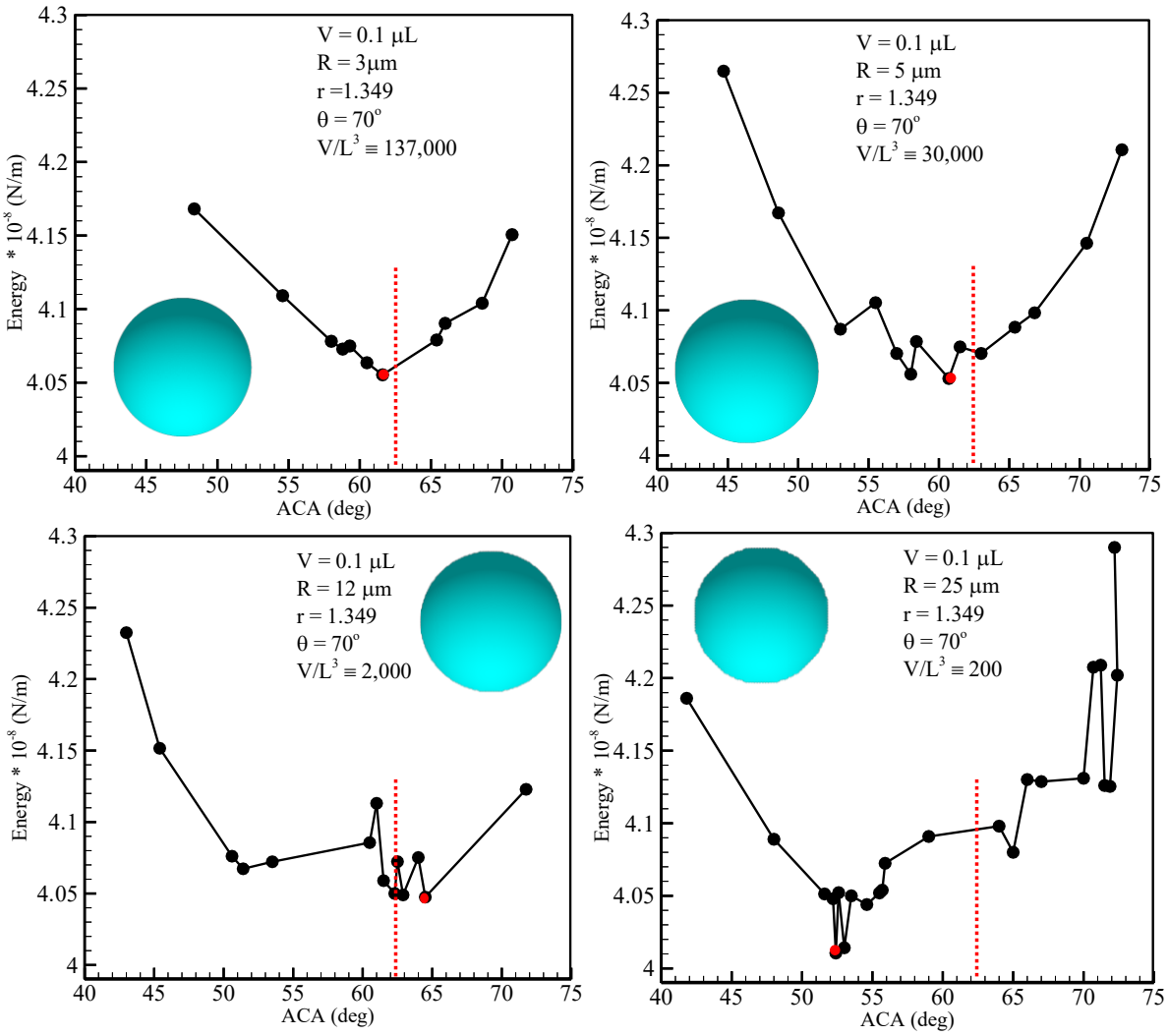

Figure 5.2: Wenzel evolution of free energy as a function of apparent contact angle for the system to reach its metastable state on a surface consisting of hemispherical bumps for different bumps radius and spacing (a) $R = 3$ (b) $R = 5$ (c) $R = 12$ (d) $R = 25$, with keeping the same roughness factor $r = 1.349$. The hemispherical bumps and the substrate are having the same YLCA $\theta = 70^o$. The red dot lines stand for the CA predicted by the Wenzel model (i.e θ^W). The red circular symbol is referring to the most stable ACA.

To see whether the measured ACA satisfy the Wenzel ACA θ^Wor not, the results will be discussed in relation to the relevant Wenzel angle. The red dot lines stand for the CA predicted by the Wenzel model (i.e θ^W). Note that the bumps and the substrate in Figure 5.2a-d have the same CA $\theta = 70^\circ$.

Figure 5.2a-d show that when the droplet is sufficiently large relatively to the wavelength L, almost a single minimum shows in the energy. The relative size of the drop to the surface wavelength is measured as

$$\gamma \equiv V/L^3 \tag{5.12}$$

where $L = S + 2R$ for identical bumps distributed uniformly. Figure 5.2a-d show four cases of different values of $\gamma \approx$ 137,000, 30,000, 2000, and 200, respectively. With decreasing γ value, the energy curves show more minimum points. The lowest minimum is the most stable one, while the others are metastable. The most stable ACA (the red circular symbol in the figures) is of interest here because it is supposed to be approximated by the Wenzel equation. The insets show the bottom view of the droplet (at the most stable point) is almost circle, so we don't need to measure the ACA from different views. The most stable CAs in these figures turn out to be $61.5^\circ, 61^\circ, 64^\circ$, and $52^\circ$for the above four values of γ, respectively. The most stable ACA in Fig. 5.2a-c are justified by Wenzel CA ($\theta^W = 62.5^\circ$), however, in Fig. 5.2d the ACA is different. To get a clear reason behind that is the approximation predicted by the Wenzel equation is sufficiently good when the relative drop size γ is large. How large is? from the present and previous work of [Brando *et al.* 2003], it appears that the relative size of about 3 orders of magnitude may be satisfactory. Intuitively, this observation can be explained by saying that when the relative drop size is sufficiently large, the surface appears to be uniform to the drop; therefore, the Wenzel averaging approach is justified. Figure 5.3a-d show the ACA determined for a droplet in Wenzel state sitting on hemispherical bumps in bimodal configuration (see in inset) with keeping the same roughness $r = 1.349$. The black symbols show the most stable states, while the dot lines stand for the CA predicted by the Wenzel model. For bimodal

hemispherical bumps $r = 1 + \frac{\pi(R_S^2+R_L^2)}{2(S+R_S+R_L)^2}$ where R_S and R_L are radius of small and large bumps, respectively. In Fig. 5.3a-b, the droplet is simulated at different bumps radius ($R_S = 3$ µm, $R_L = 6$ µm, and $R_S = 5$ µm, $R_L = 15$ µm, respectively) to explore the bimodal size configuration effect on the ACA with keeping the surface roughness factor r and the droplet volume V the same. The most stable CAs satisfy with Wensel model while $\gamma > 1000$. In Fig. 5.3c-d, for the same bumps sizes ($R_S = 7.5$ µm, $R_L = 10$ µm) but different droplet volumes, the most stable CA is closer to Wenzel model as $\gamma > 1000$.

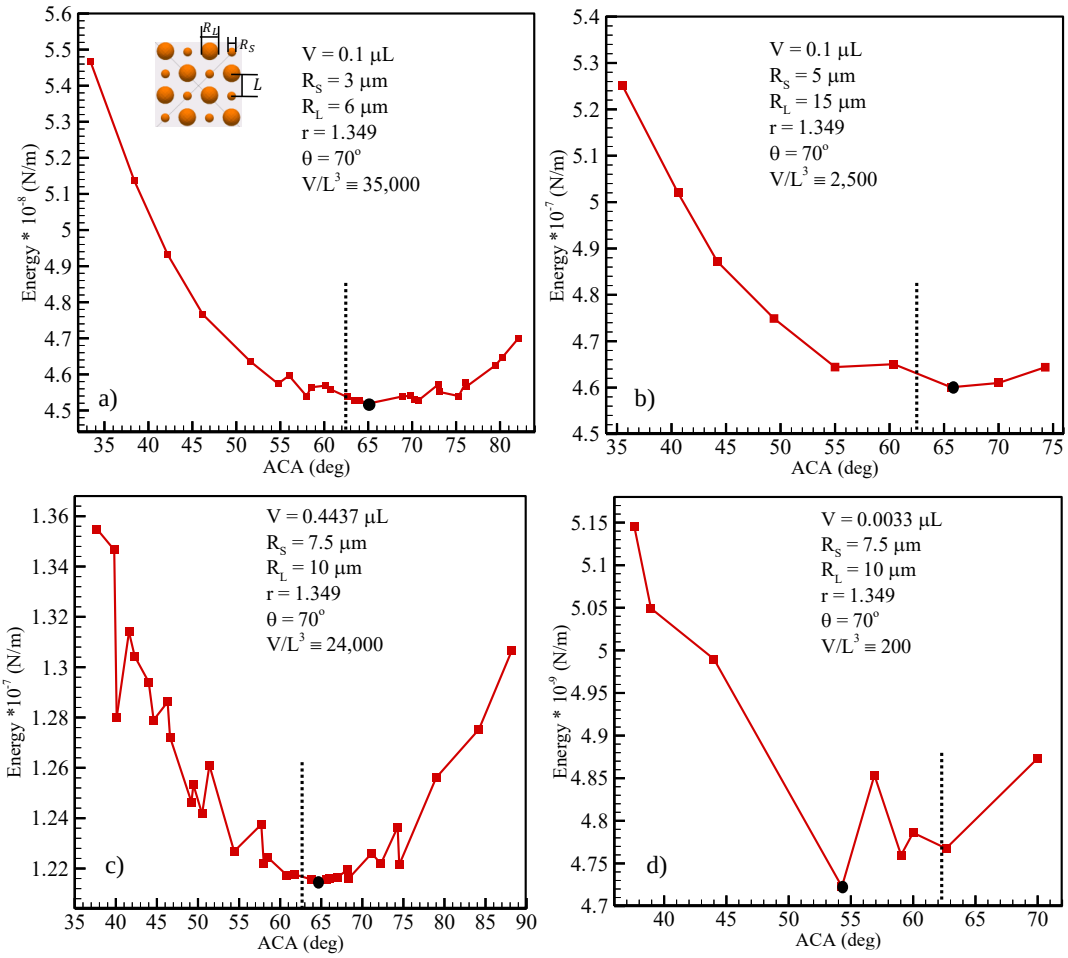

Figure 5.3: Wenzel evolution of free energy vs apparent contact angle for the system to reach its metastable state on a surface consisting of hemispherical bumps in bimodal configuration with keeping the same roughness factor $r = 1.349$. (a) $R_S = 3$ µm, $R_L = 6$ µm, $V = 0.1$µL (b) $R_S = 5$ µm, $R_L = 15$ µm, $V = 0.1$µL (c) $R_S = 7.5$ µm, $R_L = 10$ µm, $V = 0.4437$µL (d) $R_S = 7.5$ µm, $R_L = 10$ µm, $V = 0.0033$µL. The inset shows the bumps distribution and dimensions. The black dot lines stand for the CA predicted by the Wenzel model (i.e θ^W). The red circular symbol is referring to the most stable ACA.

So, we conclude from Fig. 5.2 and Fig.5.3 that Wenzel model can precisely predict the most stable (equilibrium) ACA for different roughness size and configuration unless we take care of the relative drop size γ that is important and it should be approximately about 3 orders of magnitude. That agrees with the work of Refs. [Wolansky and Marmur 1999; Brandon *et al.* 2003] that Wenzel equation is approximation which becomes correct only if the size ratio of the droplet to the roughness wavelength is sufficiently large.

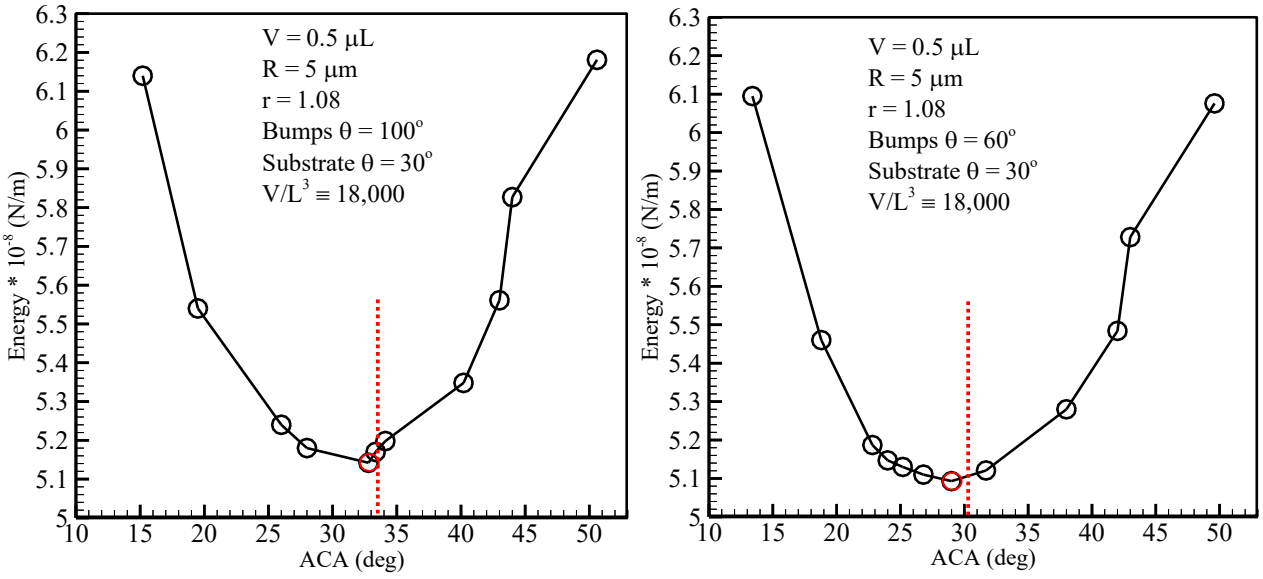

Figure 5.4: Wenzel state for hemispherical bumps with CA (a) 100° and (b) 60° for bumps and 30° for the substrate. The red dot lines stand for the CA predicted by the Wenzel model (i.e θ^{W}). The red circular symbol is referring to the most stable ACA.

Figure 5.4a-b show a computational investigation on the effects of different CA between bumps and substrate (keeping the same roughness ratio $r = 1.08$, bumps size $R = 5$ μm, and droplet volume $V =$ 0.5 μL) on minima in the free energy of three-dimensional droplets in Wenzel state. In Fig. 5.4a-b, the liquid droplet is resting on hemispherical bumps with CA 100° and 60° respectively and substrate CA 30°. For the roughness ratio $r = 1.08$, and bumps size $R = 5$ μm, the bumps are far away from each other with spacing $S = 4R$. So, Fig. 5.4 a-b present the cases of a relatively large drop whose most of triple

contact line is in contact with the substrate rather than the bumps. The most stable CAs in Fig. 5.4 a-b are $32.7^{\circ}$and 29°, respectively, that is approaching the substrate CA 30° where it is smooth; means there is no bumps. We conclude from Fig. 5.4 a-b that the contact angle of minimum energy depends on the roughness factor r more than the bumps or substrate CA. Because the bumps are far away from each other $S = 4R$, their effect is too small on the droplet shape (ACA). In this case, the contribution of the substrate CA has a big effect on the droplet ACA.

5.3.2 Cassie to Wenzel transition for hemispherical bumps

In this section, we considered a droplet in Cassie state siting on hemispherical bumps as shown in Fig.5.5a. By changing the bumps spacing S but keeping the bumps size R, bumps CA, droplet volume V, and the substrate CA all constant, we studied the effect of changing the bumps spacing on the measured ACA and the transition from Cassie to Wenzel state, see Fig 5.5b. Figure 5.5b shows the transition from Cassie to Wenzel state as a function to the wavelength $L = S + 2R$ between the bumps under constant volume of the droplet. The ACA determined at 0° and 45° views since the projected wetting area is not circular, see Figs. Fig. 5.5c-h.

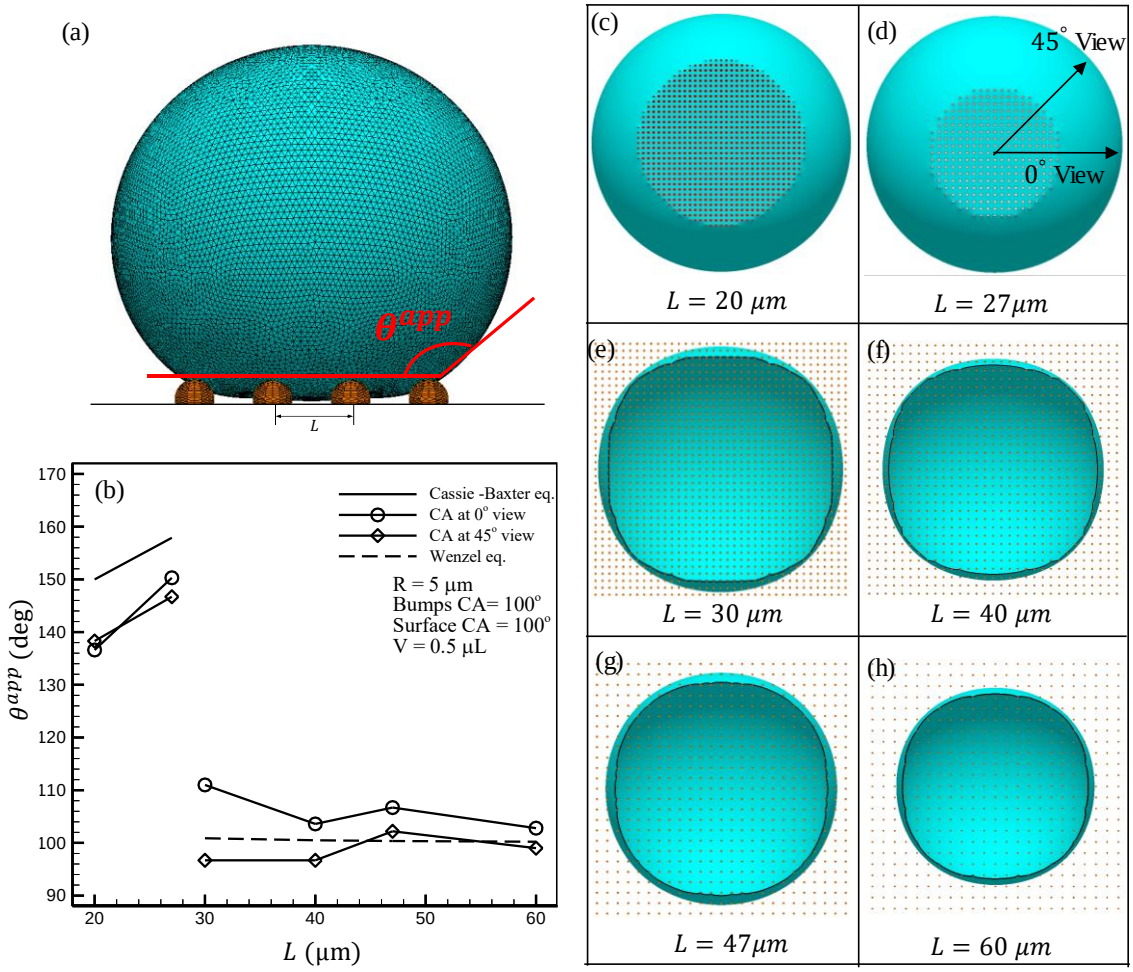

Figure 5.5: (a) front view of a droplet in Cassie state sitting on hemispherical bumps obtained from SE simulation. (b)ACA measured as a function to wavelength $L = S + 2R$ for a series of coatings with hemispherical bumps in ordered distribution and having similar YLCAs and size. (c)-(h) bottom view of the droplet (its ACA measured in b) and the contact line shape for constant droplet volume ($V = 0.5$ μL) but different bumps wavelength L. The droplet is in Cassie state in (c)-(d), while it's in Wenzel state in (e)-(h).

In Cassie state ($L < 30$ μm), the ACA is increasing along with wavelength (Fig. 5.5b) because the wetting area is decreasing (the droplet touches less bumps), see the bottom view of the droplet showing in Fig. 5.5c-d. As you see in Fig. 5.5b, our measured ACA is less than Cassie-Baxter ACA since the last is derived for a flat interface and assumed the wetted area fraction is the same in each unit cell. While the reality (our study) represents curved interface between bumps. With curved interface the solid wetted area is bigger that leads to less ACA comparing to CB apparent contact angle.

In Wenzel state ($L \geq 30$ μm), the ACA decreases with wavelength L increasing since the contribution of the bumps' support is less with the wavelength increasing. Also, the most stable contact angles determined at the two different viewing angles (determined at 0° and 45° views) deviate from the Wenzel CA due to the non-circular and corrugated contact line, see Figs. 5.5e-h. Figures 5.5 e-h illustrate that the triple contact line is going to a circular shape with increasing the wavelength [Promraksa and Chen 2012], that decreases the difference in the ACA at the two different views gradually, see the three-phase contact line in Fig. 5.5 e-h with black color for illustration. So, it is interesting to find out that the contact angle is not uniform along the contact line and strongly depends on viewing angle to the droplet. Also, it depends on whether the droplet is supported by a bump at that view or not.

5.3.3 Cassie to Wenzel transition for spherical bumps

Increase the wavelength L leads to increase the ACA for the droplet, until the critical wavelength that the droplet transits to Wenzel state (low hydrophobicity). Fig. 5.6a shows that from materials have equilibrium YLCA ~100°, high ACAs can be achieved only due to the effect of roughness (using spherical bumps). We compared our results with Cassie-Baxter equation when the wavelength is less than the critical wavelength $L_{cr} \cong 66\ \mu m$. As mentioned before, with curved interface the solid wetted area is more that leads to less ACA comparing with CB apparent contact angle.

In Cassie state region $L < L_{cr}$, using spherical bumps is much better than hemispherical bumps to support the droplet from the fast transition to Wenzel state since the solid height in $z-$direction is double in this case ($z = 2R$) comparing with half spheres ($z = R$). For half spheres under the same conditions in Fig. 5.6a, the critical wavelength $L_{cr} \cong 30\ \mu m$ (see Fig. 5.5a). The shape of the contact lines for the system under Cassie condition is anisotropic shape when the L value becomes larger, with keeping the droplet

volume the same as shown in Fig. 5.6b-g. That leads to a little difference in the ACA at the two different views (0° and 45° with x-axis).

In Wenzel state region $L > L_{cr}$, the droplet ACA is close from the substrate CA 70°, showing that the bumps don't have that much effect on the droplet shape because the bumps are too spread out and their effect is too small on the droplet shape, see Fig. 5.6h-i. Also, since most of the three-phase contact line length will be in contact with the substrate (CA 70°) rather than the spheres (CA 100°), the droplet ACA will be close to the substrate CA (see Fig. 5.6 a when $L > L_{cr}$). Figure 5.6h-i show that the shape of the contact lines for the droplet in Wenzel state is circular that leads to no difference in the ACA at different views (0° and 45° views).

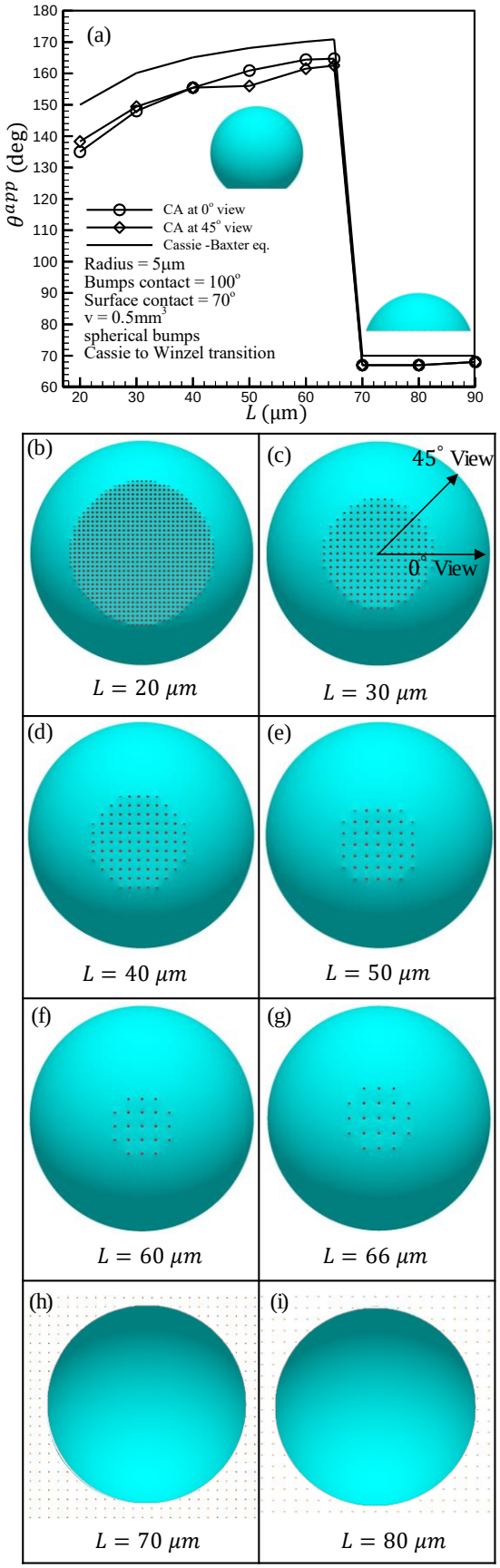

Figure 5.6: (a) The ACA as a function of wavelength L between particles (determined at 0° & 45°viewing angle with x-axis) with YLCA 100° and $70^{\circ}$for particles and substrate, respectively. (b)-(g) bottom view of droplet in Cassie state its ACA is showing in (a). (h)-(i) bottom view of droplet in Wenzel state with wavelength 70 μm and 80 μm, respectively.

By making a rough surface from a hydrophilic material, very high ACAs can be achieved only due to the effect of roughness (using spherical bumps) as shown in Fig. 5.7. Three-dimensional droplet is sitting over bumps with CA 85° and the substrate CA 70°. The ACA can reach 155° just because of increase the spacing between spherical bumps. However, the critical wavelength ($L_{cr} \cong 56\ \mu m$) is less than the case of bump CA 100° (comparing with Fig. 5.6a, the same particles size and distribution), because of the spheres are more philic that causes transition to Wenzel state with a small wavelength.

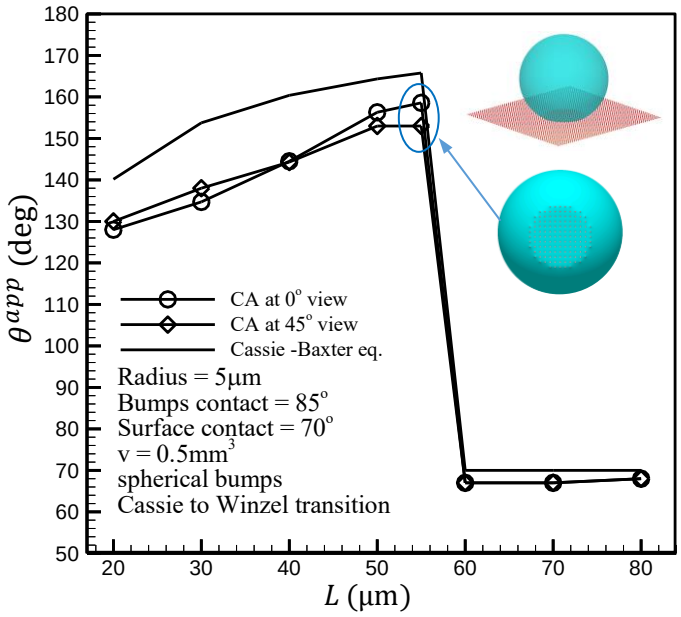

Figure 5.7: The droplet apparent contact angle as a function of wavelength L between particles (determined at 0° & 45° viewing angle with x-axis). The particles and substrate are hydrophilic with YLCA 85° and 70°, respectively.

Figure 5.8 shows the partial and fully wetting regions of chemically patterned surfaces. It presents the dependence of the ACA on the material wettability, quantified by YLCAs. Three-dimensional droplet in equilibrium with 3D pattern of chemical heterogeneity structure is computed and showed in Fig. 5.8. The chemical heterogeneity pattern consists of a periodic arrangement of particles of two types of chemistries (YLCAs) (100° & 60° in bimodal distribution). The inset shows an example of particles with a square

arrangement with different contact particles. The contact line of the droplet with the chemically heterogeneous surface has the freedom to adapt its local shape to conform to the condition that the local contact angle (CA) should conform to the value of the Young CA, assuming that line tension is negligible because it is important only for extremely small drops [Marmur 2006].

By looking to the results of Fig. 5.8 carefully, it seems that apparent contact angles of droplet and the critical wavelength ($L_{cr} \cong 56\ \mu m$) are similar to that predicted in Fig. 5.7 for particles with CA 85°. As a result, the bimodal chemical heterogeneity pattern is equivalent to the average of their bumps YLCAs. Note that the droplet volume ($V = 0.5$ µL), particles size ($R = 5$ µm), and substrate CA ($\theta = 70^{\circ}$) are the same in both Figs. 5.7 and 5.8. All the particles in Fig. 5.7 having the same CA ($\theta = 85^{\circ}$), but the particles in Fig. 5.8 are in bimodal chemical pattern and having two different CAs (100° and 60°).

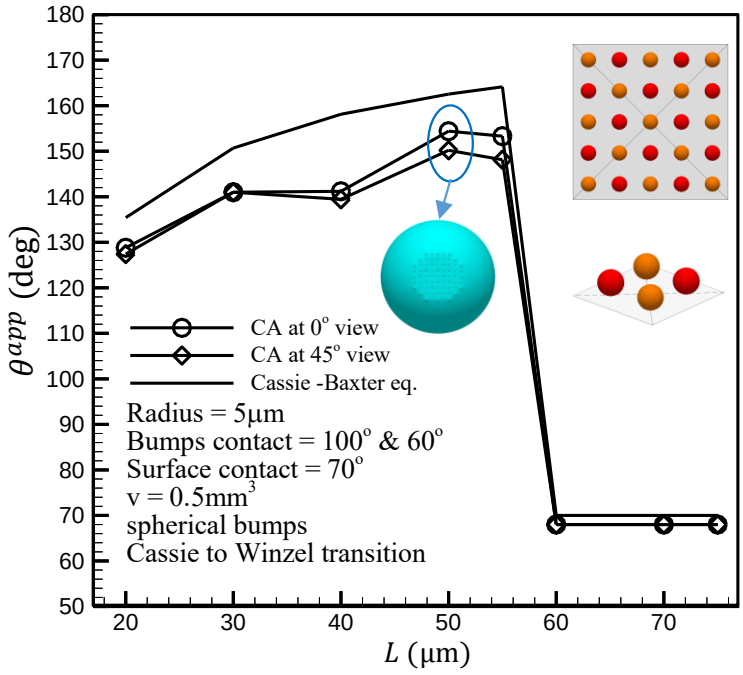

Figure 5.8: The apparent contact angle as a function of wavelength (determined at 0° & 45°viewing angle with x-axis) for two different particles YLCA (100° and 60° in bimodal distribution) and the substrate CA is 70°. The inset with two different color particles refers to two different YLCA.

Figure 5.9 shows contact angle as a function of spacing for two different particles radius (5 µm and 10 µm) in bimodal configuration, as you see at the top inset. The big differences in the most stable contact angle that determined at 0° & 45°viewing angle (rounded by ellipse in the same figure) because of the anisotropic wetting behavior us you see in the bottom insets. It is obvious that the liquid–solid contact area is not circular, as shown in insets, especially for $L \geq 40$ µm. The shapes of the liquid–solid interface strongly deviate from the circular shape and exhibit almost a diamond or square shape. This unusual and non-circular shape of the liquid–solid contact area is an outcome of wetting behavior along different defect density in perpendicular and diagonal directions of a square-arrays roughness pattern [Courbin *et al.* 2007]. Therefore, the contact angle of the final configuration of a liquid droplet strongly depends on viewing angle. That in consistent with Ref. [Promraksa and Chen 2012] which found that the contact angle variation around the droplet exhibits a periodic pattern repeated every 90°. So, the distortion of three-phase contact line by the roughness cannot be ignored.

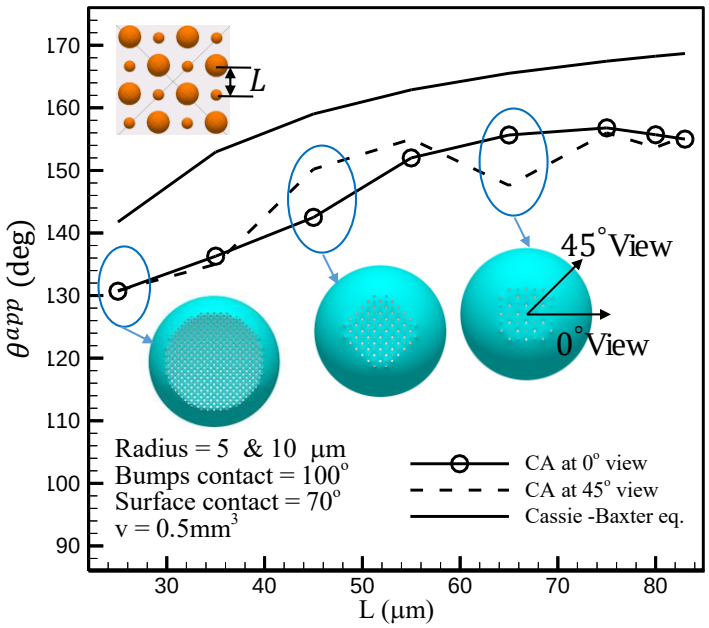

Figure 5.9: The droplet ACA as a function of wavelength (determined at 0° and 45°viewing angle). The droplet is in Cassie state with volume of $V = 0.5$ µL sitting on spherical particles in bimodal distribution with two different radii (5 µm and 10 µm). All the particles are having the same YLCA 100°. The top inset is showing the particles distribution and how the wavelength L is considered. The wave length in this figure is $L = s + R_L + R_S$.

The three-dimensional droplet shape in Cassie state is simulated and showed in Fig. 5.10 sitting on spherical particles in bimodal configuration. Figures 5.10a-b are showing the droplet bottom and front views, respectively, for constant volume droplet $V = 0.5$ µL sitting on spherical particles at different wavelength. Decreasing the wavelength reveals that the contact lines approach a circular shape. Note that the measured ACAs for the droplet showing in Figs. 5.10a-b are showed previously in Fig. 5.9.

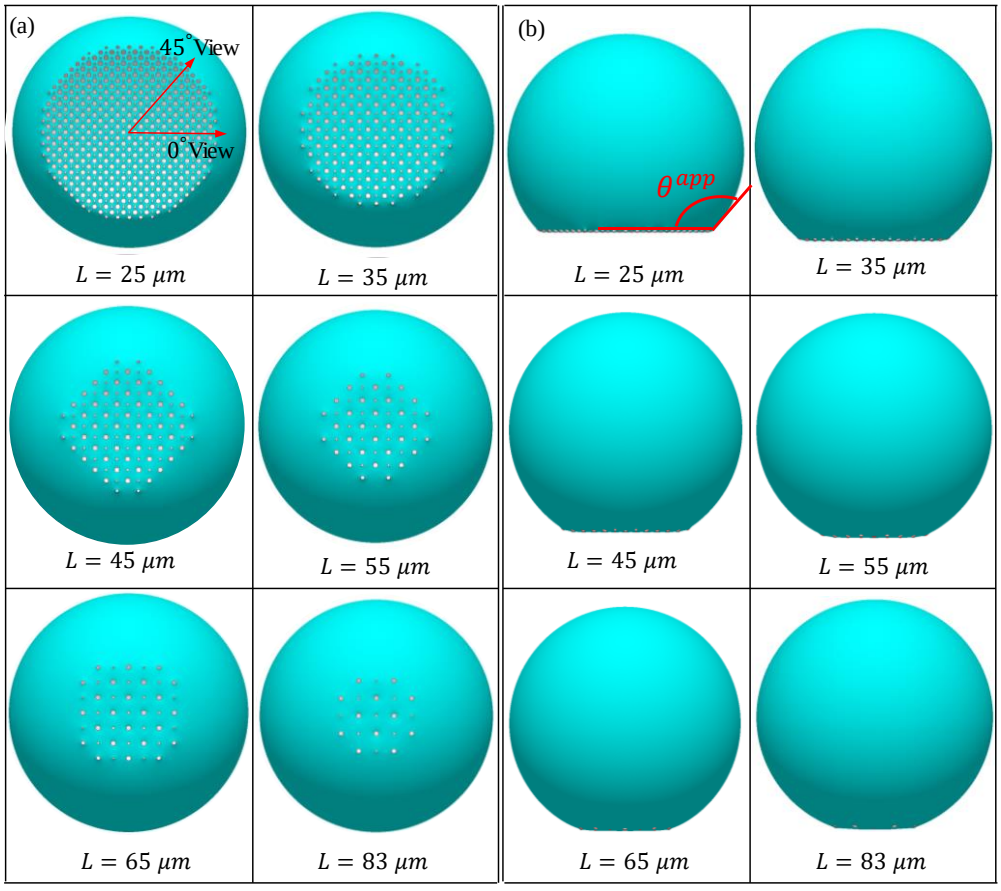

Figure 5.10: The images of (a) bottom (b) front views of a liquid droplet in the Cassie state for different wavelength L. The liquid–solid contact area is illustrated by white area and the liquid–air interface is illustrated by blue area, the particles large and small radius 5 µm and 10 µm in bimodal configuration, with $L = s + R_L + R_S$ and the same droplet size $V = 0.5$ µL. All the particles are having the same YLCA 100°.

5.3.4 Force balance analysis

Figure 5.11a shows the forces balance for the meniscus surrounding a spherical particle. The interaction between the droplet and bumps is more complicated, since the cross-section of the bumps changes as the droplet moves in the y-direction. Therefore, magnitude of the surface tension force F_σ changes depending on the height at which the interaction is located, characterized by the angle α, as can be seen in 5.11a. In our simulations, we considered the curvature of the air-water interface between the particles. So, to get the curvature of the interface, we should calculate the wetting angle α. Our derivation for the wetting angle α is based on the vertical forces balance, between the hydrostatic pressure P inside the droplet which act on the spheres and the capillary force F_σ which is a function to the surface tension σ and contact angle and acts on the circular three-phase contact line. From Fig. 5.11a, it can be seen that the capillary force F_σ is directed upward to recede the interface to the top of the particles, forming a composite solid-liquid-air interface. By applying forces balance in the y-direction at the three-phase contact line, the force balance analysis can be written as,

$$P \text{ (Interfacial area)} = \sigma \text{ (contact line length)} \sin(\theta + \alpha - \pi) \tag{5.13}$$

or

$$P\ (L^2 - \pi\, R^2 \sin^2\alpha) = -\,\sigma(2\pi\, R \sin\alpha) \sin(\theta + \alpha) \tag{5.14}$$

where P is Laplace pressure; which is the pressure difference between the inside and outside of a curved interface between liquid and gas region $P = \frac{2\,\sigma}{R^{drop}}$, R^{drop} is the droplet radius. By considering the droplet volume $V = \frac{4}{3}\pi\,(R^{drop})^3$ is constant and equal to 0.5 µL, the Laplace pressure $P = 292$ pa. The air pressure is usually assumed to be constant and equal to the ambient one. Figure 5.11b shows the angle α calculated for a droplet in Cassie state using Eq. 5.14 at different wavelength L. As can seen,α increases along with the wavelength, until it becomes almost constant when the droplet is about to transient to

Wenzel state. Note that droplet volume $V = 0.5$ µL and the spherical particles are in a uniform distribution having the same size $R = 5$ µm, and the same YLCA $\theta = 100^{\circ}$. The critical wavelength is $L_{cr} = 66$ µm.The results of Fig. 5.11b are for the case showed previously in Fig. 5.6.

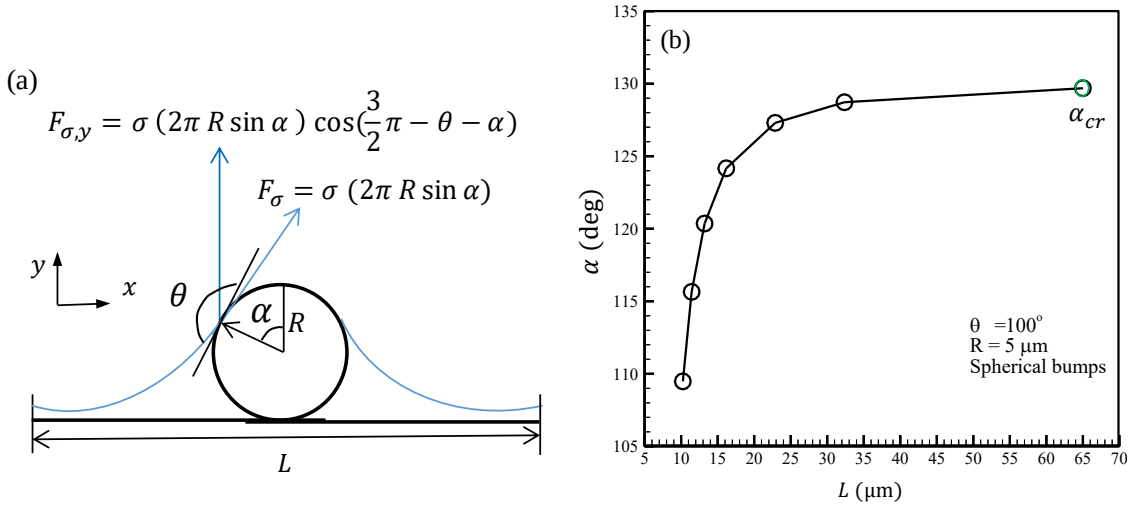

Figure 5.11: (a) the force balance analysis on the gas–liquid meniscus surrounding a spherical particle. Here, the component $F_{\sigma,y}$ denotes the surface tension force applied upward of the interface. (b) angle α calculated by our analytical method at different wavelength L. The droplet in Cassie state with volume $V = 0.5$ µL and the spherical particles are in a uniform distribution having the same size $R = 5$ µm, and the same YLCA $\theta = 100^{\circ}$. The results of (b) are for the case showed previously in Fig. 5.6.

As granular coatings, it is better to describe the pressure inside the droplet in terms of solid volume fraction (ε) we reformulated Eq. 5.14 in terms of the solid volume fraction for convenience;

$$P = \frac{-2\,\sigma\,\sin\alpha\,\sin(\theta+\alpha)}{R\left(\frac{4}{6\,\varepsilon} - \sin^2\alpha\right)} \tag{5.15}$$

where the solid volume fraction ε for the surface with ordered particles is calculated as $\varepsilon = \frac{2\pi\,R^2}{3\,L^2}$. To get the transition from Cassie to Wenzel state analytically, we should calculate the critical angle α_{cr} at which the hydrostatic pressure P is maximum and the surface departs from the Cassie state because the hydrostatic pressure becomes larger than the surface tension force beyond this point, and so the meniscus

can no longer withstand the pressure. As a result, the particles becomes immersed in water. This can affect the drag reduction significantly, or may even cause an increase in the skin-friction drag force. As a result, the hydrophobicity starts to diminish. The critical angle can be obtained by setting $(\frac{dP}{d\alpha})\Big|_{\alpha=\alpha_{cr}} = 0$

$$\left[\cos\alpha_{cr}\cos\left(\frac{3\pi}{2}-\theta-\alpha_{cr}\right)+\sin\alpha_{cr}\sin\left(\frac{3\pi}{2}-\theta-\alpha_{cr}\right)\right]\left(\frac{3}{2\varepsilon}-\sin^2\alpha_{cr}\right)$$

$$+2\sin^2\alpha_{cr}\cos\alpha_{cr}\ \cos\left(\frac{3\pi}{2}-\theta-\alpha_{cr}\right)=0 \qquad (5.16)$$

As can be seen from Eq. (5.16), the critical angle α_{cr} is only a function of the solid volume fraction ε. Figure 5.11b shows the critical angle $\alpha_{cr} = 129^{\circ}$ calculated at the critical wavelength $L_{cr} = 66$ µm.

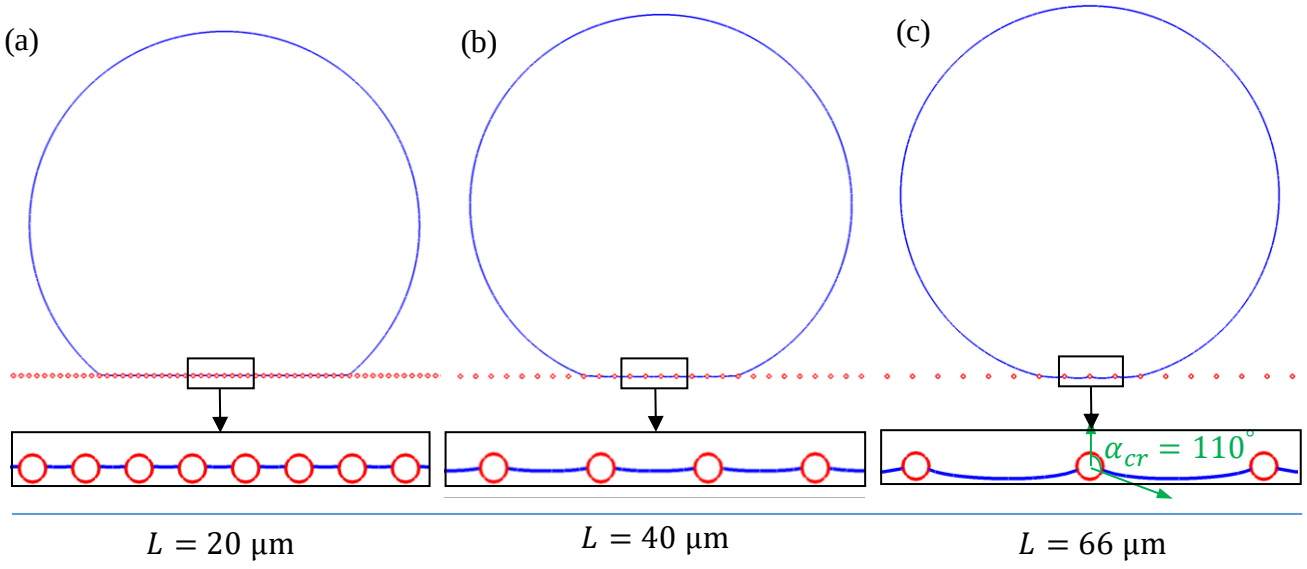

Figure 5.12: (a)-(c) Front slice view for the droplet that shows in Fig. 5.6 b, d, and g, respectively. That view determined at 0° viewing angle with x-axis.

Figure 5.12a-c show a slice view of the droplet in Cassi model (that was shown in Fig. 5.6 b, d, and g, respectively) determined at 0° view angle. With increasing the spacing between the particles, the droplet goes down more and the interface between particles becomes curved more. Until the droplet is to be so close from touching the substrate at the critical wavelength ($L_{cr} \cong 66$ μm when the CA of all particles is 100°). Under this condition, the measured critical immersion angle α_{cr} is 110°, while from the force balance analysis (Eq. 5.16) $\alpha_{cr} = 130^{\circ}$ at wavelength $L = 66$μm . The α_{cr} that comes from Eq. 5.16 can be happened as the pressure inside the droplet is equal to the critical pressure, while in our simulation α_{cr} defined as the angle the droplet touches the substrate. That can be happening under the sagging pressure that is less than the critical pressure. That explain the small immersion angle under the sagging pressure (see [Aziz *et al.* 2017] for more details). The pressure inside the droplet should be uniform since the air under the droplet is connected to the atmosphere with pressure uniform and equal to the atmospheric pressure. So, the curvature should be the same for all liquid-air interfaces; that is, the curvature of the liquid-air interfaces between bumps must equal that of the outside surface of the drop. But because of the droplet radius is much larger than the roughness scale, the curvature of the liquid-air interfaces inside the roughness valleys is much lower than that of the roughness features. In addition, these interfaces have to adjust their shape in such a way that the actual contact angle with each particle is satisfy the YLCA [Wolansky and Marmur 1998].

5.3.5 Modeling Droplet Displacement over Granular Coatings in Cassie State

Water droplet with volume $V = 0.5\ \mu L$ in Cassie state is sitting on granular surface. We applied a horizontal force on the droplet and measured the detachment force. We define the droplet detachment force here as the force needs to move the droplet on the surface forever. Means, we applied small horizontal force on the droplet and increased it gradually until the droplet leaves its equilibrium position totally. We noticed that with applying small force, the droplet starts detaching from the side opposite to force direction (the left droplet side in Fig. 5.13 and the applied force in the right direction).

There are different ways to define the detachment force according to the particles size and contact angle. Figure 5.13a-b show a droplet sitting on uniform distribution particles with radius $R = 5\ \mu m$. With applying a small force F_1 in the right side of the droplet, the droplet starts receding from the left side without touching new particles on the right side. So, that force $F_1$is less than the detachment force. We increased the force until the droplet touches a new particle from the right side, that force is the detachment force F_2. Its worth to mention that with applying F_2 the droplet keeps rolling on the surface and touching new particles without stopping.

For Bimodal contact angle particles (Fig. 5.13c-d), the equilibrium droplet sits on philic particles. With applying force, the droplet recedes from the philic to phobic particles and the force still less than the detachment force, until it touches a new philic particles with increasing the force that will be the detachment force. Foe bimodal particles size (Fig. 5.13e-f), the equilibrium droplet sits on large particle. With applying force, the droplet recedes from large to small particles and the force still less than the detachment force, until it touches a new large particle with increasing the force that will be the detachment force.

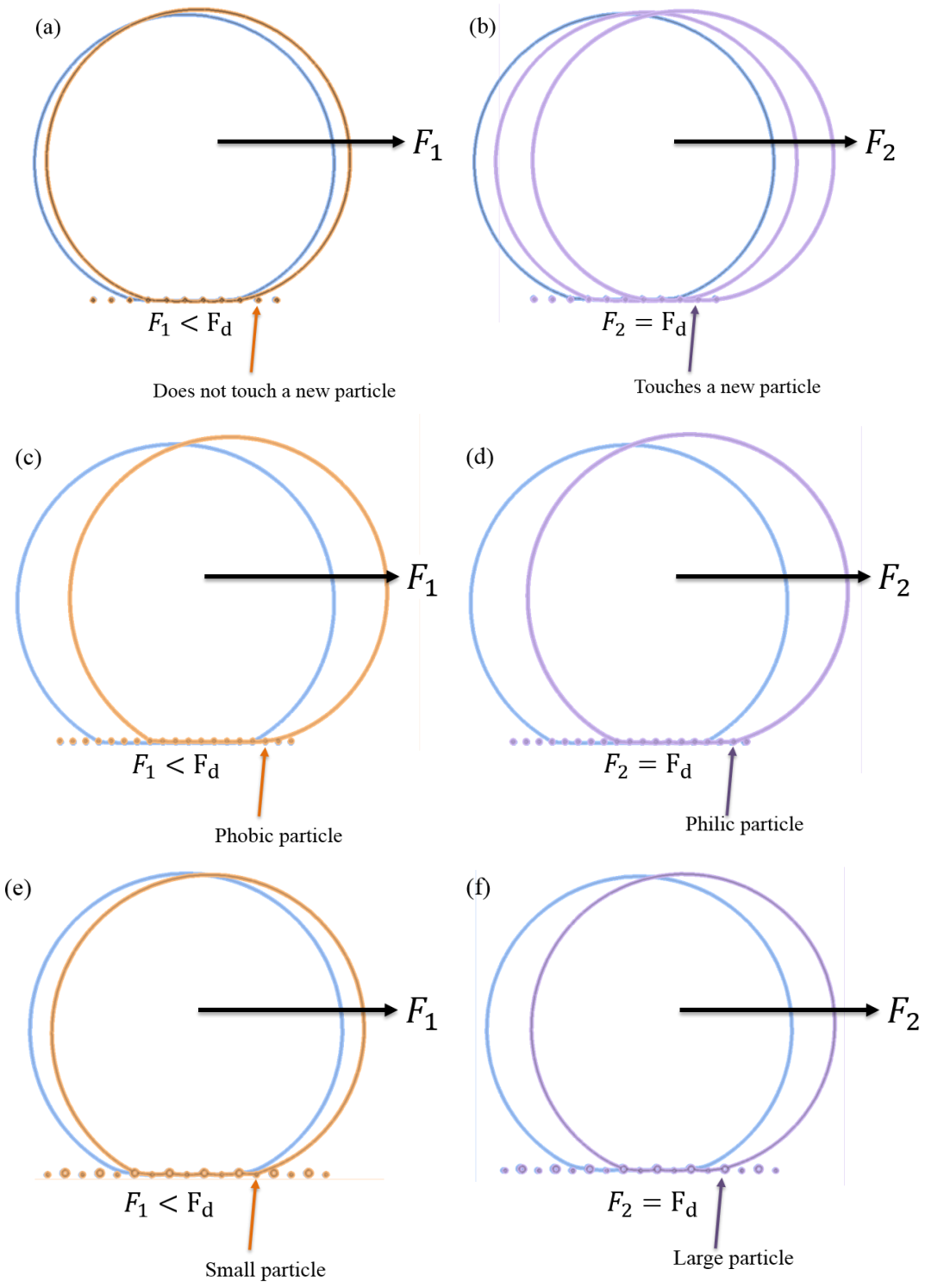

Figure 5.13: Water droplet with volume $V = 0.5$ µL in Cassie state sitting on granular surface with different configurations. (a) and (b) the same particles size $R = 5$ µm, and the same contact angle $\theta = 100^{\circ}$. (c) and (d) the same particles size $R = 5$µm, but bimodal particles contact angles $\theta_1 = 100^{\circ}$and $\theta_2 = 60^{\circ}$. (e) and (f) bimodal particles size $R_1 = 5$ µm and $R_2 = 10$ µm, but the same contact angle $\theta = 100^{\circ}$.

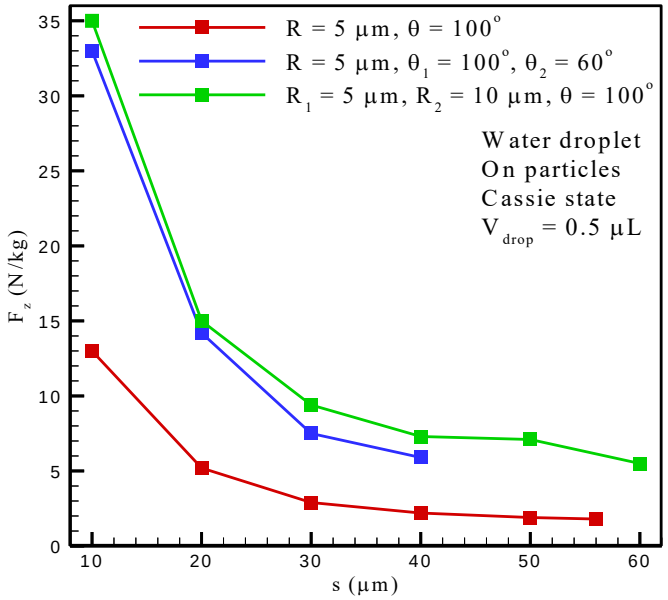

Figure 5.14: Water droplet with volume $V = 0.5$ µL in Cassie state sitting on granular surface. With increase the spacing s between the particle: the red line shows the droplet detachment force over particles radius $R = 5$ µm and contact angle $\theta = 100^{\circ}$, the blue line shows the droplet detachment force over particles radius $R = 5$ µm and bimodal contact angle $\theta_1 = 100^{\circ}$ and $\theta_2 = 60^{\circ}$, and the green line shows the droplet detachment force over bimodal particles radii $R_1 = 5$ µm and $R_2 = 10$ µm and contact angle $\theta = 100^{\circ}$.

Figure 5.14 shows how the detachment force of the droplet is decreasing with increase the spacing between the particles. The red line shows the detachment force for droplet over particles radius $R = 5$ µm and contact angle $\theta = 100^{\circ}$.With decrease the particle contact angle, the detachment force is increasing, but the critical spacing (the maximum spacing between the particle before the droplet touches the substrate) is decreasing since the interface between the particles will be curved more, see the blue line in Fig. 5.14. While with increase the particles size by doing bimodal, the detachment force is increasing more since the wetted area is increasing that needs more force to move the droplet over the particles, see the green line in Fig. 5.14. That increases the critical spacing, too. So, we suggest to increase the particles size instead of decreasing the particles contact angle to increase the detachment force and the critical spacing at the same time. Note that the gravity force is involved in this task.

5.4 Conclusions

This study dedicated for modeling apparent contact angle (ACA) of a droplet sitting on rough surfaces that are produced by placing granular protrusions (resembles natural SHP surfaces) arranged over a flat surface. The ACAs of the droplet are obtained at two different surface roughness (spherical and hemispherical bumps) and has been numerically investigated and carefully examined for Wenzel and Cassie model by using the Surface Evolver to perform the energy minimization. It is demonstrated that bumps' radius and intrinsic CA play a significant important role in the droplet ACA. Wenzel equation can predict the droplet ACA on a rough surface unless the relative size of the droplet volume to the surface wavelength is about 3 orders of magnitude. Increasing the roughness wavelength leads to an increase in the magnitude of the droplet apparent contact angles in Cassie state, but to decreasing the droplet ACA in Wenzel state.

For Wenzel and Cassie model, for a large wavelength between bumps, the ACA strongly depends on viewing angle since the shape of the contact line is not perfectly circle. Variation of the most stable contact angle as a function of viewing angle is due to distorted contact line. Distortion of the contact line by structure of the roughness maybe ignored if the size of droplet is very large compared with the size of roughness structure.

Chapter 6. Overall Conclusion

Experiment and numerical simulation were conducted to study the effects of fiber diameter, fiber YLCA, and droplet properties on the force required to detach a droplet from a fiber. We developed for the first time a semi-empirical correlation (see Eq. 2.15) that can predict the droplet detachment force from a fiber without the need for running an experiment or a computer simulation for YLCAs greater than about 20°. Considering a free body diagram for a droplet at its final equilibrium state under an external force on a fiber, it was found that droplet pressure plays an important role in the balance of forces acting on the droplet.

A new method to measure the YLCA of a fiber (i.e., the intrinsic CA of the material from which the fiber was made) is developed in this study. Experimental and computational results were produced to show that the CA measured from the longitudinal view for a droplet in the clamshell conformation on a fiber represents the YLCA of the fiber. It was also shown that the proposed measurement method is independent of the volume of the droplet used for the experiment, or the magnitude of the external body force acting on the droplet. The droplet-volume-independence is an important attribute of the proposed method, which is in contrast to the commonly-used inflection-angle method. In addition, the proposed method can be used with both wetting and non-wetting fibers, which is also in contrast to many previous methods. Our experimental results were compared with data from numerical simulation or alternative experimental methods and good agreement was observed.

In this work, we present a new approach to obtain the force required to detach a nonmagnetic droplet from a fiber using a magnetic force, for the first time. This method allows one to measure the force of detachment without the need for using an external object, an airflow, or a centrifugal device. The proposed

method is based on creating a compound droplet comprised of the droplet of interest (primary fluid) and a ferrofluid (secondary fluid). The force obtained from detaching the compound droplet was then used to calculate the force of detachment for the original (primary) droplet. Good agreement was observed between the forces measured experimentally and those obtained from numerical simulation.

For a droplet sitting on a granular coating, we found that Wenzel equation can be used to predict the droplet ACA on a rough surface unless the relative size of the droplet volume to the surface wavelength is about 3 orders of magnitude. Also, increasing the roughness wavelength shows an increasing in the droplet apparent contact angles in Cassie state, but decreasing the droplet ACA in Wenzel state.

References

Amrei MM, Davoudi M, Chase G, Tafreshi HV, *Sep. Purif. Technol.* **2017,** 180, 107– 113

Amrei MM, Venkateshan DG, D'Souza N, Atulasimha J, Tafreshi HV, *Langmuir*, **2016**, 32, 13333–13339.

Ataei M, Chen H, Tang T, Amirfazli A, *J. Colloid Interf. Sci.* **2017**, 492, 207-217.

Aziz H, Amrei MM, Dotivala A, Tang C, Tafreshi HV, *Colloid and Surf. A: Physicochem. Eng. Aspects* **2017**, 512, 61–70.

Aziz H, Farhan NM, Tafreshi HV, *Experiments in Fluids* **2018**, 59, 122.

Aziz H, Tafreshi, H. *Int. J. Multiph. Flow* **2018**, 98, 128–138.

Bai H, Tian X, Zheng Y, Ju J, Zhao Y, Jiang L, *Adv. Mater.* **2010,** 22, 5521–5525.

Bansal S, Sen P, *Langmuir* **2017**, 33, 11047−11058.

Bedarkar A, Wu XF, *J. Appl. Phys.* **2009**, 106, 113527.

Bracco G, Holst B, *Springer Series in Surface Science 51, Springer-verlag, Berlin, Heidelberg,* Chap. 1, **2013**, 3-34.

Brakke KA, *Experimental Mathematics* **1992**, 1, 141− 165.

Brandon S, Haimovich N, Yeger E, Marmur A, *J. Colloid Interface Sci.* **2003**, 263, 237–243.

Bormashenko E, *Colloid Polym. Sci.* **2013**, 291, 339−342.

Bormashenko EY, *Walter de Gruyter GmbH, Berlin/ Boston*, **2017**.

Bormashenko E, Bormashenko Y, *J. Phys. Chem. C* **2013**, 117, 19552−19557.

Bormashenko E, Bormashenko Y, Whyman G, Pogreb R, Musin A, Jager R, Barkay Z, *Langmuir* **2008**, 24, 4020.

Callies M, Que´ re´ D, *Soft Mat* **2005**, 1.55– 61.

Carroll BJ, *J. Colloid Interface Sci.* **1976**, 57, 488−495.

Carroll BJ, *J. Appl. Phys.* **1991**, 70, 493–494.

Cassie ABD, Baxter S, *Trans. Faraday Soc*. **1944**, 40, 546-51.

Charvet A, Gonthier Y, Bernis A, Gonze E, *Chemical Engineering Research and Design*, **2008**, 86, 569-576.

Chen D, Tan L, Liu H, Hu J, Li Y, Tang F, *Langmuir* **2010**, 7, 4675–4679.

Chen H, Amirfazli A, Tang T, *Langmuir* **2013**, 29, 3310−3319

Chen L, He Y-L, Tao W-Q, *J. of Heat and Mass Transfer* **2013**, 60, 252-262.

Chou T-H, Hong S-J, Liang Y-E, Tsao H-K, Sheng Y-J, *Langmuir* **2011**, 27, 3685-3692.

Clanet C, Quere D, *J. Fluid Mech*. **2002**, 460, 131–149.

Contal P, Simao J, Thomas D, Frising T, Calle S, Appert-Collin JC, Bemer D, *J. Aerosol Sci.* **2004**, 35, 263–278.

Courbin L, Denieul E, Dressaire E, Roper M, Ajdari A, Stone HA, *Nat. Mater.* **2007**, 6, 661.

De Ruiter R, de Ruiter J, Eral HB, Semprebon C, Brinkmann M, Mugele F, *Langmuir* **2012**, 28, 13300−13306.

Davoudi M, Fang J, Chase GG, *Separation and Purification Technology*, **2016**, 162, 1-5.

David R, Neumann AW, *Colloids Surf. A* **2012**, 393, 32.

Davis AMJ, Lauga E, *Phys. Fluids* **2009**, 21, 113101.

Dorrer C, Rühe J, *Langmuir* **2007**, 23, 3820.

Drelich J, *Surf. Innov.* **2013**, 1, 248–254.

Dong H, Cheng M, Zhang Y, Wei H, Shi F, *J. Mater. Chem. A* **2013**, 1, 5886–5891.

Eral HB, de Ruiter J, de Ruiter R, Oh JM, Semprebon C, Brinkmann M, Mugele F, *Soft Matter* **2011**, 7, 5138−5143.

Extrand C, *Langmuir* **2005**, 68, 2495–2532.

Extrand CW, Moon SI, *Langmuir* **2008**, 24, 9470-9473.

Extrand CW, *Langmuir* **2011**, 27, 6920–6925.

Extrand CW, *Langmuir* **2017**, 33, 9241–9242.

Extrand CW, Sung IM, *Langmuir* **2014**, 30, 8791−8797.

Fang J, Davoudi M, Chase GG, *Sep. Purif. Technol*. **2015**, 140, 77−83.

Farhan NM, Tafreshi HV, *J. Appl. Phys.* **2018**, 124, 075301.

Farhan NM, Aziz H, Tafreshi HV, *Experiments in Fluids* **2019**, 60, 87.

Funk CS, Winzer B, Peukert W, *J. Colloid & Interface Science* **2014**, 417, 171-179.

Ganne A, Lebed VO, Gavrilov AI, *Colloids Surf. A* **2016**, 499, 150-155.

Gao L, McCarthy TJ, *Langmuir*, **2006**, 22, 14, 5969–5973.

Garrod RP, Harris LG, Schofield WCE, McGettrick J, Ward LJ, Teare DOH, Badyal JPS, *Langmuir* **2007**, 23, 689−693.

Gauthier E, Hellstern T, Kevrekidis IG, Benziger J, *ACS Appl. Mater. Interfaces* **2012**, 4, 761–771.

Geraldi NR, McHale G, Xu BB, Wells GG, Dodd LE, Wood D, Newton MI, *Mater. Lett.* **2016**, 176, 205-208.

Gilet T, Terwagne D, Vandewalle N, *Appl. Phys. Lett.* **2009**, 95, 014106.

Gilet T, Terwagne D, Vandewalle N, *European Physical J. E* **2010,** 31, 3, 253.

Girifalco LA, Good, RJ, *J. Phys. Chem.* **1957**, 61, 904–909.

Good RJ, Girifalco LA, *J. Phys. Chem.* **1960**, 64, 561.

Guilizzoni M, *J. Colloid and Interface Science* **2011**, 364, 230–236.

Gurau V, Bluemle MJ, Castro ESD, Tsou YM, Man JA, Zawodzinski TA, J. Power Sources **2006**, 160, 1156–1162.

Guzowski J, Korczyk PM, Jakiela S, Garstecki P, *Soft Matter* **2012**, 8, 7269−7278.

Haefner S, Baumchen O, Jacobs K, *Soft Matter* **2015**, 11 6921-6926.

Hanumanthu R, K.J. Stebe, *Colloids Surf. A* **2006**, 282, 227–239

Hansen D, Bomholt N, Jeppesen JC, Simonsen AC, *Appl. Surf. Sci*. **2017**, 392, 181–188.

He XH, Wang W, Liu YM, Jiang MY, Wu F, Deng K, Liu Z, Ju XJ, Xie R, Chu LY, *ACS Appl. Mater. Interfaces*, **2015**, 7, 17471−17481.

Hong S-J, Chang F-M, Chou T-H, Chan SH, Sheng Y-J, Tsao H-K, *Langmuir*, **2011**, 27, 6890-6896.

Hotz CJ, Mead-Hunter R, Becker T, King AJC, Wurster S, Kasper G, Mullins BJ, *J. Fluid Mech*. **2015**, 771, 327−340.

Jamali M, Moghadama A, Tafreshi HV, Pourdeyhimi B, *Appl. Surf. Sci*. **2018,** 456, 626–636.

Jamali M, Tafreshi HV, Pourdeyhimi B, *Langmuir* **2018**, 34, 12488–12499.

Jamali M, Tafreshi HV, Pourdeyhimi B, *J. Applied Physics* **2019**, 125, 145304.

Ju J, Bai H, Zheng Y, Zhao T, Fang R, Jianga L, *Nat Commun*. **2012**, 3, 1247.

Jurin J, *Phil. Trans. R. Soc. London* **1717−1719**, 30, 739−747.

Kakaee AH, Molaeimanesh GR, Garmaroudi MHE, *J. Hydrogen Energy* **2018**, 43, 32, 15481-15491.

Kalantarian A, David R, Neumann AW, *Langmuir* **2009**, 25, 14146.

Kampa D, Wurster S, Buzengeiger J, Meyer J, Kasper G, *J. Multiph. Flow*, **2014**, 58, 313–324.

Khalil KS, Mahmoudi SR, Abu-dheir N, Varanas KK, *Applied physics letters* **2014**, 105, 041604.

Kietzig AM, Hatzikiriakos SG, Englezos P, *Langmuir* **2009**, 25, 4821–4827.

Kleingartner JA, Srinivasan S, Truong QT, Sieber M, Cohen RE, McKinley GH, *Langmuir*, **2015**, 31, pp 13201–13213

Lee C, Choi C-H, Kim C-J, *Phys. Rev. Lett.* **2008**, 101, 064501.

Lee CH, Johnson N, Drelich J, Yap YK, *Carbon* **2011**, 49, 669-676.

Li W, Amirfazli A, *Adv. Colloid Interface Sci.*, **2007**, 132, 51.

Lin PC, Yang S, *Soft Matter* **2009**, 5, 1011-1018.

Lu T., Guo Z, Li W, *RSC Adv*. **2015**, 5, 8446–8454.

Lu Z, Ng TW, Yu Y, *International Journal of Heat and Mass Transfer* **2016**, 93, 1132–113.

Malik FT, Clement RM, Gethin DT, Kiernan M, Goral T, Griffiths P, Beynon D, Parker AR, *Philos. Trans. R. Soc., A*, **2016**, 374, 20160110.

Marmur A, *Soft Matter* **2006**, 2, 12.

Marmur A, Della Volpe C, Siboni S, Amirfazli A, Drelich JW, *Surf. Innovations* **2017**, 5, 3−8.

Marmur A, Valal D, *Langmuir* **2010**, 26, 5568–5575.

McHale G, Kab NA, Newton MI, Rowan SM, *J. Colloid Interface Sci.* **1997**, 186, 453.

McHale G, Rowan SM, Newton MI, Kab NA, *J. Adhes. Sci. Technol.* **1999**, 13, 1457–1649.

McHale G, Newton MI, *Colloid and Surfaces A: Physicochemical and Engineering Aspects* **2002**, 206, 79-86.

McHale G, Newton MI, Carroll BJ, *Oil Gas. Sci. Technol.* **2001**, 56, 47–54.

McHale G, Shirtcliffe NJ, Evans CR, Newton MI, *Appl. Phys. Lett*. **2009**, 94, 064104.

Mead-Hunter R, Mullins BJ, Becker T, Braddock RD, *Langmuir* **2011**, 27, 227−232.

Mead-Hunter R, Bergen T, Becker T, O'Leary RA, Kasper G, Mullins BJ, *Langmuir*, **2012**, 28, 3483–3488.

Mei M, Fan J, Shou D, *Soft Matter* **2013**, 9, 10324−10334.

Michielsen S, Lee HJ, *Langmuir*, **2007**, 23, 6004-6010.

Michielsen S, Zhang J, Du J, Lee HJ, *Langmuir*, **2011**, 27, 11867–11872.

Moghadam A, Jamali M, Venkateshan DG, Tafreshi HV, Pourdeyhimi B, *Colloids Surf. A* **2018**, 558, 154.

Moghadam A, Yousefi SH, Tafreshi HV, Pourdeyhimi B, *Separation and Purification Technology*, **2019**, 211, 602-609.

Mullins BJ, Pfrang A, Braddock RD, Schimmel T, Kasper G, *J. Colloid Interface Sci.* **2007**, 312, 333−340.

Mullins BJ, Braddock RD, Agranovski IE, *Mathematics and Computers in Simulation* **2011**, 81, 1257-1271.

Neeson MJ, Tabor RF, Grieser F, Dagastine RR, Chan DYC, *Soft Matter* **2012**, 8, 11042.

Ojaghlou N, Tafreshi HV, Bratko D, *Soft matter* **2018,** 14, 8924-8934.

Ou J, Rothstein P, *Phys. Fluids*, **2005**, 17, 103606.

Pan Z, Weyer F, Pitt GB, Vandewalle N, Truscott TT, *Soft Matter*, **2018**, 14, 3724.

Park K-C, Chhatre SS, Srinivasan S, Cohen RE, McKinley GH, *Langmuir* **2013**, 29, 13269−13277.

Patel SU, Chase GG, *Separation and Purification Technology* **2014**, 126, 62–68.

Promraksa A, Chen L-J, *J. Colloid Interface Sci.* **2012**, 384, 172–181.

Pucci MF, Liotier P-J, Drapier S, *Appl. Sci. Manuf.* **2015**, 77, 257–265.

Quere D, *Annu. Rev. Mater. Res.* **2008**, 38, 71–99.

Que´ re´ D, *Rep Prog Phys* **2005**, 68, 2495–2532.

Que´ re´ D, *Physica A-Stat Mech & Appl* **2002**, 313, 32–46.

Rebouillat S, Letellier B, Steffenino B, *International Journal of Adhesion & Adhesives* **1999**, 19, 303-314.

Rebouillat S, Steffenino B, Salvador B, *Polymer International* **2002**, 51, 1238–1247.

Reznik SN, Salalha W, Yarin AL, Zussman E, *J. Fluid Mech.* **2007**, 574, 179–207.

Rigoni C, Ferraro D, Carlassara M, Filippi D, Varagnolo S, Pierno M, Talbot D, Abou-Hassan A, Mistura G, *Langmuir* **2018**, 34, 8917−8922.

Sahu RP, Sinha-Ray S, Yarin AL, Pourdeyhimi B, *Soft Matter* **2013**, 9, 6053−6071.

Samaha MA, Tafreshi HV, Gad-el-Hak M, *Langmuir* **2012**, 28, 9759−9766.

Savita K, Saxena RC, Kumar A, Negi MS, Bhatnagar AK, Goyal HB, Gupta AK, *Fuel Processing Techno.*, **2007**, 88, 303-307.

Schellbach SL, Monteiro SN, Drelich JW, *Mater. Lett.* **2016**, 164, 599–604.

Seo D, Lee J, Lee C, Nam Y, *Scientific reports*, **2016**, 6**,** 24276.

Sett S, Yan X, Barac G, Bolton LW, Miljkovic N, *ACS Appl. Mater. Interfaces* **2017**, 9, 36400-3640.

Shi W, Anderson MJ, Tulkoff JB, Kennedy BS, Boreyko JB, *ACS Appl. Mater. Interfaces* **2018**, 14, 11979–11986.

Shirtcliffe NJ, McHale G, Newton MI, Chabrol G, Perry CC, *Adv. Mater.* **2004**, 16, 1929−1932.

Solmaz M, Park H, Madsen CK, Cheng X, *J. Vac. Sci. Technol. B* **2008**, 26, 606–610.

Song J, Huang S, Lu Y, Bu X, Mates JE, Ghosh A, Ganguly R, Carmalt CJ, Parkin IP, Xu W, Megaridis CM, *ACS Appl. Mater. Interfaces* **2014**, 6, 19858–19865.

Sullivan DE, *J. Chem. Phys.* **1981**, 74. 2604.

Sun X, Lee HJ, Michielsen S, Wilusz E, *Applied Surface Science* **2018**, 441, 791 – 797.

Tadmor R, Bahadur P, Leh A, N'guessan HE, Jaini R, Dang L, *Phys. Rev. Lett*. **2009**, 103, 266101.

Tadmor R, Das R, Gulec S, Liu J, N'guessan HE, Shah M, Wasnik PS, Yadav SB, *Langmuir* **2017**, 33, 3594–3600.

Tavana H, Neumann AW, *Adv. Colloid Interface* **2007**, 132, 1–32.

Tian X, Chen Y, Zheng Y, Bai H, Jiang L, *Adv. Mater*. **2011**, 23, 5486.

Tie L, Guo Z, Li W, *J. Colloid Interface Sci.* **2014**, 436, 19−28.

Tie L, Guo ZG, Liu WM, *ACS Appl. Mater. Interfaces,* **2015**, 7, 10641–10649.

Tie L, Guo ZG, Liu WM, *J Colloid Interface Sci.* **2015**, 453, 142–50.

Tsai C-C, Gu Y, Kornev KG, *Colloids Surf. A* **2014**, 459, 22–30.

Venkateshan DG, Tafreshi HV, *Colloids and Surf. A* **2018**, 538, 310–319.

Viswanadam C, Chase GG, *Journal of Colloid and Interface Science* **2012**, 367, 472–477.

Wei X, Chen F, Wang H, Zhou H, Ji Z, Lin T, *J Mater Chem A* **2018**, 6, 871–877.

Wei X, Zhou H, Chen F, Wang H, Ji Z, Lin T, *Adv. Funct. Mater*. **2019**, 29, 1806302.

Wenzel RN, *Ind. Eng. Chem*. **1936**, 28, 988-94.

Weyer F, Duchesne A, Vandewalle N, *Scientific Reports* **2017**, 7, 13309.

Weyer F, Lismont M, Dreesen L, Vandewalle N, *Soft Matter,* **2015**, 11, 7086-7091

Weyer F, Said MB, Hotzer J, Berghoff M, Dreesen L, Nestler B, Vandewalle N, *Langmuir* **2015**, 31, 7799−7805.

Wolansky G, Marmur A, *Langmuir* **1998**, 14, 5292–5297.

Wolansky G, Marmur A, *Colloids Surf., A* **1999**, *156*, 381.

Wu S, Polymer interface and adhesion. *New York: Marcel Dekker*, **1982**, 264.

Wu XF, Bedarkar A, Akhatov IS, *J. Appl. Phy.* **2010,** 108, 083518.

Wurster S, Meyer J, Kolb HE, Kasper G, *Separation and Purification Technology* **2015**, 152, 70–79.

Xing Y, Wang S, Feng S, Shang W, Deng S, Wang L, Hou Y, Zheng Y, *RSC Adv.*, **2017**, 7, 29606–29610.

Xu T, Lin Y, Zhang M, Shi W, Zheng Y, *ACS Nano*, **2016**, 10, 10681−10688.

Yang C, *Filtration* **2010**, 10, 60-65.

Yarin AL, Liu W, Reneker DH, *J. Applied. Phys.* **2002**, 91, 4751-4760.

Yamamoto M, Nishikawa N, Mayama H, Nonomura Y, Yokojima S, Nakamura S, Uchida K, *Langmuir* **2015**, 31, 7355−7363.

Young T, *Philos. Trans. R. Soc. Lond.* **1805**, 95, 65.

Yousefi SH, Venkateshan DG, Tang C, Tafreshi H V, Pourdeyhimi B, *J. of Applied Physics* **2018**, 124, 235307.

Yu Y, Chen H, Liu Y, Craig VSJ, Lai Z, *Adv. Colloid Interface Sci.* **2016**, 235, 46–55.

Zheng Y, Bai H, Huang Z, Tian X, Nie FQ, Zhao Y, Jiang L, *Nature* **2010**, 463, 640−643.

Appendix A

Steps Considered to Produce a Compound Droplet on a Horizontal Fiber

The steps considered for producing a compound droplet on a horizontal fiber are as follows. With the fiber mounted horizontally on two stands (on the scale), an oil droplet with the desired volume was produced using a syringe pump.

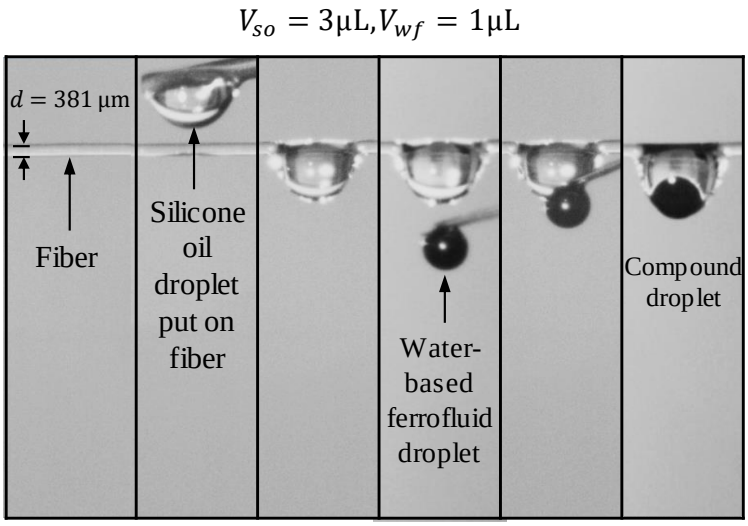

FIG. A1. The steps considered to produce a compound droplet on a horizontal fiber.

The droplet was then transferred to the fiber using the syringe. An aqueous ferrofluid droplet was then produced and brought into contact with the oil droplet that will capsulate the ferrofluid droplet because the surface tension difference toward creating a compounded droplet (see Figure A1).

Droplet Detachment vs. Droplet Breakup

Following the approach discussed in [Tadmor *et al.* 2017], we used the work of adhesion W to judge if the measured forces are for liquid–liquid break-up or for droplet–solid detachment, i.e.,

$$W = \frac{F}{L} \tag{A1}$$

where F is the maximum force measured, and L is the length of the droplet contact line on the fiber. For the latter, we use an equation developed in our previous work [Farhan and Tafrehsi, 2018],

$$L = 2\pi \sqrt{\frac{(\beta r)^2 + (l_f/2)^2}{2}} \tag{A2}$$

where β (in radian) is the azimuthal angle between the negative vertical axis and the top of the contact line on the fiber and l_f is the transverse projection of the wetted length of the fiber on its lower side as shown in the figure below. Also, see the discussion of Fig. 2.5c for more information.

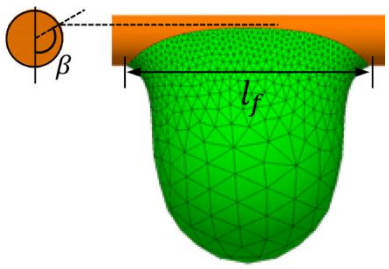

FIG. A2 shows the fiber's wetted length l_f and azimuthal angle β for a droplet hanging from the fiber at the detachment moment,

For instance, for silicone oil droplet with a volume of 3 µL detaching from a fiber with a diameter of 381 µm (Figure 4.3a in chapter 4), we obtain $W = \frac{F}{L} = \frac{49\ \mu\text{N}}{4\ \text{mm}} = 0.012\,\frac{\text{N}}{\text{m}}$ which is smaller than the surface

tension of the silicone oil used for the experiment $\sigma_{so} = 0.02\frac{\mathrm{N}}{\mathrm{m}}$. We therefore conclude that the force obtained from the experiment the force needed for droplet–solid detachment. Similarly, for the detachment of a ferrofluid-cloaked water droplet from the fiber shown in Figure 4.5 (water and ferrofluid volumes are 4 µL and of 0.3 µL, respectively, and fiber diameter is 457 µm), we obtain $W = \frac{f_{w-of}}{L} = \frac{79\ \mu\mathrm{N}}{4\ \mathrm{mm}} = 0.02\frac{\mathrm{N}}{\mathrm{m}}$ which is smaller than the surface tension of the compound droplet used in the experiment $\sigma_{w-of} = 0.06\frac{\mathrm{N}}{\mathrm{m}}$.

Appendix B: Vita

NOOR MOHSIN FARHAN

Email: farhannm@vcu.edu; noorm.farhan@yahoo.com

EDUCATION

- **PhD, Mechanical & Nuclear Engineering** (2015–2019)
  Virginia Commonwealth University
  Dissertation: Multiphase Droplet Interactions with a Single Fiber

- **MS, Mechanical Engineering** (2008–2011)
  Baghdad University, Baghdad, Iraq.
  Thesis: Effect of Wall Elasticity on the Flow Field through Stenosis Arteries and Veins

- **BS, Mechanical Engineering** (2004–2008)
  Baghdad University, Baghdad, Iraq (2004–2008)

RESEARCH INTERESTS AND ACTIVITIES

- Filtration and Separation
- Multiphase Flow
- Superhydrophobic Surfaces
- Computational Fluid Dynamics
- Interfacial Phenomena
- Thermodynamics

PEER-REVIEWED JOURNAL PUBLICATIONS

1. **N.M. Farhan** and H.V. Tafreshi, Universal Expression for Droplet–Fiber Detachment Force, *Journal of Applied Physics* 124, 075301 (**2018**).

2. H. Aziz, **N.M. Farhan**, and H.V. Tafreshi, Effects of Fiber Wettability and Size on droplet Detachment Residue, *Experiment in Fluids* 59, 122 (**2018**).

3. **N.M. Farhan**, H. Aziz and H.V. Tafreshi, Simple Method for Measuring Intrinsic Contact Angle of a Fiber with Liquids, *Experiment in Fluids* 60, 87 (**2019**).

4. **N.M. Farhan** and H.V. Tafreshi, Using Magnetic Field to Measuring Detachment Force between a Nonmagnetic Droplet and Fibers, *Langmuir* (under review).

5. **N.M. Farhan,** H. Aziz, and H.V. Tafreshi, Modeling Droplets in Cassie and Wenzel states over Granular Coatings, (in preparation)

RELEVANT COURSEWORK

- EGMN 504: Advanced Engineering Math
- EGMN 602: Convective Heat Transfer
- EGMN 603: Dynamic Systems
- EGMN 604: Materials
- EGMN 503: Continuum

WORK EXPERIENCE

- **Teaching**, Kut Technical Institute, Kut, Iraq (2012–2013)
  for the courses: Math, Thermodynamics, AutoCAD
- **Research Assistant**, Kut Technical Institute, Kut, Iraq (2012–2013)

TECHNICAL SKILLS

- **Computer Programming:** FORTRAN, MATLAB, Mathematica
- **Engineering Software:** Surface Evolver, ANSYS Fluent, AutoCAD
- **General:** Latex, Tecplot, MS Office